



Numerical Analysis of Fretting Wear and its Interaction with Fretting Fatigue

Shengjie Wang

Doctoral dissertation submitted to obtain the academic degree of
Doctor of Electromechanical Engineering

Supervisors

Prof. Magd Abdel Wahab, PhD* - Tongyan Yue, PhD**

* Department of Electromechanical, Systems and Metal Engineering
Faculty of Engineering and Architecture, Ghent University

** State Grid Xinyuan, China

June 2021



Numerical Analysis of Fretting Wear and its Interaction with Fretting Fatigue

Shengjie Wang

Doctoral dissertation submitted to obtain the academic degree of
Doctor of Electromechanical Engineering

Supervisors

Prof. Magd Abdel Wahab, PhD* - Tongyan Yue, PhD**

* Department of Electromechanical, Systems and Metal Engineering
Faculty of Engineering and Architecture, Ghent University

** State Grid Xinyuan, China

June 2021



ISBN 978-94-6355-499-2

NUR 978

Wettelijk depot: D/2021/10.500/47

Members of the Examination Board

Chair

Prof. Patrick De Baets, PhD, Ghent University

Other members entitled to vote

Samir Khatir, PhD, Ghent University

Yong Ling, PhD, Ghent University

Prof. Timon Rabczuk, PhD, Bauhaus Universität-Weimar, Germany

Xiaowei Wang, PhD, Nanjing Tech University, China

Supervisors

Prof. Magd Abdel Wahab, PhD, Ghent University

Tongyan Yue, PhD, State Grid Xinyuan, China

Acknowledgements

Firstly, I want to thank my supervisor Prof. dr. ir. Magd Abdel Wahab for the opportunity to work on this interesting research topic and for kind help and guidance in my research work.

I also want to express my gratitude to Dr. ir. Tongyan Yue, Dr. ir. Nadeem Ali Bhatti, Dr. ir. Kannaki Shanmugham Pondicherry, Dr. ir. Jacob Sukumaran, and Dr. ir. Samir Khatir for all the discussions and patience.

Moreover, I would thank all my colleagues that give me a supportive and creative working environment and my best friends Hao Xiang, Rongxue Sun, Xiaowei Wang, Shiwei Han, Lukas Steyaert, Tom and Liangliang Cheng to make my life more colourful in Ghent.

In addition, I want to thank Prof. dr. ir. Hanxiang Wang who gave me a lot of support and guidance when I worked in China University of Petroleum (East China)

Finally, I would like to thank my family for the continuous support.

English summary

Fretting is a phenomenon that happens between two contact parts when there is oscillatory relative displacement under normal load. There are two main failures in fretting process: fretting wear and fretting fatigue. Fretting wear is dominant in gross slip regime while fretting fatigue plays a key role in partial slip regime.

Fretting is detrimental for some parts of machine. For example, the connection between the blade and the dovetail of the compressor on the plane, the connection in the complex coupling, and the riveted connection between the plates of the plane shell. The main problem of fretting is that it can aggravate the condition of wear and fatigue with cycles due to the increment of the slip amplitude in the connection until final failure. In case of fretting fatigue, the main problem is crack initiation and propagation, which can lead to the final rupture of the parts.

Due to the detrimental effect on the connected parts under fretting, many researchers have investigated the mechanism and effect of both fretting wear and fretting fatigue experimentally. However, the stress and strain conditions in the parts of the connection cannot be analysed experimentally, and therefore numerical methods are alternative for the analysis of the stress strain in fretting parts. Among the numerical techniques, finite element method (FEM) shows many advantages due to its efficiency and accuracy.

There are many factors that can affect the wear characteristics of wear profiles in fretting wear, and lifetime prediction of crack initiation and propagation in fretting fatigue, such as normal load, geometry of the contact parts, roughness of contact surface, the surface treatment, etc. In the numerical model, many parameters can be considered to obtain the results that match with the experimental ones. In this thesis, FEM is applied to analyse both fretting wear and fretting fatigue. The main contribution is summarised as follows:

1. At first, a finite element (FE) model is generated to analyse the effect of the variable wear coefficient on wear characteristics for cylinder-

on-flat configuration both in gross slip regime and partial slip regime. Because in most research, the wear coefficient is considered as a constant, which does not agree with the experimental data. The result shows that in gross sliding regime, the characteristics of the wear profile has an opposite effect on the maximum tangential and shear stress for both flat specimen and cylindrical specimen. Moreover, the effect of wear volume on the plasticity accumulation is significant. The effect of variable wear coefficient model (VWCM) for flat and cylindrical specimen on the history of stress, wear characteristics and plasticity accumulation are significant. In partial slip regime, the characteristics of the wear profile has an opposite effect on the maximum shear stress and positive effect on the tangential stress for both flat and cylindrical specimen. The effect of wear volume on the plasticity accumulation is not significant. Plasticity accumulation in constant wear coefficient model (CWCM) tends to be higher than that in VCWM for both specimen and cylinder. The effect of VWCM for flat and cylindrical specimens on the history of stress, wear characteristics and plasticity accumulation are also significant.

2. Secondly, a prediction tool for fretting wear characteristics, i.e. wear width and wear depth, namely Proper Orthogonal Decomposition with Radial Basis Function (POD-RBF), is proposed. FEM method is commonly used to predict the wear characteristics. However, it is time-consuming, especially when different parameters such as slip amplitude, number of cycles and normal loads are considered. For example, for every load case, a new FE model should be solved. Through POD-RBF, wear characteristics can be predicted within one second based on the database for some cases obtained by FEM. To validate the accuracy, efficiency, and applicability of POD-RBF, its results are compared with the grey model (GM) (1, 1) and polynomial curve fitting (PCF) of second order when the load and oscillatory displacement are given. The results show that the accuracy of POD-RBF is greater than 95% and the efficiency is the highest among the three considered prediction methods. To further investigate the applicability of POD-RBF for any combination of displacement amplitude, number of cycles and normal load, five random load cases are applied. Based on the database, the accuracy of wear characteristics prediction by POD-RBF under randomly generated

load cases is higher than 95%. Compared with artificial neural network (ANN), POD-RBF shows higher computational efficiency and accuracy. This prediction tools can be used to predict fretting wear characteristics properly.

3. Finally, the interaction between the fretting wear and fretting fatigue are analysed with and without considering debris effect. Moreover, the effect of the loading cases on the wear profiles is also investigated. From the analysis, we can see that the boundary conditions influence the shear stress and wear profile when considering the wear in fretting fatigue analysis. The normal load tends to affect the wear width and wear depth, tangential load affects the wear volume, and phase difference affects the side of maximum wear volume. Wear can affect the fretting fatigue crack initiation. The predicted lifetime tends to be better than that without considering wear and all the predicted data lies in the $\pm 2N_i$. For both Ruiz parameters $F1$ and $F2$, the maximum tends to be near the boundary of the slip and stick zone. The effect of the debris on the critical plane parameters are considered and it is found that the debris can make the profile of the critical plane parameters close to that in the model without wear and move the location of crack initiation from boundary of stick and slip zone to the trailing edge. Moreover, the predicted lifetime without considering wear debris can be used as a reference for the loading case. However, the predicted crack initiation location without considering debris effect cannot be used for the fretting fatigue case

Nederlandstalige samenvatting

Fretting is een fenomeen dat optreedt tussen twee contactdelen wanneer er een oscillerende relatieve verplaatsing is onder normale belasting. Er zijn twee belangrijke manieren waarop het frettingsproces structureel kan falen: frettingslijtage en frettingvermoeiing. Frettingslijtage is dominant in een volledig slipregime, terwijl frettingvermoeiing dominant is bij een partieel slipregime.

Fretting is nadelig voor sommige machineonderdelen. Voorbeelden zijn de verbinding tussen het blad en de zwaluwstaart van de compressor, de verbinding in de complexe koppeling en de bevestigde verbinding tussen platen. Het belangrijkste probleem van fretting is dat het de toestand van slijtage en cyclusvermoeiing kan verergeren als gevolg van de toename van de slipamplitude in de verbinding tot het uiteindelijke falen. In het geval van frettingvermoeiing is het grootste probleem scheurinitiatie en propagatie, wat kan leiden tot het uiteindelijk scheuren of breken van de onderdelen.

Vanwege het nadelige effect van fretting op de verbonden delen, onderzochten onderzoekers al herhaaldelijk experimenteel het mechanisme en het effect van zowel frettingslijtage als frettingsvermoeiing. De spannings- en rekomstigheden in de onderdelen van de verbinding kunnen echter niet experimenteel worden geanalyseerd, en daarom zijn numerieke methoden een alternatief voor de analyse van de spanningsrek in frettingsonderdelen. Van de numerieke technieken vertoont de finiete-elementenmethode (FEM) veel voordelen vanwege zijn efficiëntie en nauwkeurigheid.

Er zijn veel factoren die van invloed kunnen zijn op de slijtage-eigenschappen van slijtageprofielen bij frettingslijtage en de levensduurvoorspelling van scheurinitiatie en propagatie bij frettingvermoeiing, zoals normale belasting,

geometrie van de contactonderdelen, eigenschappen van het contactoppervlak, de oppervlaktebehandeling, enz. In het numerieke model kunnen er veel parameters worden overwogen om de resultaten te verkrijgen die overeenkomen met de experimentele. In dit proefschrift wordt FEM toegepast om zowel frettingslijtage als frettingvermoeding te analyseren. De belangrijkste bijdragen zijn als volgt samengevat:

1. Ten eerste wordt er een finiete-elementenmodel (FE) gegenereerd om het effect van de variabele slijtagecoëfficiënt op de slijtage-eigenschappen voor cilinder-op-vlakconfiguratie te analyseren, zowel in het volledig-slijpregime als in het partiële-slijpregime. In de meeste onderzoeken wordt de slijtagecoëfficiënt namelijk als een constante beschouwd, wat de experimentele data tegenspreken. Het resultaat toont aan dat in het volledig-slijpregime de kenmerken van het slijtageprofiel een tegengesteld effect hebben op de maximale tangentiële en schuifspanning voor zowel platte als cilindrische exemplaren. Bovendien is het effect van het slijtagevolume op de accumulatie van plasticiteit aanzienlijk. Overigens is het effect van een model met variabele slijtagecoëfficiënt (VWCM) voor platte en cilindrische exemplaren op de geschiedenis van spanning, slijtage-eigenschappen en accumulatie van plasticiteit significant. Bij partieel slijpregime hebben de kenmerken van het slijtageprofiel een tegengesteld effect op de maximale schuifspanning en een positief effect op de tangentiële spanning voor zowel vlakke als cilindrische exemplaren. Het effect van het slijtagevolume op de accumulatie van plasticiteit is niet significant. De plasticiteitsaccumulatie in het model met constante slijtagecoëfficiënt (CWCM) is meestal hoger dan die in VCWM voor zowel het monster als de cilinder. Het effect van VWCM voor platte en cilindrische exemplaren op de geschiedenis van spanning, slijtage-eigenschappen en accumulatie van plasticiteit is ook significant.

2. Ten tweede wordt er een voorspellingstool voorgesteld voor de eigenschappen van frettingslijtage, dus slijtagebreedte en slijtagediepte, namelijk ‘gepaste orthogonale decompositie met radiale basisfunctie’ (d.i. ‘Proper Orthogonal Decomposition with Radial Basis Function’ of POD-RBF). De finiete-elementenmethode (FEM) wordt vaak gebruikt om de slijtage-eigenschappen te voorspellen. Dit is echter tijdrovend, vooral wanneer er rekening wordt gehouden met verschillende parameters zoals

slipamplitude, aantal cycli en normale belastingen. Voor elk geval van belasting moet er bijvoorbeeld een nieuw FE-model worden opgelost. Via POD-RBF kunnen slijtage-eigenschappen binnen één seconde worden voorspeld op basis van de database voor sommige gevallen die FEM heeft opgeleverd. Om de nauwkeurigheid, efficiëntie en toepasbaarheid van POD-RBF te valideren, worden de resultaten vergeleken met het grijze model ('grey model' of GM) (1, 1) en polynomiale curve-fitting (PCF) van tweede orde wanneer de belasting en oscillerende verplaatsing worden gegeven. De resultaten laten zien dat de nauwkeurigheid van POD-RBF groter is dan 95% en dat de efficiëntie van de drie beschouwde voorspellingsmethoden het hoogst is. Om de toepasbaarheid van POD-RBF verder te onderzoeken voor elke combinatie van verplaatsingsamplitude, aantal cycli en normale belasting, worden vijf willekeurige belastingsgevallen toegepast. Op basis van de database is de nauwkeurigheid van de voorspelling van slijtage-eigenschappen door POD-RBF onder willekeurig gegenereerde belastingsgevallen hoger dan 95%. Vergeleken met het artificiële neurale netwerk (ANN) vertoont POD-RBF een hogere rekenefficiëntie en nauwkeurigheid. Deze voorspellingstools kunnen worden gebruikt om de eigenschappen van frettingslijtage goed te voorspellen.

3. Ten slotte wordt de interactie tussen frettingslijtage en frettingsvermoeiing geanalyseerd met en zonder rekening te houden met het puineffect. Bovendien wordt ook het effect van de belastingsgevallen op de slijtageprofielen onderzocht. Uit de analyse kunnen we zien dat de randvoorwaarden de schuifspanning en het slijtageprofiel beïnvloeden wanneer we de slijtage beschouwen bij de analyse van de frettingsvermoeiing. De normale belasting heeft invloed op de slijtagebreedte en slijtagediepte, tangentiële belasting heeft invloed op het slijtagevolume, en faseverschil heeft invloed op de zijde van het maximale slijtagevolume. Slijtage kan het begin van de scheurinitiatie beïnvloeden. De voorspelde levensduur is meestal beter dan wanneer er geen rekening gehouden wordt met slijtage en alle voorspelde gegevens liggen in de $\pm 2N_i$. Voor zowel F1 als F2 ligt het maximum meestal in de buurt van de grens van de slip- en stickzone. Het effect van het puin op de kritieke vlakparameters wordt in overweging genomen en er wordt vastgesteld dat het puin het profiel van de kritieke vlakparameters zonder slijtage dichtbij dat in het model kan brengen en de locatie van scheurinitiatie kan verschuiven van de grens van de stick en slipzone tot de achter-rand. Bovendien kan de

voorspelde levensduur zonder rekening te houden met puin worden gebruikt als referentie voor het belastingsgeval. De voorspelde locatie van scheurinitiatie zonder rekening te houden met het effect van puin kan echter niet worden gebruikt in het geval van frettingsvermoeiing.

Contents

Contents.....	xi
List of Figures.....	xv
List of Tables.....	xxiii
List of symbols.....	xxv
List of abbreviation.....	xxix
Chapter 1 Introduction.....	1
1.1 Fretting wear and fretting fatigue.....	1
1.1.1 Fretting wear.....	1
1.1.2 Fretting fatigue.....	2
1.2 Problems of fretting wear and fretting fatigue.....	2
1.2.1 Fretting wear problem.....	2
1.2.2 Fretting fatigue problem.....	3
1.3 Finite element method (FEM).....	4
1.4 Motivation of the thesis.....	5
1.5 Outline of the thesis.....	5
1.6 Conclusion remarks.....	6
Chapter 2 Background and Literature review.....	7
2.1 Overview.....	7
2.2 Contact mechanics.....	8
2.3 Fretting.....	12
2.3.1 Fretting configuration.....	12
2.3.2 Fretting regime.....	13
2.3.3 Fretting maps.....	15
2.4 Fretting wear.....	17
2.4.1 Wear models.....	20
2.4.2 Critical role of loading conditions and material properties ..	23
2.4.3 Numerical modelling of fretting wear.....	24

2.4.4	Fretting wear test rig.....	29
2.5	Fretting fatigue	30
2.5.1	Basic theories of plain fatigue	31
2.5.2	Crack initiation in fretting fatigue	36
2.5.3	Crack propagation of fretting fatigue	43
2.5.4	Numerical modelling of fretting fatigue	48
2.5.5	Fretting fatigue test rig	53
2.6	Interaction between fretting wear and fretting fatigue.....	54
2.6.1	Effect of wear on crack initiation	54
2.6.2	Effect of wear on crack propagation.....	55
2.7	Prediction methods	56
2.7.1	POD-RBF	56
2.7.2	Grey model	57
2.7.3	Curve fitting.....	58
2.7.4	ANN	59
2.8	Concluding remarks.....	60
Chapter 3	Methodology and FE modelling	63
3.1	Overview	63
3.2	Variable wear coefficient model in fretting wear	63
3.2.1	Experimental setup	64
3.2.2	Numerical models.....	66
3.2.1	Numerical implementation	74
3.3	Predictive tools to predict the wear characteristics.....	75
3.3.1	Model description.....	75
3.3.2	Verification and validation of the FE model	77
3.3.3	Prediction by POD-RBF.....	81
3.4	Combined fretting wear and fretting fatigue models.....	84
3.4.1	Experimental set-up.....	84
3.4.2	FE model	86
3.4.3	Verification and numerical implementation	87
3.4.4	Models with different boundary conditions.....	88

3.4.5	Loading cases for wear profile analysis.....	89
3.4.6	Fretting fatigue model with debris layer.....	91
3.5	Conclusion remarks	94
Chapter 4	Wear characteristics analysis	95
4.1	Overview	95
4.2	Effect of variable wear coefficient on wear characteristics	96
4.2.1	Gross sliding regime	96
4.2.2	Partial slip regime	102
4.3	Prediction of wear characteristics by POD-RBF	108
4.3.1	Results of simulated cases	108
4.3.2	Prediction of wear profile for different number of cycles ..	110
4.3.3	Prediction of wear profile for three different parameters ...	113
4.4	Conclusion remarks	117
Chapter 5	Effect of wear on fretting fatigue.....	119
5.1	Overview	119
5.2	Effect of boundary condition on the FE results	120
5.3	Effect of loading cases and phase difference on wear profiles...	121
5.4	Effect of wear on fatigue initiation position	123
5.5	Lifetime prediction of crack initiation considering wear effect .	125
5.6	Effect of debris layer on crack initiation parameter	126
5.7	Conclusion remarks	129
Chapter 6	Conclusions and future work	131
6.1	Conclusion	131
6.2	Future work	134
References	137
List of publications	155

List of Figures

Figure 1-1– Fretting wear happens on crowned teeth and straight teeth of the spline coupling from left to right..... 2

Figure 1-2– The schematic of the hip prosthesis and its mechanism..... 3

Figure 1-3– Fretting fatigue damage: (a) crack propagation at the root of the bladed disk dovetail, and (b) SEM of the fracture surface for thin steel wire 4

Figure 2-1– Cylinder-on-flat configuration for analytical solutions 8

Figure 2-2– Normalized contact pressure along the normalized contact width 9

Figure 2-3– Normalized shear stress as a function of the normalized contact width with tangential load, Q 11

Figure 2-4– Normalized shear stress as a function of the normalized contact width with tangential load, Q and axial load, σA 11

Figure 2-5– Contact configurations: (a) point contact, (b) line contact, and (c) surface contact 12

Figure 2-6– Fretting loading conditions for ball-on-flat configuration 13

Figure 2-7– Fretting regimes: (a) stick regime, (b) partial slip regime, and (c) gross slip regime 14

Figure 2-8– Schematic of the stick zone and slip zone in partial slip and gross slip regime for both cylinder-on-flat and ball-on-flat configuration 14

Figure 2-9– Fretting map from Vingsbo..... 15

Figure 2-10– Fretting maps: (a) running condition fretting map, and (b) material response fretting map 16

Figure 2-11– Quantitative analysis for fretting map..... 17

Figure 2-12– Schematic of fretting wear kinematics.....	18
Figure 2-13– Optical graphs of fretting wear phenomenon observed in: (a) blade-disc connection, (b) connection between steel wires	19
Figure 2-14– Definition of the wear volume wear coefficient, K and threshold of dissipated energy to activate the wear, Ed_{th}	21
Figure 2-15– Schematic of three stages for fretting wear.....	22
Figure 2-16– Schematic of the fretting wear model with roughness: (a) macro model, (b) micro model, and (c) local roughness	25
Figure 2-17– Schematic of the fretting wear model with the debris layer ...	27
Figure 2-18– Debris layer updating model.....	27
Figure 2-19– Schematic diagram of the debris layer in FDEM.....	28
Figure 2-20– Schematic of the test rig for fretting wear	29
Figure 2-21– Loading history and terms for plain fatigue.....	31
Figure 2-22– S-N curve for plain fatigue	32
Figure 2-23– Schematic of the intrusion and extrusion in sub-grain scale and crack propagation in grain scale under tensile loading.....	33
Figure 2-24– Crack growth behaviour.....	34
Figure 2-25– Schematic of compact tension specimen and cross-section of its crack	35
Figure 2-26– Loading modes of crack opening.....	36
Figure 2-27– Sketch of the angle of the critical plane on one point.....	37
Figure 2-28– Schematic of the representative element.....	41
Figure 2-29– Schematic of crack and the point near the crack tip	44
Figure 2-30– SIFs near the tip of the new crack.....	45
Figure 2-31– Path integral of J	46
Figure 2-32– FE model of cylindrical pad on flat specimen	49
Figure 2-33– In phase loading conditions of fretting fatigue	50
Figure 2-34– Bending fretting fatigue of bolt connection: (a) sketch of the bolt connection and loading condition, (b) FE mesh for the configuration	50

Figure 2-35– Schematic of the enrichment of the nodes in XFEM: circle is the Heaviside enrichment, and square is the crack tip enrichment..... 52

Figure 2-36– Mesh of crack generated by seam in ABAQUS 53

Figure 2-37– Fretting fatigue test rig: (a) apparatus for the experiments, and (b) schematic of the test rig 53

Figure 3-1– Experimental variation of wear volume with number of cycles vs wear volume in simulation 64

Figure 3-2– Geometry of the cylindrical pad and flat specimen 65

Figure 3-3– Relationship between plastic strain and stress 65

Figure 3-4– FE model: (a) FE model for the flat specimen and cylindrical specimen, and (b) partition for the contact zone..... 66

Figure 3-5– Loading history of FE model 67

Figure 3-6– Contact pressure comparison between the FE model and analytical solution, when $P = 1000 \text{ N}$ 67

Figure 3-7– ABAQUS implementation for FE analysis of fretting wear 68

Figure 3-8– The schematic of the vertical movement for ALE nodes..... 68

Figure 3-9– Wear coefficient changes with the number of cycles for both flat specimen and cylindrical pad 69

Figure 3-10– Flowchart to obtain the wear coefficient to be used in FE model 70

Figure 3-11– Experimental wear coefficient after certain cycles’ interval: (a) Flat specimen, and (b) cylindrical pad..... 71

Figure 3-12– Wear characteristics of both flat specimen and cylindrical specimen after 25000 cycles..... 72

Figure 3-13– Profiles of the cylinder before and after fretting wear and the adjusted wear profile after 25000 cycles 72

Figure 3-14– Schematic of CWCM and VWCM in the first 25000 cycles for both specimens: (a) cylindrical pad; (b) flat specimen..... 73

Figure 3-15– Flow chart of numerical implementation of fretting wear for cylindrical pad and flat specimen 74

Figure 3-16– Dimensions and boundary conditions of fretting wear FE model 75

Figure 3-17– Loading history - N is the total number of cycles..... 76

Figure 3-18– Comparison of the FE results with the analytical solution - contact pressure when P is 185 N..... 77

Figure 3-19– Mindlin-Cattaneo shear distribution comparison between analytical and FE results ($Q = 1000$ N and $P = 1670$ N)..... 78

Figure 3-20– Shear stress for different mesh size and the maximum stress trend versus mesh size- $P = 1670$ N, $Q = 1000$ N 79

Figure 3-21– Comparison of the FE model wear profile with referenced experimental results after 18000 cycles: (a) P is 185 N and D is 25 μm , (b) P is 1670 N and D is 25 μm [40] 80

Figure 3-22– Wear profiles after 30000 cycles- P is 1670 N and D is 25 μm 81

Figure 3-23– Flowchart of POD RBF applied to the wear characteristics prediction..... 83

Figure 3-24– Schematic of the experimental set-up 85

Figure 3-25– FE model 1 for the fretting fatigue experiment 86

Figure 3-26– Loading history for the fretting fatigue experiment..... 87

Figure 3-27– Verification of the FE model by the analytical solution 88

Figure 3-28– FE model 2 for the fretting fatigue experiment 88

Figure 3-29– Flowchart for the implementation of the prediction of crack initiation lifetime 90

Figure 3-30– Experimental wear profile near the trailing edge..... 91

Figure 3-31– Wear profiles: (a) wear profile after 100000 cycle for Exp. 1, and (b) the schematic of the debris layer in fretting fatigue model 92

Figure 3-32– Schematic of the contact in FE model 93

Figure 3-33– Schematic of the introduction time point of the debris to model 93

Figure 4-1– History and profile of wear characteristics for the flat specimen in the gross sliding regime for both CWCM and VWCM when $\delta = 50$ mm:

(a), (b), and (c) are the history of wear characteristics, and (d) is the wear profiles after 10000th and 25000th cycle..... 96

Figure 4-2– Profile and history of equivalent plastic strain for the flat specimen in the gross sliding regime for both CWCM and VWCM when $\delta = 50$ mm: (a) the profiles at 10000th cycle and 250000th cycle, and (b) the maximum value history 98

Figure 4-3– Profile and history of shear and tangential stresses for the flat specimen in the gross sliding regime for both CWCM and VWCM: (a) and (b) are shear and tangential stress profiles in 10000th cycle and 250000th cycle when $\delta = 50$ mm, and (c) and (d) are the history of maximum shear and tangential stress, respectively 98

Figure 4-4– History and profile of wear characteristics for the cylindrical pad in the gross sliding regime for both CWCM and VWCM when $\delta = 50$ mm: (a), (b) and (c) are the history of wear characteristics, and (d) is the wear profiles after 10000th and 25000th cycle..... 100

Figure 4-5– Profile and history of the equivalent plastic strain for the cylindrical pad in the gross sliding regime for both CWCM and VWCM when $\delta = 50$ mm: (a) is the profiles in 10000th cycle and 250000th cycle, and (b) is the maximum value history 101

Figure 4-6– Profile and history of shear and tangential stress for the cylindrical pad in the gross sliding regime for both CWCM and VWCM: (a) and (b) are shear and tangential stress profiles in 10000th cycle and 250000th cycle when $\delta = 50$ mm, and (c) and (d) are the history of maximum shear and tangential stress, respectively 101

Figure 4-7– History and profile of wear characteristics for the flat specimen in the partial slip regime for both CWCM and VWCM when $\delta = 10$ mm: (a), (b), and (c) are the history of wear characteristics, and (d) is the wear profiles after 10000th and 25000th cycle..... 102

Figure 4-8– Profile and history of equivalent plastic strain for the flat specimen in the partial slip regime for both CWCM and VWCM when $\delta = 10$ mm: (a) is the profiles in 10000th cycle and 250000th cycle, and (b) is the maximum value history 103

Figure 4-9– Profile and history of shear and tangential stress for the flat specimen in the partial slip regime for both CWCM and VWCM: (a) and (b)

are shear and tangential stress profiles in 10000th cycle and 250000th cycle when $\delta = 10$ mm, and (c) and (d) are the history of maximum shear and tangential stress, respectively 104

Figure 4-10– History and profile of wear characteristics for the cylindrical pad in the partial slip regime for both CWCM and VWCM when $\delta = 10$ mm: (a), (b), and (c) are the history of wear characteristics, and (d) is the wear profiles after 10000th and 25000th cycle..... 105

Figure 4-11– Profile and history of the equivalent plastic strain for the cylindrical pad in partial slip regime for both CWCM and VWCM when $\delta = 10$ mm: (a) is the profiles in 10000th cycle and 250000th cycle, and (b) is the maximum value history 106

Figure 4-12– Profile and history of shear and tangential stress for cylindrical pad in the partial slip regime for both CWCM and VWCM: (a) and (b) are shear and tangential stress profiles in 10000th cycle and 250000th cycle when $\delta = 10$ mm, and (c) and (d) are the history of maximum shear and tangential stress, respectively 107

Figure 4-13– Wear depth (μm) versus number of cycles under different amplitudes - normal load 185 N 109

Figure 4-14– Wear width (μm) versus number of cycles under different amplitudes - normal load 185 N 109

Figure 4-15– Comparison of wear characteristics between simulated data and predicted values by POD-RBF for normal load 185 N and displacement amplitude 20 μm 110

Figure 4-16– Corresponding prediction error of POD-RBF of the data in Figure 4-15 111

Figure 4-17– Wear characteristics prediction by GM (1, 1)..... 111

Figure 4-18– Wear characteristics prediction by PCF..... 112

Figure 4-19– Corresponding prediction error of PCF of the data in Figure 4-18 112

Figure 4-20– Comparison of wear characteristics obtained by FEM and POD-RBF under random generated load cases 114

Figure 4-21– Prediction error by POD-RBF compared with the FEM raw data under random generated load cases 115

Figure 4-22– Comparison of wear characteristics obtained by FEM and ANN under random generated load cases 115

Figure 4-23– Prediction error by ANN compared with the FEM raw data under random generated load cases 116

Figure 5-1– Effect of boundary conditions on the wear profile and shear stress: (a) wear profiles after 80000 cycles and releasing step, and (b) shear stress at the end of 80000th cycle..... 120

Figure 5-2– Effect of loading cases on wear profiles: (a) effect of normal load, (b) effect of tangential load, and (c) effect of axial load 122

Figure 5-3– Variation of Ruiz parameters with cycles for Exp. 1 when σ_A reaches the maximum value 123

Figure 5-4– Variation of critical plane parameters with cycles for Exp. 1. 123

Figure 5-5– Variation of damage accumulation value with cycles for Exp. 1 124

Figure 5-6– Crack initiation lifetime predicted by FP, FS and SWT for Exp. 1 125

Figure 5-7– Critical plane parameters considering the debris effect after 10000 cycles 126

Figure 5-8– Shape of the damage accumulation value for three critical plane parameters that reaches 1, when Δh is 0.15 μm 127

Figure 5-9– Crack initiation lifetime predicted by *FP*, *FS* and *SWT* for Exp. 1 considering debris when Δh is 0.15 μm 128

List of Tables

Table 3-1– Material properties	65
Table 3-2– Normal load cases and the corresponding CoF and wear coefficient	76
Table 3-3– Contact width and maximum contact pressure for all the normal loads.....	77
Table 3-4– Experimental data for fretting fatigue test [2].....	85
Table 3-5– Constant of material properties [164, 165].....	85
Table 3-6– The loading cases to analyse the effect of loading condition on wear characteristics	89
Table 4-1– Wear depth (μm) at different cycles under different amplitudes - normal load 185 N.....	108
Table 4-2– Wear width (μm) at different cycles under different amplitudes - normal load 185 N.....	109
Table 4-3– CPU time of methods for parameters prediction.....	113
Table 4-4– CPU time of methods for 3 parameter prediction	116

List of symbols

V	Wear volume
s	Sliding distance
k	Specific wear rate
F	The load
$\Delta h(x)$	Wear depth at position x
K_A	Archard's wear coefficient
δ	Applied stroke half amplitude
q_i	Shear stress at the node i
ΔN	Jump cycles
W_V	Wear volume
K	Energy wear volume coefficient
E_d	Accumulated dissipated energy
q_i	Shear force in the i th cycle
ds_i	Sliding distance in the i th cycle
R'	Equivalent radius
E'	Effective Young's modulus

ν	Poisson ratio
a	Contact width
L	Contact length
μ	Coefficient of friction
τ	Shear stress
c	Stick zone width
Q	Tangential frictional force
e	Offset of the stick zone
p_{max}	Maximum contact pressure
σ_A	Axial load
R_E	Equivalent radius
δ_{global}	Global slip amplitude
S_a	Stress amplitude
S_r	Stress range
S_m	Mean stress
σ_{max}	Maximum stress
σ_{min}	Minimum stress
τ_θ	Shear stress on the plane
ΔK	Stress intensity range
$\Delta\tau_{max}$	Maximum range of shear stress
σ_n^{max}	Maximum normal stress
σ_{f-1}	Fatigue limit in tension

τ_{f-1}	Fatigue limit in torsion
τ'_f	Coefficient of shear fatigue strength
b'	Exponent of torsion fatigue strength
$\Delta\gamma_{max}$	Maximum shear strain range
σ_y	Yield stress
G	Shear modulus
γ'_f	Shear fatigue ductility coefficient
c'	Fatigue ductility exponent in tension
σ_n^{max}	Maximum normal stress
R_v	Triaxiality function
σ_H	Hydrostatic stress
K_I	Stress intensity factor in model I

List of abbreviation

FEM	Finite element method
FDEM	Combined finite and discrete element method
FE	Finite element
MD	Molecular dynamics
MPC	Multi point constraint
ALE	Arbitrary Lagrangian-Eulerian
<i>FP</i>	Findley parameter
<i>FS</i>	Fatemi-Socie parameter
<i>SWT</i>	Smith-Watson-Topper
<i>F1</i>	Ruiz <i>F1</i> parameter
<i>F2</i>	Ruiz <i>F2</i> parameter
CWCM	Constant wear coefficient model
VWCM	Variable wear coefficient model
GM	Grey model
POD-RBF	Proper Orthogonal Decomposition with Radial Basis Function

PCF

Polynomial curve fitting

ANN

Artificial neural network

XFEM

Extended finite element method

Chapter 1 Introduction

1.1 Fretting wear and fretting fatigue

Fretting happens when there is small oscillatory relative slip between two contact parts [1]. Fretting can cause damaged to the mechanical parts, which may be detrimental to the proper operating of the machines and vehicles. The main damaged can be classified into fretting wear, fretting fatigue and fretting corrosion [2]. Oxidation is one of the fretting corrosions, which always couple with wear. Wear and fatigue in fretting process are the main threats to the contacting parts and are mainly researched and investigated. They are described as follows.

1.1.1 Fretting wear

Wear happens on the two contact surfaces when there is relative slip. There are two wear mechanisms: abrasive wear and non-abrasive wear [3]. Ploughing and adhesion can happen in fretting process based on the loading

condition, which causes material removal, and debris is generated between two contact parts. Therefore, in fretting process, the wear mode transformed from two-body wear to three-body wear.

1.1.2 Fretting fatigue

In engineering mechanical design, the avoidance of the material yield and fracture is the basic objective [4]. Fatigue of material can cause surface crack nucleation and propagation, which can lead to the final fracture. Therefore, there are two stages for common fatigue: crack initiation and crack propagation [5]. For fretting wear, there are two contact parts. In crack initiation stage, the sub-grain scale extrusion and intrusion happen on the contact surface, where there is a stress concentration. Then grain scale short crack and long crack happen in succession. Compared with the fretting wear set up, the axial load is applied to cause a tension stress in fretting process.

1.2 Problems of fretting wear and fretting fatigue

1.2.1 Fretting wear problem

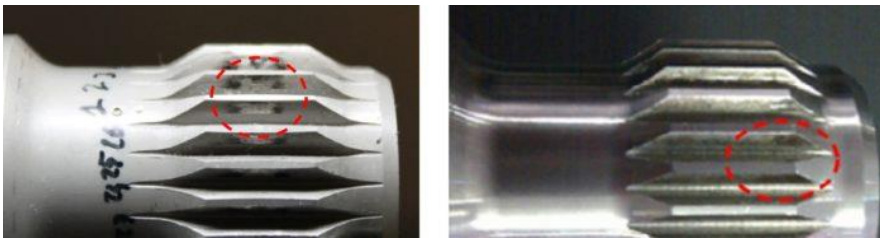


Figure 1-1– Fretting wear happens on crowned teeth and straight teeth of the spline coupling from left to right

Spline couplings are commonly used for the transmission of torques between two shafts. The internal teeth and external teeth are jointed together. Due to vibration, deflection of the teeth or the misalignment of the shafts' axes, small relative slip between internal and external teen happens. Therefore, fretting

wear happens on the surface of the teeth and can be a main damage [6]. The fretting wear phenomenon on the straight teeth and crown teeth surface is shown in Figure 1-1 [7]. Wear on the teeth surface can degrade its strength, which can lead to a rupture of the teeth, then the wear aggravates.

Total hip replacement is commonly used for the patients. In 2014, there are about 89 000 hip operations in UK and there are 285 000 hip operations each years in America [8]. Therefore, the mechanism for the hip prosthesis should be carefully analysed to make lifetime longer. The schematic of the hip prosthesis and its mechanism are shown in Figure 1-2. From Figure 1-2(b), we can see that the connection between the head and stem is conical taper fixation. Under impact load, there is a tangential relative slip and rotation between head and stem, which can cause wear and affect the lifetime of the hip prosthesis by fretting [9].

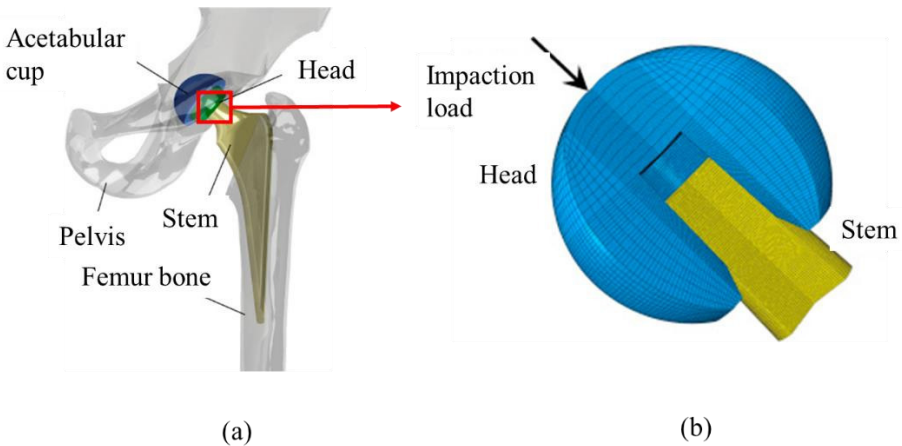


Figure 1-2– The schematic of the hip prosthesis and its mechanism

1.2.2 Fretting fatigue problem

As shown in Figure 1-3 (a), due to the fretting between the disk and blade, crack initiates at the bottom of the dovetail and tends to propagate to the circumferential surface, which is detrimental to the turbine engine [10]. As

shown in Figure 1-3 (b), the initiation point is in the wear-zone. Therefore, the geometry change due to the wear in fretting process can influence stress condition and then affect the crack initiation location and fatigue lifetime, which is considered and analysed in this thesis [11].

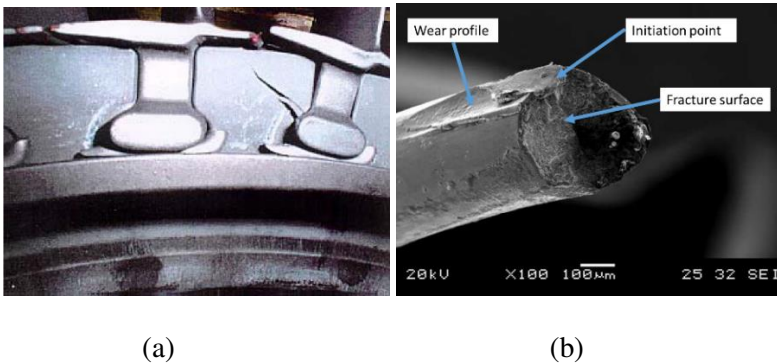


Figure 1-3– Fretting fatigue damage: (a) crack propagation at the root of the bladed disk dovetail, and (b) SEM of the fracture surface for thin steel wire

1.3 Finite element method (FEM)

Nowadays numerical models are widely used to solve the engineering problems. FEM shows its advantage due to its efficiency and accuracy and becomes popular. The development of FEM is closely related to the development of computers, which make the calculation method rapid. It was first applied in the field of continuum mechanics to analyse static and dynamic characteristics of aircraft structures. Then, it is widely used to solve the problems of heat conduction, electromagnetic field, fluid mechanics etc. ABAQUS is one of the commonly used commercial FEM software and is used to solve fretting problems presented in this thesis. In fretting process, there are many factors that affect the lifetime of the parts. However, the experiments cannot provide measurements of the stresses and strains in fretting process. Analytical method can only be used to obtain the stresses and strains in the position of the maximum and minimum tangential load on the contact surface.

Numerical model by FEM can be used to get the stresses and strains at any time point during fretting process, which can be used to predict the lifetime and the extent of damage in the parts.

1.4 Motivation of the thesis

In fretting process, many factors can affect the wear characteristics in fretting wear and lifetime prediction in fretting fatigue. Many researchers have investigated the effect of normal load, tangential load, surface treatment, the defect of the material etc., on the wear characteristics and fatigue lifetime. In this thesis, the effect of variable wear coefficient on wear characteristics is analysed, which are considered as a constant in most published research works. Then, to increase the efficiency of the prediction of the wear characteristics, Proper Orthogonal Decomposition with Radial Basis Function (POD-RBF) is applied for different normal loads, tangential displacements, and cycles. Furthermore, in fretting fatigue, the effect of wear is commonly ignored. In this thesis, the effect of wear on fretting fatigue is investigated.

1.5 Outline of the thesis

The remaining chapters of the thesis are summarised as follows.

Chapter 2: After the introduction of contact mechanics, which can be used as an analytical solution to validate the FE models, fretting, fretting wear, fretting fatigue are described in detail including the wear models and theories of crack initiation and propagation. Then, the literature review on the interaction between fretting wear and fretting fatigue is presented. Finally, the prediction tools, which are used in this thesis are described.

Chapter 3: The methodology and FE modelling for the variable wear coefficient model (VWCM), prediction tools and interaction between fretting wear and fretting fatigue are presented in detail.

Chapter 4: The effect of the variable wear coefficient on wear characteristics and details of the prediction tools are presented.

Chapter 5: The effect of the wear on fretting fatigue with and without considering the effect of the debris is given.

Chapter 6: The conclusions and future work are presented.

1.6 Conclusion remarks

In this chapter, the introduction of this thesis is given. Due to the complexity in the problems of fretting wear and fretting fatigue in engineering applications, numerical models should be used to investigate the effect of different parameters and analyse the failure mechanism based on the stress and strain data. Moreover, the outline of the thesis is presented.

Chapter 2 Background and Literature review

2.1 Overview

Fretting is a complex phenomenon, and fretting wear and fretting fatigue are the two main damage mechanisms in fretting process. Numerical modelling is commonly used for the analysis of fretting wear and fretting fatigue. In this chapter, theoretical background and literature review for the research topics presented in the thesis are introduced in detail. Firstly, the contact mechanics that can be used for the verification of the FE contact model is presented in section 2.2. Then the concept, basic theory, and literature review on fretting, fretting wear, and fretting fatigue are described in section 2.3, 2.4, and 2.5, respectively. The literature review on interaction between fretting wear and fretting fatigue are given in section 2.6, while the prediction tools which are used in this thesis are given in section 2.7. Finally, the conclusion remarks are given in section 2.8.

2.2 Contact mechanics

Contact between two parts is essential to the phenomenon of fretting. Contact mechanics theory is an effective way for the verification of FE contact model. The shear stress obtained by analytical solution can also be used to check the convergence of the FE model. Moreover, the shear stress on the contact surface causes fretting wear. Besides, crack also initiates from the contact surface in fretting fatigue. Therefore, in this section, the analytical solution of contact pressure, and shear stress for the cylinder-on-flat configuration under normal load, tangential load and axial load is described.

Hertzian contact theory is used to calculate the contact pressure distribution for the two elastic contact parts under normal load, which was originally proposed by Hertz [12]. Two elastic bodies with curved surfaces under normal load were analysed in Refs. [13] and [14]. Hertzian contact is derived based on the following assumptions: (1) no plastic deformation, (2) the dimensions have no limitation on the stress distribution, and (3) there is no friction between the contact surfaces. A cylinder-on-flat configuration is shown in Figure 2-1. where F is the normal load, Q is the tangential stress, σ_A is the axial stress and R_1 is the radius of the cylinder.

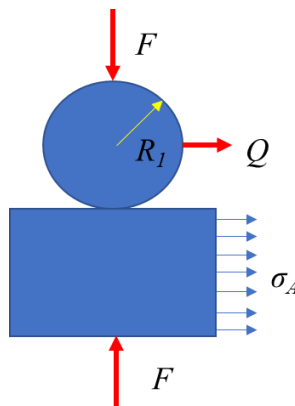


Figure 2-1– Cylinder-on-flat configuration for analytical solutions

This contact configuration is called line contact, in which the half-contact width a can be written as:

$$a = 2 \left(\frac{2}{\pi} \right)^{\frac{1}{2}} \left(\frac{F}{L} \right)^{\frac{1}{2}} \left(\frac{R'}{E'} \right)^{\frac{1}{2}} \quad (2.1)$$

Where F is the normal load, L is the length of the cylinder and flat, R' is the equivalent radius and E' is the effective Young's modulus. The equivalent radius and the effective Young's modulus are given by:

$$\frac{1}{R'} = \frac{1}{R_1} + \frac{1}{R_2} \quad (2.2)$$

$$\frac{1}{E'} = \frac{1 - \nu_1^2}{2E_1} + \frac{1 - \nu_2^2}{2E_2} \quad (2.3)$$

Where R_1 and R_2 are the radii, E_1 and E_2 are Young's moduli and ν_1 and ν_2 are the Poisson ratios of the cylinder and flat, respectively. For flat specimen, the radius of the curvature tends to be positively infinity. Therefore, $\frac{1}{R_2}$ tends to be zero in cylinder-on-flat configuration [14]. Herein, the equation for contact pressure along the horizontal direction is given by:

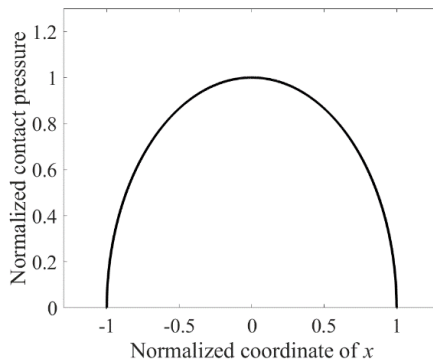


Figure 2-2– Normalized contact pressure along the normalized contact width

$$p(x) = p_{max} \sqrt{1 - \left(\frac{x}{a}\right)^2}, \text{ where } p_{max} = \left(\frac{FE'}{2\pi LR'}\right)^{\frac{1}{2}} \quad (2.4)$$

The distribution of contact pressure is shown in Figure 2-2.

Two cases can take place when the tangential load as shown in Figure 2-1 is applied. The relative slip occurs for the whole contact surface (gross sliding), and slip occurs for partial slip regime (partial slip). We take the partial slip regime as an example. For partial slip regime, two zones co-exist: stick zone and slip zone. For stick zone, $\tau < \mu p$, where p is the normal pressure derived from Eq. (2.4), μ is the coefficient of friction and τ is the shear stress due to the applied tangential load. Defining c as the half stick zone width, the shear stress in the slip zone and stick zone is given by [14]:

$$\tau(x) = \mu p_{max} \left(1 - \left(\frac{x}{a}\right)^2\right)^{\frac{1}{2}} \quad c \leq |x| \leq a \quad (2.5)$$

$$q(x) = \mu p_{max} \left(\sqrt{1 - \left(\frac{x}{a}\right)^2} - \frac{c}{a} \sqrt{1 - \left(\frac{x}{c}\right)^2} \right) \quad |x| \leq c \quad (2.6)$$

Where c is the stick zone. Which can be given by:

$$c = a \left(1 - \frac{Q}{\mu F}\right)^{\frac{1}{2}} \quad (2.7)$$

The normalized shear stress with tangential, Q load is shown in Figure 2-3. A symmetric shear stress profile can be obtained when the tangential load is applied. As shown in Figure 2-1, there is axial load, σ_A , that can affect the shape of the shear stress along the contact surface. After applying the axial load, an offset of the stick zone, e , occurs, which is given by Eq. (2.8) [15].

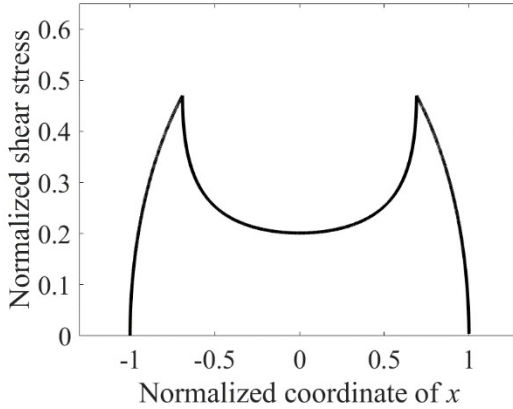


Figure 2-3– Normalized shear stress as a function of the normalized contact width with tangential load, Q

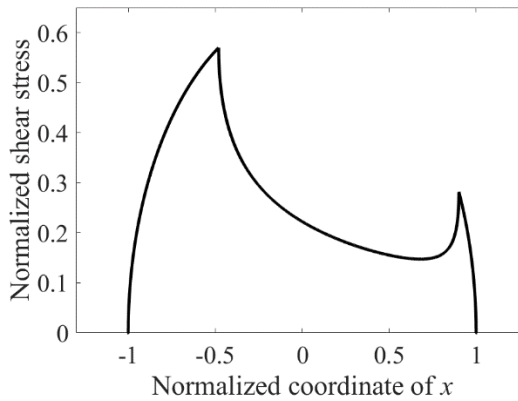


Figure 2-4– Normalized shear stress as a function of the normalized contact width with tangential load, Q and axial load, σ_A

$$e = \frac{\sigma_A a}{4\mu p_{max}} \quad (2.8)$$

The corresponding shear stress along the contact surface after applying axial load is presented in Figure 2-4, which can be derived from Eq. (2.9). The axial

load causes an unsymmetrical shear traction profile and an offset of the stick zone, e . When $e + c > a$, a reverse slip happens. Then the value of $e + c$ should be lower or equal to a to limit the axial load.

$$\begin{cases} q(x) = \mu p_{max} \sqrt{1 - \left(\frac{x}{a}\right)^2} & |x - e| > c \\ q(x) = \mu p_{max} \left(\sqrt{1 - \left(\frac{x}{a}\right)^2} - \frac{c}{a} \sqrt{1 - \left(\frac{x-e}{c}\right)^2} \right) & |x - e| < c \end{cases} \quad (2.9)$$

2.3 Fretting

Fretting is a phenomenon, in which oscillatory motion with small amplitude happens between two contact surfaces [16]. Eden et al. first introduced the fretting phenomenon in 1911 in Ref. [17], where the effect of alternating was considered for soft ductile material. With more and more research on fretting, the testing rigs, mechanisms, loading conditions etc., have been rapidly developed.

2.3.1 Fretting configuration

There are three main fretting contact configurations: point contact, line contact and surface contact as is shown in Figure 2-5. And the corresponding test configurations are ball-on-flat, cylinder-on-flat, and flat-on-flat.

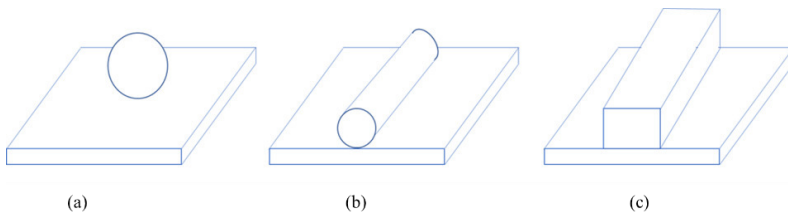


Figure 2-5– Contact configurations: (a) point contact, (b) line contact, and (c) surface contact

For line contact and surface contact, the tangential loading is mostly analysed, while for point contact, there are four kinds of loading conditions, which is given in Figure 2-6 [18, 19]. Figure 2-6 (a) shows the tangential fretting, in which tangential movement of the ball occurs under normal load, while (b) is the radial fretting with cyclic normal load. The ball rolls on the plate for rotational fretting as shown in Figure 2-6 (c), while the ball rotates along the direction of the normal load.

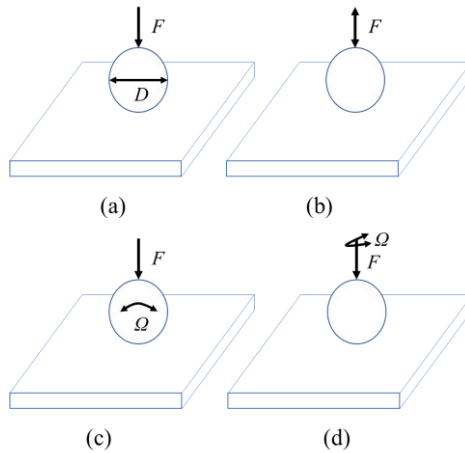


Figure 2-6– Fretting loading conditions for ball-on-flat configuration

2.3.2 Fretting regime

According to the tangential force and displacement, fretting regimes can be classified into stick regime, mixed stick and slip regime and gross slip regime. These three regimes are shown in Figure 2-7 [20], in which D_s is the slip distance and Da is the applied distance. In the stick regime, the displacement is accommodated by the elastic deformation of the contact surface and there is almost no relative slip between the two contact surfaces. In the mixed stick and slip regime, the slip is caused by elastic and plastic deformation, and the stick zone and slip zone coexist. The quasi-elliptical area is the dissipated energy caused by friction. In gross slip regime, there is a constant tangential

force. The quasi-square area is the dissipated energy generated by gross sliding.

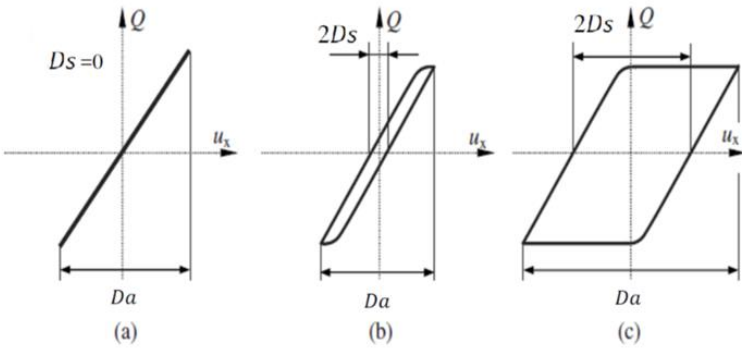


Figure 2-7– Fretting regimes: (a) stick regime, (b) partial slip regime, and (c) gross slip regime

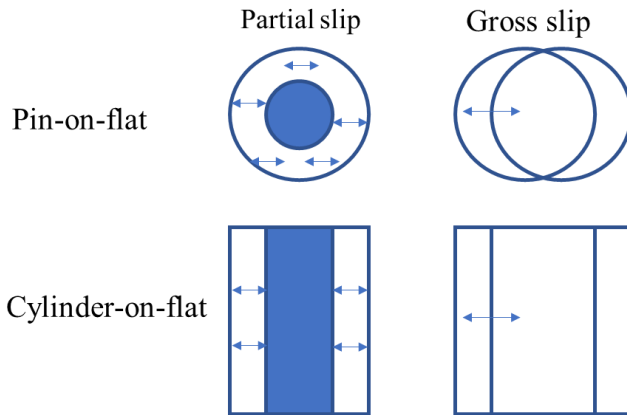


Figure 2-8– Schematic of the stick zone and slip zone in partial slip and gross slip regime for both cylinder-on-flat and ball-on-flat configuration

To make the meaning of the partial slip regime and gross slip regime more intuitive, the schematic of stick and slip zone of the cylinder-on-flat and ball-on-flat in these two regimes is shown in Figure 2-8; in which the blue surface is the stick zone.

2.3.3 Fretting maps

There are many kinds of damages in the fretting process, among which the main three damages are fretting wear, fretting fatigue and fretting corrosion [21]. Fretting corrosion can accelerate wear and pitting of the contact surface due to the chemic-mechanical effect under fretting condition [22]. Cracks can be found in the fretting process, which is mainly caused by the fretting fatigue in the partial slip regime, when the fatigue load, σ_A is applied [4, 23]. Fretting wear is a complex phenomenon, because there are many factors that have influences on the process, such as materials, stress field, environment, temperature, frequency, etc. In the fretting wear process, the material is removed from the contact surfaces, which transform the wear mode from two-body to three-body abrasive wear [21].

Fretting maps are commonly analysed to investigate the relationship between fretting wear and fretting fatigue with different normal loads and oscillatory displacements [24].

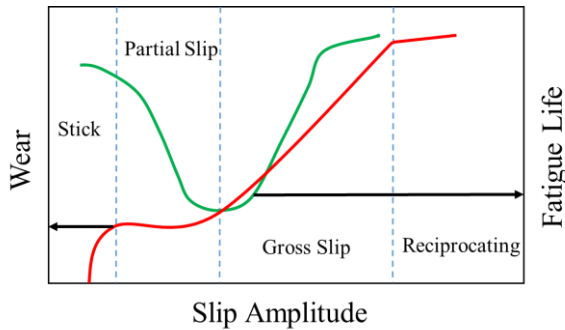


Figure 2-9– Fretting map from Vingsbo

Vingsbo proposed a fretting map after fretting experiments of carbon steel, in which the fatigue and wear in fretting process were compared for different slip amplitudes [1]. From Figure 2-9, we can see that in the stick zone, fatigue is dominant and there is less particle detachment. In partial slip regime, fatigue and wear coexist and cannot be ignored. In gross slip and reciprocating

regime, the wear is dominant, and the initial crack can be removed by wear, which can alleviate the fretting fatigue crack nucleation. Therefore, the fatigue life increased dramatically with the increase of the slip amplitude.

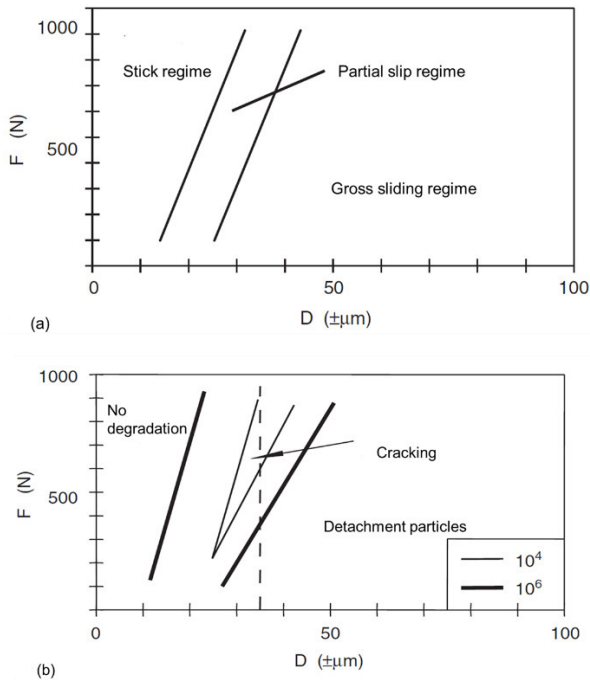


Figure 2-10– Fretting maps: (a) running condition fretting map, and (b) material response fretting map

Another two fretting maps were proposed by Zhou and Vincent as shown in Figure 2-10, in which F is the normal load and D is the oscillatory displacement [25-27]. From Figure 2-10 (a), it can be concluded that the transition normal load from partial slip regime to gross slip regime increases with the increase of the applied displacement. The running condition in Figure 2-10 (a) does not totally agree with the material response in Figure 2-10 (b). moreover, the lifetime is much lower around partial slip regime than that in gross slip and stick regimes.

The above-mentioned fretting maps was estimated based on the experimental data and there is no specific indicator to classify the corresponding regimes. As shown in Figure 2-11, Heredia and Fouvry proposed a quantitative method to distinguish the stick regime, partial slip regime and gross sliding regime by the ratio between tangential load and normal load, Q/P , the percentage of gross sliding cycle in the total number of cycles, %GS and accumulated dissipated energy $\sum E_d$. It means that, in partial slip regime, both gross slip and partial slip exist. Other parameter, A is introduced to define the transition from partial slip cycles to gross slip cycles [28]. A is the ratio between dissipated energy and the total energy in one cycle. Moreover, the phenomenon of wear and crack near the transition zone are also used to make the material response clearer.

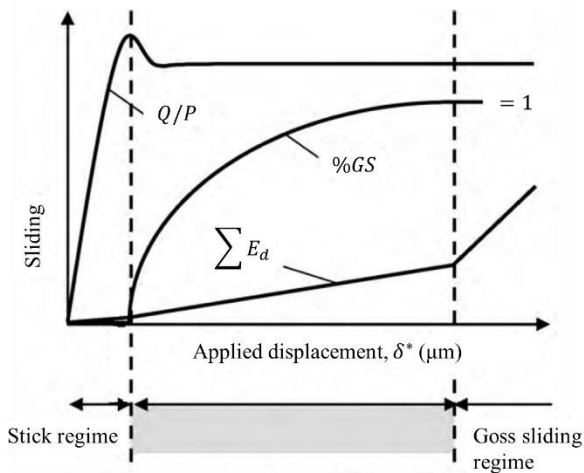


Figure 2-11– Quantitative analysis for fretting map

2.4 Fretting wear

Fretting wear is the wear caused by fretting. There are three stages for the mechanism of fretting: metal transfer caused by adhesion, generation of the

debris due to the particle detachment, and the steady-state, in which the generation and the ejection of the debris are the same [29].

The mechanical deformation causes the oxidation of the surface by absorbing the oxygen. The wear kinetics is shown in Figure 2-12 [30]. The dissipated energy leads to debris generation and relative displacement between two contact parts ejects the debris out of the contact zone. Wear kinetics is the superposition of debris generation and ejection. Fretting wear is significant in gross slip regime due to the large amount of dissipated energy. Therefore, the wear phenomenon in fretting is mostly investigated in gross sliding regime [31, 32]. With the increment of the slip amplitude, the wear mechanism changes from adhesive wear to abrasive wear and oxidation [33].

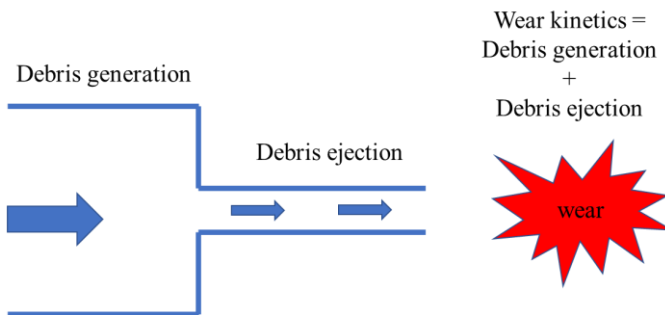


Figure 2-12– Schematic of fretting wear kinematics

Fretting wear is troublesome in power industry and turbine engine, which is mostly caused by the vibration or hoisting [30, 34]. The optical graphs of the wear scar for the blade-disc connection for turbine engine and connection between steel wires are shown in Figure 2-13 [30, 35]. The wear on the parts can make the connection loose and make the machine not to operate properly. For the hoisting wires used for example in coal mines, the fretting wear can reduce the strength of the wire, which may cause accident due to the sudden fracture of the wire.

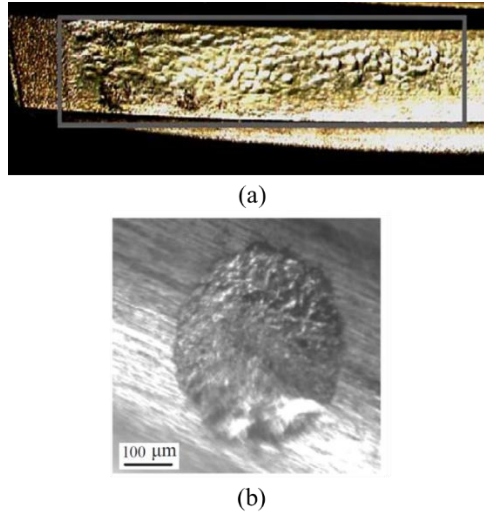


Figure 2-13– Optical graphs of fretting wear phenomenon observed in: (a) blade-disc connection, (b) connection between steel wires

To resist the wear in fretting process, the effect of heat treatment, reinforcement and surface modification are investigated commonly [36]. For example, Chen et al. analysed the effect of the T6 heat treatment on the wear resistance for aluminium alloy matrix composite and found that the T6 heat treatment offers a better wear resistance by low wear volume and coefficient of friction. In addition, Nimura et al. found that the contact surface with embedded hard particles could possess very good wear resistance property in both dry and lubricated conditions [36]. Moreover, Sato et al. found the most effective lubricants for the resistance of fretting wear through experiments [37].

To quantify the effect of wear in fretting process, many researchers have tried through experiments, analytical solution, and simulations. Therefore, in the following subsections, the basic theory of wear and up to date research are presented.

2.4.1 Wear models

There are two typical wear models that can be used for the fretting wear analysis: Archard's model and dissipated energy model. The theories and applications of these two wear models are given in the following subsections.

2.4.1.1 Archard's model

The calculation of the wear rate in fretting process is mostly based on the Archard's equation [38]:

$$\frac{V}{s} = kF \quad (2.10)$$

Where V is the wear volume, F is the load, s is the sliding distance and k is the special specific wear rate, which has the SI-dimension m^2 / N . Moreover, the k -value is related to the material properties, surface roughness and other parameters [39].

Based on this equation, McColl et al. [40] used the modified Archard's equation to obtain the local wear depth on contact surface. The modified Archard's equation is given by:

$$\Delta h(x) = K_A \times 4\delta(x) \times p(x) \times \Delta N \quad (2.11)$$

Where the subscript x is position on contact surface, K_A is the Archard's wear coefficient, $\delta(x)$ is the local relative slip amplitude, ΔN is the jump cycles, $p(x)$ is the local contact pressure and $\Delta h(x)$ is the wear depth. K_A is assumed to be a constant along the contact surface.

2.4.1.2 Dissipated energy model

Through experiments, Fouvry et al. found that the total wear volume tends to be proportional to the accumulated dissipated energy and presented the

dissipated energy equation, Eq. (2.12) [41, 42]. And it is concluded that compared with the Archard's wear model, dissipated energy model can consider the variable coefficient of friction.

$$W_V = K \sum E_d \quad (2.12)$$

Where the W_V is the wear volume, K is the energy wear volume coefficient and $\sum E_d$ is the accumulated dissipated energy. The experimental definition of the wear volume wear coefficient is shown in Figure 2-14 [42]. From the figure, we can see that the positive linear relationship between accumulated dissipated energy and wear volume is obvious. Moreover, a threshold, E_{dth} is found to activate the wear. This period is the tribologically transformed structure (TTS) phase.

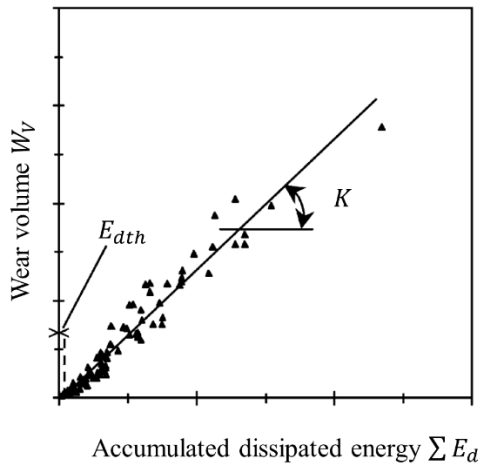


Figure 2-14— Definition of the wear volume wear coefficient, K and threshold of dissipated energy to activate the wear, E_{dth}

Zhou and Sauger proposed and analysed TTS in the fretting process, which is the transition phase between the bulk material and debris [43-45]. The fretting

wear process can be divided into three phases: I) running in stage (plastic deformation accumulation); II) TTS formation (TTS volume increases dramatically), III) stable stage (the volume of the destruction of TTS and formation of debris is the same) based on the experimental results, as shown in [46, 47]. The debris formation begins at the beginning of stage III. In most research, this phenomenon is ignored. The wear coefficient is commonly obtained by averaging the cycles wear volume and is applied to all the cycles of fretting in the FE model. It is interesting to consider the change in the wear coefficient during and after the running-in stage.

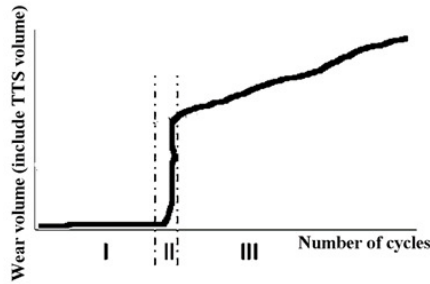


Figure 2-15– Schematic of three stages for fretting wear

To apply the dissipated energy equation to the fretting wear model, the local wear depth based on the energy density equation can be obtained as [48]:

$$\Delta h_i(x) = K_D \int_0^T q_i(x) ds_i(x) \quad (2.13)$$

Where the subscript i means the i^{th} cycle, T is the period for one cycle, K_D is the local energy wear coefficient, $q_i(x)$ and $ds_i(x)$ are the shear stress and the slip at the x position, respectively and $\Delta h_i(x)$ is the wear depth. In general, the local wear coefficient is the same as the overall energy wear coefficient K .

2.4.2 Critical role of loading conditions and material properties

There are many factors that have a critical effect on the fretting wear in fretting process. These factors can be classified into loading conditions and material properties. Coefficient of friction, surface roughness, hardness etc., are material properties, while the normal loading and slip amplitude are loading conditions. Experimental investigation on the effect of loading conditions and material properties are presented below.

Cruzado et al. analysed the effect of normal load and slip amplitude on the wear coefficient for steel wire and found that the higher load can lead to a higher wear coefficient [49]. In addition, with higher load and slip amplitude, the transition from running-in stage to stable stage is delayed. From the experiments, we can see that the wear coefficient is not a constant in the whole fretting process. Different materials possess different material properties. Xianglong et al. analysed the effect of normal load and slip amplitude for alloy 690 and found that higher normal load and slip amplitude led to a lower wear coefficient, which is a reverse tendency compared with the steel wire mentioned above [50]. Moreover, when the normal load and sliding amplitude is low, the abrasive wear mechanism dominants, while when the normal load and slip amplitude is higher, delamination wear play a more important role. Other researchers also analysed the effect of the slip amplitude or normal load effect on the fretting wear mechanism and wear coefficient, from which we can see that the effect of the normal load and slip amplitude are significant [33, 51, 52]. Moreover, the geometry and the cross angle for the steel wires can also affect the wear mechanism and wear coefficient in fretting process [53, 54].

The coefficient of friction is not a constant in fretting process and it changes with loading conditions and atmospheres [55]. The temperature can also affect the fretting wear mechanism. With higher temperature, the adhesive wear mechanism tends to be dominant and the threshold from partial slip regime to gross slip regime increases with the increases of the temperature [56-58]. Effect of hardness of the material is not significant and the wear mechanism

is almost the same by comparing the hardened and non-hardened material [59, 60]. However, hardened material shows a positive effect when considering the wear coefficient and the crack length [61, 62].

2.4.3 Numerical modelling of fretting wear

2.4.3.1 Numerical models without debris layer

FEM is widely used in fretting wear analysis, due to its high efficiency and applicability. Based on Archard's equation and dissipated energy equation, finite element (FE) models are designed to model the fretting wear surface evolution. Examples of FE models without considering debris layer are listed below.

McColl et al. first implement the fretting wear simulation based on Archard's wear model by commercial software ABAQUS [40]. The wear profile after each increment due to the node movement on contact surface and the node movement amplitude was calculated in user subroutine UMESHMOTION. The evolution of the stresses and the wear profiles are investigated numerically, and the numerical wear profiles agrees well with the experimental results. After this implementation of fretting wear simulation, more and more cases of fretting wear are analysed numerically.

Yue and Li analysed the effect of the variable coefficient of friction and found that variable wear coefficient had a significant effect in partial slip regime and the contact pressure in variable coefficient of friction model in the whole process also differed with that in constant coefficient of friction model [63, 64]. Kyvia et al. [65] described a multiscale method to take the roughness of the contacting surfaces into account and transform the roughness in microscale to the macro dimension and analyse the fretting wear in the macro model, which is a typical homogenization method. The schematic diagram is shown in Figure 2-16. In the micro model, the random local roughness is generated based on the experimental parameters R_q and ζ , where R_q is the root mean square of the roughness and ζ is the horizontal distribution factor of the

roughness. The contact pressure in the micro model with the random roughness can be obtained using Kernel smoothing. Then, Eq. (2.14) can be used to calculate the equivalent radius of the fretting pad based on the maximum pressure from the Kernel smoothing. After which the wear profile is predicted based on the fretting pad with the equivalent radius R_E . The results of this multiscale method showed better agreements with the experiment results when compared with the model without considering roughness.

$$R_E = \frac{FE'}{\pi p_{max}^2} \quad (2.14)$$

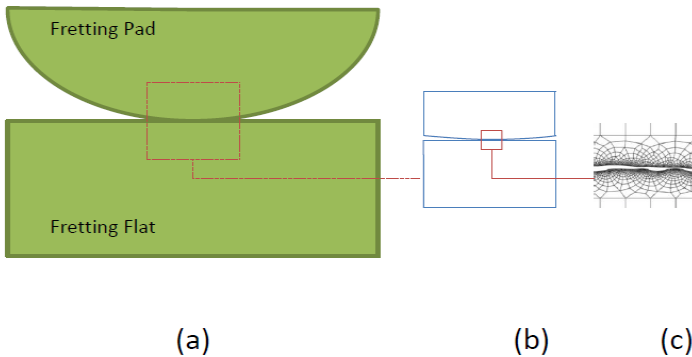


Figure 2-16– Schematic of the fretting wear model with roughness: (a) macro model, (b) micro model, and (c) local roughness

Besides the FEM, 3D fretting wear model were also used based on boundary element method (BEM) [66]. The Holm–Archard linear wear law was applied and the geometry change of the contact surface was not via the remeshing of the surface, but the gap variable, which made the process more efficient. BEM was also used to simulate the fretting wear for the fibre-reinforced materials [67]. Moreover, combined finite-discrete element method (FDEM) was applied to model the coated and uncoated surfaces in fretting wear process [68]. Lee et al. analysed the tube-to-plate contact structure by influence function method [69]. The two-dimensional contact model was established by

Cauchy integral equation. And this method was computationally effective compared with FEM.

2.4.3.2 Numerical models with debris layer

In fretting process, third bodies are formed due to the particle detachment, which can affect the stress distribution and the wear characteristics. In this thesis the effect of the debris in fretting fatigue is also analysed. Therefore, the numerical modelling of fretting wear considering the effect of the third bodies in fretting process is presented as follows.

Yue and Abdel Wahab [70] investigated the effect of the debris on the fretting wear process using a 2D FE model based on the dissipated energy equation. In this model, the profile of the debris is obtained from the wear profile of the contact part after certain cycles. The debris is introduced into the model after 500, 1500 or 2500 cycles, and the model simulated the wear profile for the next 500 cycles with debris. Then, the FE model without debris was used until the final number of cycles. In this model, the debris is set to be a constant, e.g., 5 μm , 10 μm , and 15 μm . In the whole process, the effect of the debris is only considered in the running in stage and the third bodies are assumed to be ejected after the running in stage.

Ding et al. [71] also proposed a FE based method to analyse the effect of the debris in the fretting wear as shown in Figure 2-17. In Figure 2-17, M_1 is the cylinder, M_2 is the plate, M_3 is the debris layer, τ_1 is the boundary between cylinder and debris layer, τ_2 is the boundary between the plate and the debris layer and τ_3 is the up surface of the debris layer. In this model, the plasticity of the debris was considered. Moreover, the evolution of the debris layer was predicted based on the assumption that the debris delaminated from τ_2 became part of the debris layer and the debris generated from M_1 was removed from the contact surface. τ_1 was assumed to be a contact pair and FEM based on modified Archard's model was used for the calculation of the profile evolution of τ_3 . As for τ_1 , it was calculated based on the local contact pressure and slip on the interface of τ_1 . In this way, the thickness of the debris

layer was not a constant in the fretting process. This model took the debris kinetics into account.

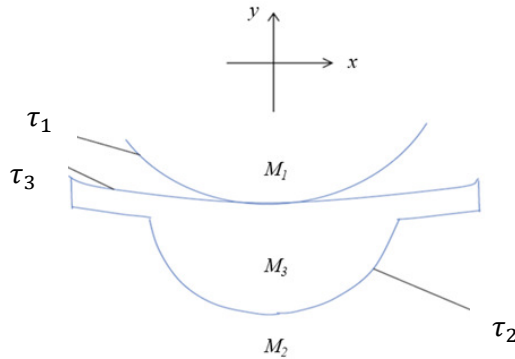


Figure 2-17– Schematic of the fretting wear model with the debris layer

Yue & Abdel Wahab [70] and Ding et al. [71] only analysed the effect of the debris generated from the specimen, however, the debris generated from the cylinder was not analysed. Arnaud et al. [72] proposed a fretting wear model that could consider the wear of both the cylinder and the specimen. The debris flowchart is shown in Figure 2-18.

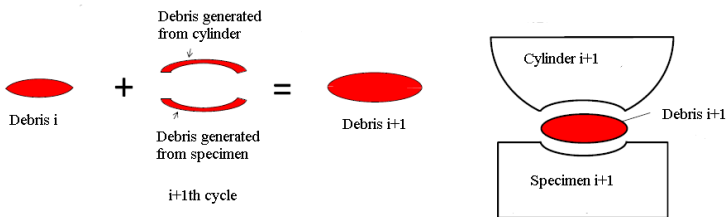


Figure 2-18– Debris layer updating model

It is obvious that the debris generation of the cylinder and the specimen can be considered in this model. Moreover, the ratio of the generated debris

thickness to the wear evolution height is introduced to take the debris ejection into account, which can get better results for the predicting of the wear profile. However, the elliptical debris layer is not a stable state. Due to the tangential shear stress between the debris layer and the cylindrical pad, the top of the debris layer can be removed. Therefore, the elliptical debris layer in Figure 2-18 is not an ideal model.

In a FE model of fretting wear with debris, the profile of the debris is considered as a layer, which is a continuum model and does not offer the insight into the granular structure of the layer. Benjamin [73] proposed FDEM to analyse the effect of the third body in fretting wear. In a combined FDEM, explicit FE method is used to solve the internal stresses, while the discrete element method is used to solve the contact interaction. The first bodies are designed by FEM, while the third body particles are designed by discrete element method. The schematic model is shown in Figure 2-19.

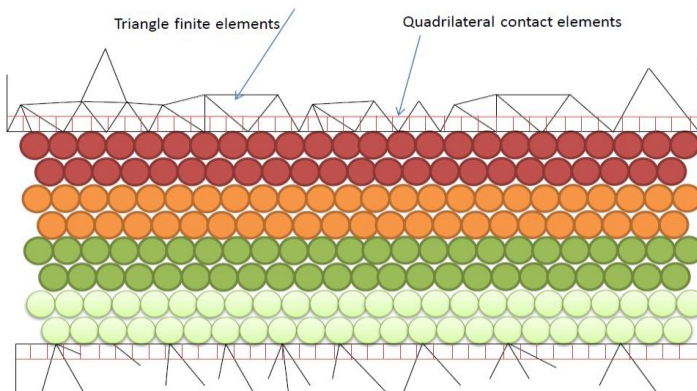


Figure 2-19– Schematic diagram of the debris layer in FDEM

The triangular finite elements of the first bodies' surfaces are replaced by a row of quadrilateral contact elements along the first-body surfaces for solving the contact interaction by the penalty method [74]. The FDEM based wear prediction was validated and found to be in good agreement with the

experiments [75]. FE method is based on Continuum Mechanics and the contact interaction is solved by the Lagrange multiplier. Discrete element method is used mainly for discontinuous geometry or contacting particles, but it cannot be used to model a continuous body. For FEM, grid distortion can happen in the simulation and a large stiffness matrix should be solved, while for DFEM a complex non-linear mechanical model must be solved. The accuracy and efficiency of both FEM and DFEM have no significant difference. However, the choice between FEM and DFEM depends on the physical properties of the debris. The geometry of the debris in fretting is different from case to case. In most experiments, the debris is a compact layer because of the normal load. Therefore, FEM is used in this thesis to design the debris layer.

2.4.4 Fretting wear test rig

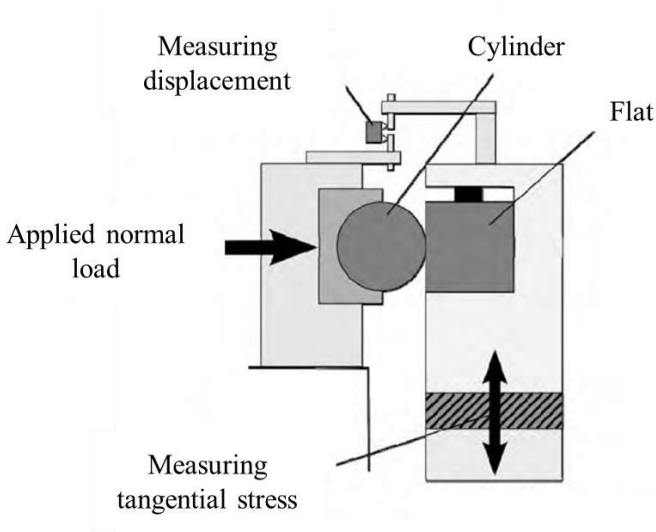


Figure 2-20– Schematic of the test rig for fretting wear

The commonly used fretting wear testing rig is shown in Figure 2-20 [30, 76, 77]. The cylinder and the flat are fixed, and an oscillatory displacement is applied on the cylinder by a hydraulic tension-compression machine. The relative displacement and the tangential load are measured to generate the fretting loops in the fretting process, which can be used to distinguish the fretting regimes as shown in Figure 2-7.

The applied displacement by hydraulic machine is the global slip amplitude, while the relative slip on the contact surface is the actual slip amplitude. The actual slip displacement is not the same as the global slip amplitude due to the plastic accommodation and the rig compliance [78, 79]. The relationship between the global and actual displacement is determined by rig compliance and coefficient of friction [80]. The actual slip amplitude is given by Eq. (2.15). Where C_{COF} is a constant which is related to the coefficient of friction, C_{rig} is a constant, which is related to the test rig and δ_{global} is the global slip amplitude.

$$\delta = \delta_{global} \frac{C_{COF}}{C_{rig}} \quad (2.15)$$

2.5 Fretting fatigue

Fretting fatigue is another damage caused in fretting process. Compared with the normal fatigue, the fretting fatigue can reduce the fatigue initiation lifetime up to more than 50% [81]. Cracks nucleates earlier in life and then they begin to propagate [82]. Therefore, there are two phases in fretting fatigue: crack initiation and crack propagation. There are many factors that can affect the lifetime for both crack initiation and propagation in fretting process. The main factors are slipping amplitude, contact configuration, surface condition, axial load, and the coefficient of friction [83-85]. Fretting fatigue is a multiaxial fatigue, therefore, many multiaxial fatigue criteria has been applied to analyse the crack initiation lifetime for fretting fatigue.

To make the background of fretting fatigue more readable, the basic theories for plain fatigue is presented in the first subsection, and then the background and literature review for fretting fatigue crack initiation and propagation are given in the following two subsections, respectively. Thereafter, the fretting fatigue test rig is described to make the mechanism of fretting fatigue more intuitive.

2.5.1 Basic theories of plain fatigue

Fatigue is the failure caused by varying load. The terms and the loading history for the plain fatigue is shown in Figure 2-21. S_a is the stress amplitude, S_r is the stress range, and S_m is the mean stress. σ_{max} is the maximum stress and σ_{min} is the minimum stress. The ratio between σ_{max} and σ_{min} is the stress ratio, R . The loading period between two maximum point is one cycle. When $R = -1$, it is the alternating load, when $R = 0$ it is varying load, and when $R = 1$ it is static load.

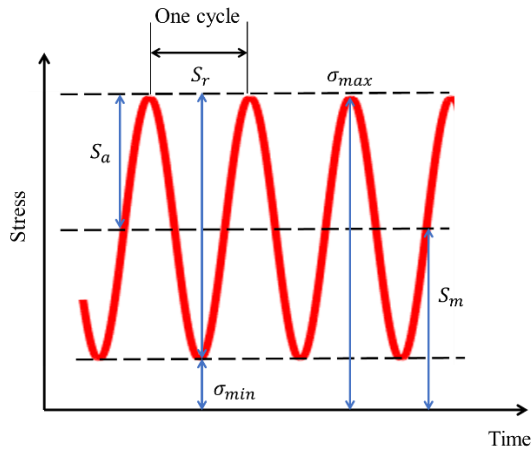


Figure 2-21– Loading history and terms for plain fatigue

For the plain fatigue, the relation between the fatigue strength and the lifetime is usually described in S-N curve, which is shown in Figure 2-22. S_f is the fatigue limit, under which the part possesses infinite lifetime. Finite lifetime of the part is found in the zone above S_f .

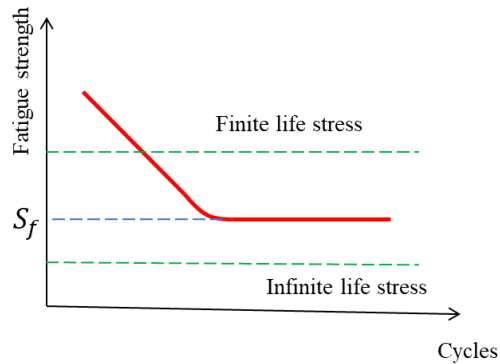


Figure 2-22– S-N curve for plain fatigue

According to the number of cycles to the failure, fatigue can be classified into high cycle fatigue (HCF) and low cycle fatigue (LCF). The threshold from HCF to LCF is about 10^5 cycles. In HCF, the stress is much lower than the yield stress and no significant plastic deformation is caused in the cycles. For LCF, the stress is near or higher than the yield stress and significant elastic or plastic strain is caused during the cycles.

There are three stages in the fatigue. Firstly, the nucleation of the crack happens due to the slip band in grains, which is an irreversible damage of the microstructure. Then, micro-crack grows to macro-crack in propagation stage. Finally, a sudden fracture of the material happens. In the first stage, the crack nucleation is sensitive to the local stress concentration and the crack propagates to grain size. In the second stage, long crack propagates in the direction of maximum principal stress. Unstable crack growth is found in the third stage.

Schematic of the crack propagation in grain scale and intrusion and extrusion in sub-grain scale under tensile loading is shown in Figure 2-23. From Figure 2-23 (a), we can see that the intrusion and extrusion in sub-grain scale occur in the direction of the maximum shear stress. Then, in the uniaxial tensile test, we assume the angle between the shear stress plane and the tensile stress is θ , the maximum tensile force is F and the cross section of the cylinder part on shear stress plane is $A/\sin\theta$. Then the shear stress on the plane can be derived from Eq. (2.16). From this equation, we can conclude that the shear stress reaches the maximum value when θ is 45° . Therefore, in Figure 2-23 (b), the micro crack begins to propagate in a direction of about 45° .

$$\tau_\theta = \frac{F \cos\theta}{A/\sin\theta} \quad (2.16)$$

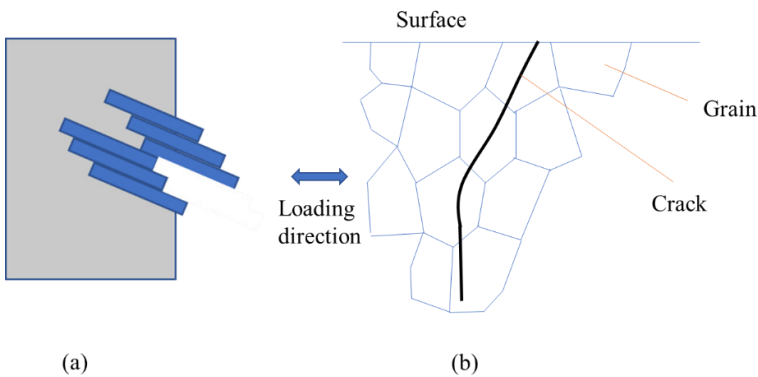


Figure 2-23– Schematic of the intrusion and extrusion in sub-grain scale and crack propagation in grain scale under tensile loading

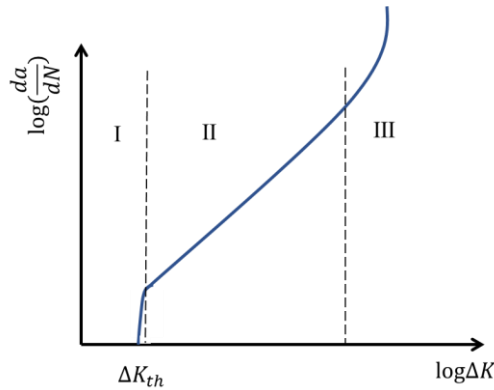


Figure 2-24– Crack growth behaviour

After the crack initiation from microstructure scale as shown in Figure 2-23 (b), crack propagation starts. A question arises: How to define the crack growth rate in crack propagation? The empirical crack growth behaviour is shown in Figure 2-24, which is mostly used for high cycle fatigue with the same stress amplitude without corrosive effect. In stage I, there is a crack growth threshold, ΔK_{th} , after which there is a stable crack growth. There is no significant boundary between the crack initiation and stage I of the crack propagation. Therefore, the initial crack length for crack propagation is important to distinguish the phase of crack initiation and propagation. Paris-Erdogan law shows the relation between the crack length and the stress intensity factor range in stage II crack propagation, which is given in Eq. (2.17). Where a is the crack length, N is the number of cycles, C and m are material constants, and ΔK is the stress intensity range. In stage II, the relationship between $\log\left(\frac{da}{dN}\right)$ and $\log\Delta K$ is linear and the propagation of the crack is relatively stable. In stage III, unstable crack growth happens, and the fracture process is near quasi static fracture. At the end of stage III, the stress intensity factor range, ΔK , approaches $(1 - R)K_c$, where R is the stress ratio and K_c is the fracture toughness of materials.

$$\frac{da}{dN} = C\Delta K^m \quad (2.17)$$

In engineering application, stage II is commonly used as the propagation phase. The cycles of crack propagation can be obtained by:

$$N_p = \int_{a_0}^{a_f} \frac{da}{C\Delta K^m} \quad (2.18)$$

Where a_0 is the initial crack length and a_f is the final crack length. C and m can be obtained by experiments or S-N curve. Due to the complexity of the loading conditions, ΔK should be defined specifically, and is given by:

$$\Delta K = Y\Delta\sigma\sqrt{\pi a} \quad (2.19)$$

Where Y is the function of the geometry of the part and $\Delta\sigma$ is the stress range at the crack tip.

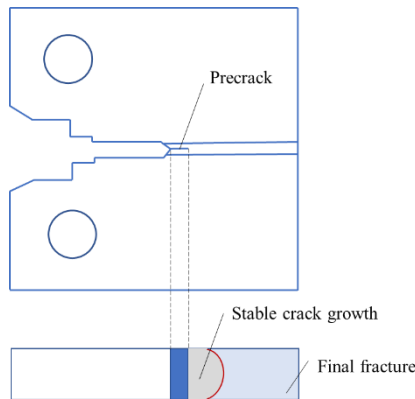


Figure 2-25– Schematic of compact tension specimen and cross-section of its crack

To analyse the fracture mechanism, toughness of the material is essential, which is commonly obtained by the fracture mechanics testing. Compact tension specimen is commonly used for the material toughness testing. The schematic of compact tension specimen and cross-section of its crack is shown

in Figure 2-25. Stable crack growth stage happens at first at the front of the precrack, after which there is a sudden final rupture.

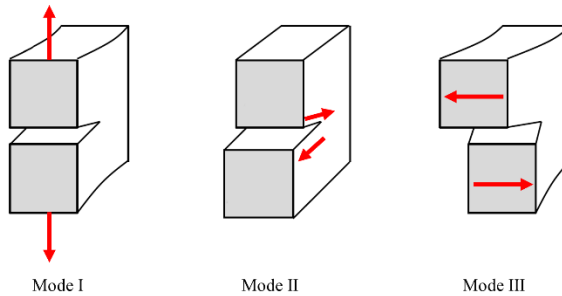


Figure 2-26– Loading modes of crack opening

There are three types of crack opening according to the loading modes as shown in Figure 2-26. In model I, the crack opening load vertical to the crack surface is applied. In model II, the in-plane shear load is applied, while in mode III, the out of plane shear load is applied.

2.5.2 Crack initiation in fretting fatigue

Compared with the plain fatigue crack initiation, there are many differences for the fretting fatigue crack initiation. Fretting fatigue is a kind of multiaxial fatigue, for which contact is essential. Moreover, the normal load and the axial load is not always proportional and in phase [86]. All these conditions make fretting fatigue a complex stress condition in the process. Therefore, multiaxial fatigue criterion is used for fretting fatigue to predict the crack initiation location. The common experientially used fatigue criteria are critical plane methods, Ruiz parameters and continuum damage mechanics. These theories are described in the following subsections.

2.5.2.1 Critical plane methods

Many multiaxial fatigue criteria have been used for fretting fatigue analysis. Critical plane approaches are mostly used due to their applicability and generality [87]. There are three kinds of critical plane methods, namely stress-based, strain-based, and energy-based critical plane method. Findley parameter (FP), Fatemi-Socie parameter (FS) and SWT are the corresponding three kinds of critical plane methods. The three critical plane method are presented below.

FP criterion is firstly proposed by Findley in Ref. [88], which is a typical critical plane method to calculate direction and position of crack nucleation in early stage [2]. FP is given by [89]:

$$FP = \frac{\Delta\tau_{max}}{2} + k_1\sigma_n^{max} \quad (2.20)$$

Where $\Delta\tau_{max}$ and σ_n^{max} are the maximum range of shear stress and the maximum normal stress on the critical plane in one fretting cycle, respectively. k_1 is determined by the fatigue limit in tension σ_{f-1} and torsion τ_{f-1} when the stress ratio R is equal to -1. k_1 is determined from:

$$\frac{\sigma_{f-1}}{\tau_{f-1}} = \frac{2}{1 + \frac{k_1}{\sqrt{1 + k_1^2}}} \quad (2.21)$$



Figure 2-27– Sketch of the angle of the critical plane on one point

To determine the angle of the critical plane, θ varying from -90° to 90° is used to get the maximum shear stress range on one point as shown in Figure 2-27.

The stress and strain condition on the critical plane can be obtained by Eqs. (2.22), (2.23), (2.24), and (2.25). x' and y' mean the rotated Cartesian coordinate. These equations can be used to obtain the damage parameters on the corresponding critical plane for all the critical plane methods.

$$\sigma_{x'} = \frac{\sigma_x + \sigma_y}{2} + \frac{\sigma_x - \sigma_y}{2} \cos 2\theta + \tau_{xy} \sin 2\theta \quad (2.22)$$

$$\tau_{x'y'} = -\frac{\sigma_x - \sigma_y}{2} \sin 2\theta + \tau_{xy} \cos 2\theta \quad (2.23)$$

$$\varepsilon_{x'} = \frac{\varepsilon_x + \varepsilon_y}{2} + \frac{\varepsilon_x - \varepsilon_y}{2} \cos 2\theta + \frac{\gamma_{xy}}{2} \sin 2\theta \quad (2.24)$$

$$\gamma_{x'y'} = -\frac{\varepsilon_x - \varepsilon_y}{2} \sin 2\theta + \frac{\gamma_{xy}}{2} \cos 2\theta \quad (2.25)$$

FP is used to predict the crack initiation time and the equation for lifetime prediction is given by [90, 91]:

$$FP = \tau'_f (2N_i)^{b'} \quad (2.26)$$

Where τ'_f is the coefficient of shear fatigue strength, N_i is the crack initiation lifetime and b' is exponent of torsion fatigue strength.

Fatemi and Socie proposed a strain-based critical plane method, FS as shown in Eq. (2.27) [92]. Where $\Delta\gamma_{max}$ is the maximum shear strain range and σ_n^{max} is the corresponding normal stress. σ_y is the yield stress and k_2 is the material constant, which is approximately equal to σ_y/σ'_f [93]. The relationship that links FS and crack initiation lifetime is given in Eq. (2.28) [94]: where γ'_f is the shear fatigue ductility coefficient, G is the shear modulus, b' is fatigue strength exponent in torsion, and c' is fatigue ductility exponent in tension.

$$FS = \frac{\Delta\gamma_{max}}{2} \left(1 + k_2 \frac{\sigma_n^{max}}{\sigma_y}\right) \quad (2.27)$$

$$FS = \frac{\tau_f'}{G} (2N_i)^{b'} + \gamma_f' (2N_i)^{c'} \quad (2.28)$$

Another critical plane method, *SWT*, which is an energy-based method, is also applied in this thesis. *SWT* is used as a criterion for fretting fatigue by Szolwinski and Farris which is given in Eq. (2.29) [95].

$$SWT = \sigma_n^{max} \frac{\Delta\varepsilon_n}{2} \quad (2.29)$$

Where σ_n^{max} is the maximum normal stress, while $\Delta\varepsilon_n$ is the corresponding strain amplitude. The equation that connects *SWT* and crack initiation lifetime, N_i is given by:

$$SWT = \frac{\sigma_f'^2}{E} (2N_i)^{2b} + \sigma_f' \varepsilon_f' (2N_i)^{b+c} \quad (2.30)$$

Where σ_f' is the fatigue strength coefficient, ε_f' is the fatigue ductility coefficient, E is the Young's modulus, b is the fatigue strength exponent, and c is the fatigue ductility exponent. b' and c' are the same as b and c , respectively.

2.5.2.2 Ruiz parameter

Ruiz et al. used two damage parameters to analyse the fretting phenomenon in a dovetail joint at the first time [96]. The first damage parameters, $F1$ is proportional to the frictional energy per unit area, which is given by [97]:

$$F1 = \tau \cdot \delta \quad (2.31)$$

Where τ is the shear stress on the contact surface and δ is the relative slip between two contact surfaces. This parameter can be used to indicate the extent of the surface material removal, because the frictional energy is proportional to the material removal in dissipated energy wear model [96]. It should be noted that in fretting process, the shear stress is always changing with loading history in one cycle. However, $F1$ is the value at the maximum loading case and in this equation, the tensile stress applied on the specimen is not considered.

To consider the tensile stress, the second damage parameter, $F2$ is used as:

$$F2 = \tau \cdot \delta \cdot \sigma_{xx} \quad (2.32)$$

Where σ_{xx} is the tensile stress. $F1$ can be used for the maximum wear damage location. However, the maximum wear damage location usually differs from the crack initiation point due to the competence between the wear and crack initiation. Through experiments, it was observed that $F2$ could be used for the prediction of crack initiation point.

2.5.2.3 Continuous damage mechanics

Damage mechanics can be used to estimate the damage evolution based on the effective stress. Kachanov used thermodynamics laws to combine the damage with stresses and strains [98]. The effective stress in representative volume element as shown in Figure 2-28 is given by:

$$\tilde{\sigma} = \frac{F}{S - \Delta S} \quad (2.33)$$

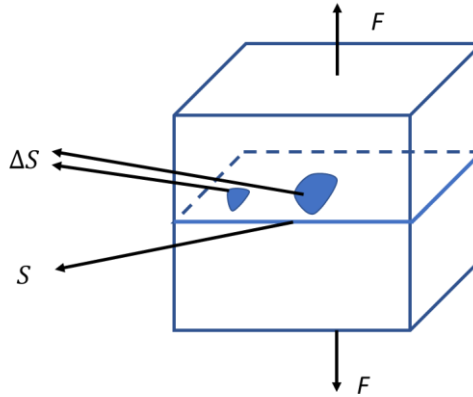


Figure 2-28– Schematic of the representative element

Where F is the axial load for representative volume element, S is the whole area of the cross-section and ΔS is the area with damage or void in S . The stiffness of the material decreases with the increment of the damage area. The damage variable, D can be expressed by Eq. (2.34) [99]:

$$D = \frac{\Delta S}{S} \quad (2.34)$$

When D is 0 if there is no damage for the material, while when D is 1 if is a crack in the corresponding cross-section.

Continuous damage mechanics can be used to solve low cycle fatigue, creep, and high cycle fatigue. Fretting fatigue is a kind of high cycle fatigue mostly. Therefore, in this section the damage models for high cycle fatigue are given. Lemaitre explained the damage evolution for high cycle fatigue by dissipated potential energy [100]. The corresponding dual dissipation potential function, which is based on thermodynamics force, is given by [101]:

$$\phi(Y, \dot{Y}) = \frac{C}{(\beta/2) + 1} \left(\frac{-Y}{C} \right)^{(\beta/2)+1} (\dot{Y}) \quad (2.35)$$

Where C and β are constants and Y is the corresponding damage strain energy release rate, which is obtained by Eq. (2.36), where σ_{eq} is the equivalent stress, R_v is the triaxiality function, and σ_H is the hydrostatic stress [102]. The triaxiality equation is given by Eq. (2.37):

$$Y = \frac{\sigma_{eq}^2}{2E(1-D)^2} R_v \quad (2.36)$$

$$R_v = \frac{2}{3}(1+\nu) + 3(1-2\nu) \left(\frac{\sigma_H}{\sigma_{eq}} \right)^2 \quad (2.37)$$

The differential function of Y with respect to time can be given by:

$$\dot{Y} = \frac{dY}{dt} = \frac{2\sigma_{eq}\dot{\sigma}_{eq}}{2E(1-D)} R_v \quad (2.38)$$

Derivative of the damage variables with respect to time can be obtained by the derivative of ϕ with respect to Y is given in Eq. (2.39), where the linear accumulation of the strain energy rate is assumed:

$$\dot{D} = -\frac{\partial\phi}{\partial Y} = \left(\frac{-Y}{C} \right)^{\beta/2} (-\dot{Y}) \quad (2.39)$$

By integrating Eq. (2.39), we can get the damage variables in one cycle as:

$$\frac{\partial D}{\partial N} = \int_{t_1}^{t_2} \dot{D} dt = \int_{\sigma_{eq,min}}^{\sigma_{eq,max}} \frac{A\sigma_{eq}^{\beta+1} R_v^{\frac{\beta}{2}+1}}{(1-D)^{\beta+2}} d\sigma_{eq} \quad (2.40)$$

Where β and A are material constants, and $\sigma_{eq,max}$ and $\sigma_{eq,min}$ are maximum and minimum equivalent stresses, respectively. The result of Eq. (2.40) can be expressed by Eq. (2.41).

$$\frac{\partial D}{\partial N} = A \frac{(\sigma_{eq,max}^{\beta+2} - \sigma_{eq,min}^{\beta+2})}{(1-D)^{\beta+2}} R_v^{-\frac{\beta}{2}-1} \quad (2.41)$$

When N is 0, the damage variable tends to be 0. Therefore, we can get the damage variable by Eq. (2.42). When D is equal to 1, then we can get the crack initiation lifetime N_i using Eq. (2.42).

$$D = 1 - [1 - A(\beta - 3) (\sigma_{eq,max}^{\beta+2} - \sigma_{eq,min}^{\beta+2}) R_v^{\frac{\beta}{2}+1} N]^{\frac{1}{\beta+3}} \quad (2.42)$$

Hojjati-Talemi et al. applied the continuous damage mechanics to predict the location of the crack initiation position [102]. However, the above-mentioned continuous damage model is commonly used for the proportional loading, in which R_v is considered as a constant in the loading process. To apply this continuous damage model to the non-proportional loading cases, Nadeem and Wahab proposed a continuous damage model considering the variation of R_v with time [103].

2.5.3 Crack propagation of fretting fatigue

In this thesis, the crack initiation of fretting fatigue is analysed. Although crack propagation is not applied in the thesis, some basic theories are given in this subsection. After the crack initiation process, an initial crack with certain angle is formed. Then the crack propagation is next phase for fretting fatigue. The initial crack length for crack propagation can be defined by [104]:

$$a_0 = \frac{1}{\pi} \left(\frac{\Delta K_{th}}{\sigma_e} \right)^2 \quad (2.43)$$

Where ΔK_{th} is the minimum stress intensity factor range that can give rise to crack propagation, and σ_e is the fatigue limit of the material. Self-arrest phenomenon happens to the crack if the stress intensity factor range is below ΔK_{th} .

The orientation of crack propagation can be predicted and quantified by fracture mechanics, while the loading cycles can be predicted by crack growth law given in Eq. (2.18). In fracture mechanics, there are two fracture theories: linear-elastic fracture mechanics (LEFM) and elastic-plastic fracture mechanics (EPFM).

Irwin proposed Stress intensity factors (SIFs) to quantify the stress singularity ahead of the crack [105]. From then on, SIFs are commonly used as the underlying principle of LEFM to characterise the crack propagation. In LEFM, SIFs near the crack tip in mode I loading condition as shown in Figure 2-29 can be expressed as:

$$K_I = Y\sigma_\infty\sqrt{\pi a} \quad (2.44)$$

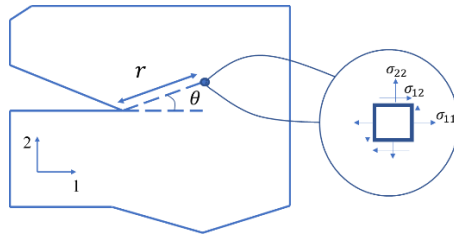


Figure 2-29– Schematic of crack and the point near the crack tip

Where Y is the dimensionless geometry factor, σ_∞ is the stress as the crack tip, and a is the half crack length. From this equation, it can be concluded that SIFs are affected by applied stress, size of the crack and the geometry of the specimen. Energy release rate, which is also defines as crack driving force is

a dual of stress intensity factor. The energy release rate for Mode I is given by:

$$G_I = \frac{K_I^2}{E'} \quad (2.45)$$

Where $E' = E$ for plane stress and $E' = \frac{E}{(1-\nu^2)}$ for plan strain. The stress field ahead of the crack tip for linear elastic material can be written as [106]:

$$\sigma_{ij}(r, \theta) = \left(\frac{K_I}{\sqrt{2\pi r}} \right) f_{ij}^I(\theta) + \left(\frac{K_{II}}{\sqrt{2\pi r}} \right) f_{ij}^{II}(\theta) + \left(\frac{K_{III}}{\sqrt{2\pi r}} \right) f_{ij}^{III}(\theta) \quad (2.46)$$

Where K is SIFs, the subscripts I, II and III are the modes of the loading, r is the distance from the crack tip to the point and $f_{ij}(\theta)$ is a known dimensionless function of θ .

In fretting fatigue, the LEFM is commonly used to predict the fretting fatigue crack propagation lifetime. A stepwise crack propagation model is usually used for the prediction of the propagation path. The SIFs near the new crack tip is shown in Figure 2-30. The relation between SIFs at the previous crack tip and SIFs at new crack tip is given by Eq. (2.47).

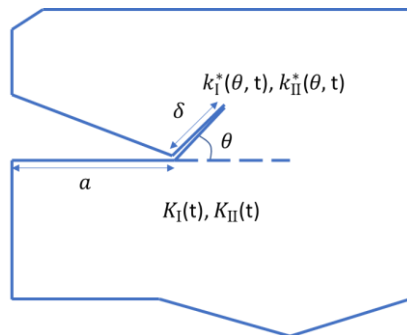


Figure 2-30– SIFs near the tip of the new crack

Where $k_I^*(\theta, t)$ and $k_{II}^*(\theta, t)$ are the SIFs at the tip of the new crack, while $K_I(t)$ and $K_{II}(t)$ are SIFs at the tip of the previous crack. θ is the angle between the new crack and previous crack.

$$\begin{bmatrix} k_I^*(\theta, t) \\ k_{II}^*(\theta, t) \end{bmatrix} = \begin{bmatrix} K_{11}(\theta) & K_{12}(\theta) \\ K_{21}(\theta) & K_{22}(\theta) \end{bmatrix} \begin{bmatrix} K_I(t) \\ K_{II}(t) \end{bmatrix} \quad (2.47)$$

Where $K_{11}(\theta)$, $K_{12}(\theta)$, $K_{21}(\theta)$, and $K_{22}(\theta)$ are function of θ [107]. By using this equation, we can get the crack orientation angle θ_p using one of the following methods: maximum tangential stress criterion (MTS), maximum energy release rate criterion and $K_{II} = 0$ criterion [108-110].

LEFM is only valid when the nonlinear material deformation is near the crack tip and small-scale yielding is assumed. Then an alternative EPFM is required. Compared with LEFM, the stress around the crack tip in EPFM is totally different. In EPFM, J integral acts the same as G in LEFM. J is equal to G in linear elastic condition, which can be obtained by Eq. (2.48), in which U is the internal strain energy and da is the incremental crack length.

$$J = -\left(\frac{dU}{da}\right) \quad (2.48)$$

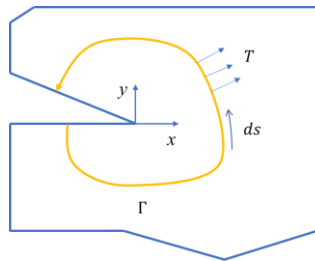


Figure 2-31– Path integral of J

J can be used as a path integral as shown in Figure 2-31, which can be obtained by [106]:

$$J = \int_{\Gamma} (w dy - T_i \frac{\partial u_i}{\partial x} ds) \quad (2.49)$$

Where w is the strain energy density, T_i is the traction vector and u_i is the displacement component. w and T_i can be obtained by Eq. (2.50) and Eq. (2.51), respectively. Γ is a counter clockwise integral path, which can be selected randomly.

$$w = \int_0^{\epsilon_{ij}} \sigma_{ij} d\epsilon_{ij} \quad (2.50)$$

$$T_i = \sigma_{ij} n_j \quad (2.51)$$

The same as the stress near the crack tip in LEFM, the stress near the crack in EPFM can be expressed as:

$$\sigma_{ij} = \sigma_y \left(\frac{Ej}{\alpha I_n r \sigma_y^2} \right)^{\frac{1}{n+1}} \tilde{\epsilon}_{ij}(n, \theta) \quad (2.52)$$

Where I_n and $\tilde{\epsilon}_{ij}(n, \theta)$ are the function of n and θ , α is usually take as $0.002 / \epsilon_y$.

J -Integral can only be used to obtain a value of fracture energy release rate, which is difficult to segregate the total energy release rate to three modes of fracture. Yau et al. proposed M -Integral which is an interaction integral to extract the stress intensity factor for three fracture modes from the energy release rate by J -Integral for linear elastic material [111]. In M -Integral, two solutions are assumed:

$$\sigma_{ij} = \sigma_{ij}^{(1)} + \sigma_{ij}^{(2)}, \epsilon_{ij} = \epsilon_{ij}^{(1)} + \epsilon_{ij}^{(2)}, u_i = u_i^{(1)} + u_i^{(2)} \quad (2.53)$$

Substituting displacement, stress and strain fields to Eq. (2.49) to J -integral leads to:

$$J = J^{(1)} + J^{(2)} + M^{(1,2)} \quad (2.54)$$

Where:

$$J^{(1)} = \int_{\Gamma} (w^{(1)} dy - T_i^{(1)} \frac{\partial u_i^{(1)}}{\partial x^{(1)}} ds) \quad (2.55)$$

$$J^{(2)} = \int_{\Gamma} (w^{(2)} dy - T_i^{(2)} \frac{\partial u_i^{(2)}}{\partial x^{(2)}} ds) \quad (2.56)$$

$$M^{(1,2)} = \int_{\Gamma} (w^{(1,2)} dy - T_i^{(1)} \frac{\partial u_i^{(2)}}{\partial x^{(1)}} ds - T_i^{(2)} \frac{\partial u_i^{(1)}}{\partial x^{(1)}} ds) \quad (2.57)$$

$M^{(1,2)}$ is the M -Integral, in which $w^{(1,2)} = \sigma_{ij}^{(1)} \epsilon_{ij}^{(2)} = \sigma_{ij}^{(2)} \epsilon_{ij}^{(1)}$. The relationship between J -integral and stress intensity factors for mixed modes can be found in Ref. [112], while the relationship between M -Integral and stress intensity factors can be found in Ref. [113].

2.5.4 Numerical modelling of fretting fatigue

After the description of the theories about the crack initiation and propagation for fretting fatigue, the numerical modelling of crack initiation and propagation is given in the following subsections, respectively.

2.5.4.1 Crack initiation

There are many numerical models to analyse the crack initiation of fretting. For the homogeneous material, the crack initiation position mostly locates on the contact surface. Many researchers have applied FEM to the analysis of the fretting fatigue crack initiation for complex coupling and crystal plasticity

finite element method (CPFEM) to the microstructure analysis of the crack initiation. The stress and strain on the contact surface are commonly extracted from the nodes to get the corresponding value of crack initiation parameter in FEM and then predict the lifetime and initiation position. Here, some examples of the numerical modelling are given as follows.

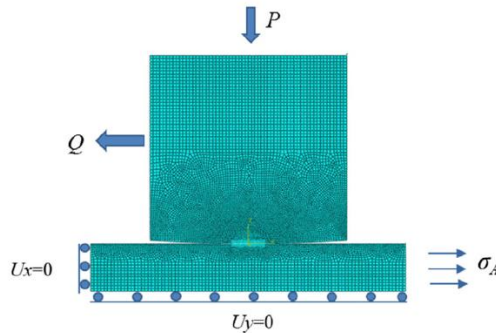


Figure 2-32– FE model of cylindrical pad on flat specimen

Tsai and Mall first applied FEM to the analysis of stress in fretting fatigue for cylinder-on-flat configuration by commercial software ABAQUS [114]. Then, Naboulsi and Mall predicted the crack initiation behaviour by shear stress range (MSR), modified SWT and FP using FEM [115]. The cylinder-on-flat configuration is commonly used to analyse the fretting fatigue phenomenon as shown in Figure 2-32 [116]. The commonly used in phase loading condition is shown in Figure 2-33. Bhatti et al. analysed the effect of out phase loading conditions by critical plane methods and continuum damage mechanics [86, 116, 117]. The effect of out of phase loading conditions is significant and should be considered carefully for the actual mechanical configurations. Moreover, the effect of the void in the material is analysed on the contact stress condition and fretting fatigue crack initiation [118, 119]. The results show that the position and size of the void have a significant effect on the stress state and the crack initiation position.

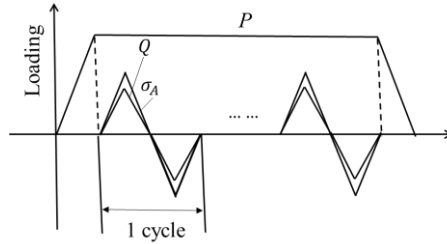


Figure 2-33– In phase loading conditions of fretting fatigue

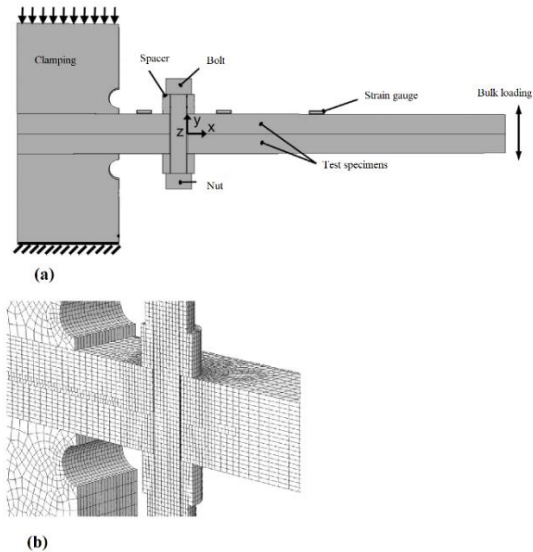


Figure 2-34– Bending fretting fatigue of bolt connection: (a) sketch of the bolt connection and loading condition, (b) FE mesh for the configuration

Other complex configurations are also analysed to investigate the fretting fatigue besides the cylinder on flat configuration. Lanoue et al. analysed the fretting fatigue strength for interference fit of the shaft and hub [120]. The results show that the mesh refinement, contact algorithm, high stress gradient etc., can affect the prediction accuracy. Ding et al. analysed the fretting fatigue

phenomenon in complex coupling and found that the SWT and Ruiz parameters obtained by FEM shows a good agreement with the experimental results [121]. Moreover, D_{fret} was used to consider the effect of wear on fretting fatigue. Juoksukangas et al. analysed the bending fretting fatigue between the bolt and test specimen as shown in Figure 2-34 [122]. The fatigue life decreases when the bulk bending load increases and when the preload of the bolt increases.

2.5.4.2 Crack propagation

In the numerical modelling of crack initiation of fretting fatigue, there is no crack in the model and only the stress and strain states near the contact surface are analysed. In this subsection, the numerical modelling of crack propagation is presented. Extended finite element method (XFEM) and ‘seam’ in ABAQUS are commonly used to model the crack in fretting fatigue. XFEM can be used to model the crack by adding the degree of freedom of the nodes near the crack as shown in Figure 2-35. The schematic of the crack in XFEM is shown in [123]. There are two more DOFs for Heaviside enriched nodes and eight more DOFs for crack tip enriched nodes. The standard formulation for the displacement approximation is given by [124]:

$$u_{XFEM}(x) = \sum_{i \in \Omega} N_i(x) u_i + \sum_{i \in \Psi} N_i(x) H(x) a_i + \sum_{i \in K} \left[N_i(x) \sum_{\alpha=1}^4 F_{\alpha}(x) b_{i\alpha} \right] \quad (2.58)$$

$H(x)$ is the Heaviside function and is equal to ± 1 , which cause a discontinuity on the crack. Ω is the set for all the nodes, Ψ is the set for Heaviside enriched nodes and K is the set for crack tip enriched nodes. a_i and $b_{i\alpha}$ are the corresponding DOFs of $H(x)$ and $F_{\alpha}(x)$, respectively. $F_{\alpha}(x)$ is the crack tip function, which can be obtained by:

$$[F_{\alpha}(r, \theta), \alpha = 1 - 4] = \left[\sqrt{r} \sin \frac{\theta}{2}, \sqrt{r} \cos \frac{\theta}{2}, \sqrt{r} \sin \frac{\theta}{2} \sin \theta, \sqrt{r} \cos \frac{\theta}{2} \sin \theta \right] \quad (2.59)$$

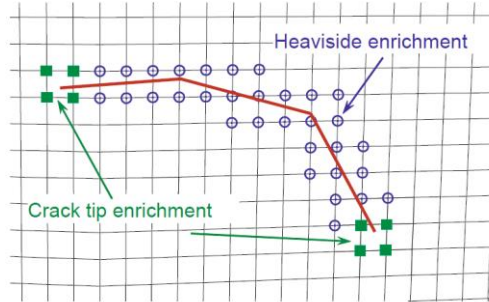


Figure 2-35– Schematic of the enrichment of the nodes in XFEM: circle is the Heaviside enrichment, and square is the crack tip enrichment

If there is no crack in FE model, the classical FE approximation equation can be obtained by:

$$u_{FE}(x) = \sum_{i \in \Omega} N_i(x) u_i \quad (2.60)$$

Giner et al. proposed an ABAQUS implementation of XFEM for crack propagation by using user subroutine UEL [123]. Then this method was used to analyse crack propagation for fretting fatigue [125-127]. And criteria of $\max(k_I(\theta, t))$, $\max(\Delta k_I(\theta))$ and $\frac{da}{dN}(\theta)$ are used to determine the crack propagation angle as described in Figure 2-30. Then, Paris-Erdogan law is used to get the corresponding crack propagation length for certain jump cycle. In XFEM, the crack is independent of the mesh. Therefore, there is no need to update the mesh with the increment of the crack path. Moreover, combined cohesive zone method and XFEM are applied to analyse the crack propagation of fretting for complete contact by Pereira et al. [128].

Besides XFEM, ‘seam’ in ABAQUS is also used to predict the lifetime of the fretting fatigue crack propagation [110, 129]. The mesh of the crack generated by seam in ABAQUS is shown in Figure 2-36. The limitation of seam in

ABAQUS is that the mesh should be updated with the propagation of the crack in FE model.

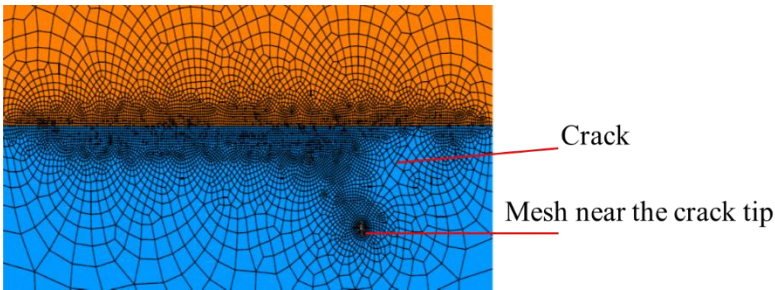


Figure 2-36– Mesh of crack generated by seam in ABAQUS

2.5.5 Fretting fatigue test rig

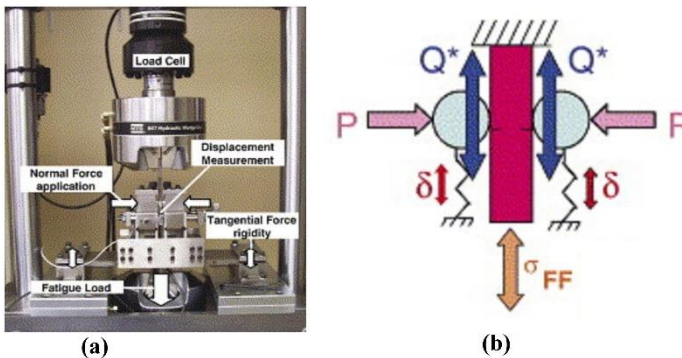


Figure 2-37– Fretting fatigue test rig: (a) apparatus for the experiments, and (b) schematic of the test rig

The test rig of fretting fatigue for cylinder-on-flat configuration is shown in Figure 2-37 [61]. Compared with the loading conditions of fretting wear, axial load is applied for the specimen and the tangential displacement is substituted by the tangential load. For flat-on-flat configuration, tangential load is not applied [126]. Beside the axial load, torsional load can also be used as a cyclic

fatigue load [130]. The radius of the cylindrical pad, normal load, tangential load, and axial load can all affect the crack initiation and propagation significantly. Therefore, these parameters are important input for the experiments.

2.6 Interaction between fretting wear and fretting fatigue

In mixed slip regime, there is a competence between wear and fatigue. In gross sliding regime, the initiation of micro crack can be moved away when the wear is significant, which can prolong lifetime of the parts. Researchers have made a lot of efforts to investigate the crack initiation point and crack propagation path in fretting process [87, 89, 131-133]. The assumptions for these analyses are that the geometry change on the contact surface caused due to the wear is neglected. Moreover, only one cycle of fretting is used to analyse the stress state to get the crack initiation time. In the real case, the surface geometry change has effect on the stress state near the contact surface, which is the critical zone for crack initiation. In this way, the analysis of one cycle is not enough to consider the stress and strain states in fretting process.

2.6.1 Effect of wear on crack initiation

Some researchers have done some works to investigate the effect of fretting wear on crack initiation. Madge et al. [134, 135] analysed the critical role of wear on fatigue in fretting process for both gross slip regime and partial slip regime. They found that competence between the wear and fatigue crack initiation on the contact surface was significant and the wear had alleviated the fatigue damage initiation significantly. Shen et al. [136] considered the wear effect on fretting fatigue lifetime of crack initiation by damage-coupled elastic-plastic constitutive model, in which the effect of plasticity on damage accumulation and wear characteristics were presented in detail. To increase the accuracy of the prediction, a parameter D_{fret2} was introduced to combine

the Smith Watson Topper (*SWT*) by Ding et al. [137] to considered the wear effect in fretting process, in which the frictional work threshold $(\tau\sigma)_{th}$ was used as an indicator to distinguish the zone where wear is dominant. In addition, O'Halloran et al. [138] validated this parameter by cylinder on flat specimen configuration and found that this method can reduce the computation time significantly. This was because the wear depth computation on contact surface was not necessary for combined D_{fret2} -*SWT*.

2.6.2 Effect of wear on crack propagation

The fretting wear affect not only the crack initiation, but also the crack propagation. The effect of wear on crack propagation is also significant, which is caused by the redistribution of the shear stress [139]. The implementation of crack propagation through commercial software ABAQUS in fretting was first proposed by Giner [123, 140]. Llavori et al. analysed the wear profile effect on crack propagation and found that the considering wear can obtain a more accurate crack propagation path and propagation lifetime. Hattori and Watanabe investigated the effect of wear on crack propagation of fretting fatigue based on stress intensity factor by both FEM and experiments and found that the fatigue strength decreased with the evolution of the wear profiles [141]. Steel wires are commonly used for the transmitting electricity or supporting. Wang et al. analysed the dynamic wear characteristics of steel wires in fretting process and the effect of these wear characteristics on crack propagation [142]. It is concluded that the elliptical wear scar and parabolic wear depth were found and fitted well with the prediction fitting equation and larger crack depth was founded in the centre of the crack zone. Moreover, the effect of cross angle and friction-increasing grease effect between steel wires were also analysed in [143] and [144], respectively.

2.7 Prediction methods

Researchers have made a lot of efforts to analyse the wear in fretting process through both simulations and experiments [40, 70, 145-148]. The characteristics of wear can be measured by experiments under certain loading conditions. However, the setup is time-consuming. Therefore, simulation is an alternative technique for the prediction of the wear characteristics based on experimental material properties. Among the simulation methods, FEM is most popular due to its wide applicability. Wear characteristics can be predicted through simulations under different loading cases efficiently by FEM. To make the prediction more accurate and efficient, predictive methods can be applied to engineering data under many loading cases and environmental circumstances. In engineering problems, sometimes the loading conditions are different from case to case. In this thesis, an inverse analysis of wear characteristics is presented through Proper Orthogonal Decomposition with Radial Basis Function (POD-RBF) based on the simulation data is proposed. In this way, we can predict the wear characteristics under different loading cases. In the following subsections, the prediction methods that are used in this thesis are described such as grey model, curve fitting and artificial neural network (ANN), which will be used for the comparison with POD-RBF.

2.7.1 POD-RBF

Prediction models can be used to predict the engineering data under many loading cases and environmental circumstances. In engineering problems, sometimes the loading conditions are different from case to case. In this thesis, an inverse analysis of wear characteristics is presented through Proper Orthogonal Decomposition (POD) with Radial Basis Function (RBF) based on the simulation data. In this way, we can predict the wear characteristics.

Proper Orthogonal Decomposition (POD) with Radial Basis Function (RBF) is a statistical formulation. However, POD consists of quantifying the

coherence between the values of data used to predict behaviour based on the RBF interpolation. POD is used in various fields for fast prediction such as aero-elasticity, default detection, modal analysis, multi-body system, stochastic structure dynamics, and fracture mechanics [149-153]. On the other hand, its application in the field of tribology (evaluation of the coefficient of friction and wear rate) is almost difficult to find in the literature. According to Ref. [154], it is difficult to find numerical models solving the tribological behaviour between the disc and the brake pads. Numerical prediction of wear process of an initial line contact in mixed lubrication conditions was presented by Hao and Meng [155]. Artificial neural network were used to predict the aging effects on the wear behaviour of IN706 super alloy [156] and friction characteristics of industrial brakes [157].

2.7.2 Grey model

Grey system theory first proposed by Ju-Long in 1982 [158] and it widely applied in agriculture, ecology economy, industry [159], e.g. Grey system theory compass grey relational space, grey generating space, grey forecasting, etc. Grey model (GM) is a dynamic model with a few differential equations, by using at least four data. In this thesis, GM (1, 1) is used for the prediction due to the lower data volume. It is mostly used for the prediction of the data with the same intervals for one parameter. Therefore, the interpolation to the raw data is not acceptable.

In GM (1, 1), a group of new data series with obvious trend is generated by Accumulating Generating Operation (AGO) at first, which is given by:

$$x^{(1)}(k) = \sum_{i=1}^k x^{(0)}(i); k = 1, 2 \dots n \quad (2.61)$$

Where $x^{(0)} = \{x^{(0)}(1), x^{(0)}(2) \dots x^{(0)}(n)\}$ is the raw data, and $x^{(1)} = \{x^{(1)}(1), x^{(1)}(2) \dots x^{(1)}(n)\}$ is AGO-generated data. After AGO, adjacent mean equal weight sequence is generated by:

$$z^{(1)}(k) = 0.5x^{(1)}(k-1) + 0.5x^{(1)}(k), k = 2, 3 \dots n \quad (2.62)$$

Where $z^{(1)} = \{z^{(1)}(2), z^{(1)}(3) \dots z^{(1)}(n)\}$. The equation for GM(1, 1) is established as:

$$x^{(0)}(k) + az^{(1)}(k) = b \quad (2.63)$$

Where k ranges from 1 to n and the data should be obtained with the same interval, a is the develop coefficient and b is the coefficient of grey effect. To obtain the two coefficients, the following equation is given:

$$\hat{c} = (B^T B)^{-1} B^T Y \quad (2.64)$$

Where \hat{c} is a 2×1 matrix of two coefficient a and b , respectively, Y is a $1 \times (n-1)$ matrix obtained by deleting the first element of raw data matrix whose dimension is n and B is a $2 \times (n-1)$ matrix, in which the first column is $z^{(1)}$ and in the second column, all the elements are 1.

The prediction line can be obtained by accumulated subtract operation as:

$$\hat{x}^0(t+1) = \left(\frac{1-0.5a}{1+0.5a} \right)^{t-2} \cdot \frac{b-ax^{(1)}(1)}{1+0.5a} \quad (2.65)$$

Where $x^{(1)}(1)$ is the first element of the raw data matrix and $\hat{x}^0(t+1)$ is the predicted value at variable point $t+1$.

2.7.3 Curve fitting

Two curve fitting methods are commonly used: linear regression and polynomial curve fitting (PCF). Interpolation can be implemented to the raw data for one parameter prediction. Least square method is the commonly used method for PCF. There is no specific requirement for the raw data interval and more accurate curve fitting can be obtained using more data. In this thesis,

PCF is used to compare the results with POD-RBF to determine the advantages and disadvantages of each method and it is given by:

$$f(x) = a_0 + a_1x + a_2x^2 + a_3x^3 + \dots + a_kx^k \quad (2.66)$$

Where k is the order of a polynomial, a_0 to a_k are the coefficients for each order of x and $f(x)$ is the predicted curve. To obtain the coefficients, here, the 2nd order polynomial is taken as an example as:

$$\begin{bmatrix} n & \sum x_i & \sum x_i^2 \\ \sum x_i & \sum x_i^2 & \sum x_i^3 \\ \sum x_i^2 & \sum x_i^3 & \sum x_i^4 \end{bmatrix} \begin{bmatrix} a_0 \\ a_1 \\ a_2 \end{bmatrix} = \begin{bmatrix} \sum y_i \\ \sum x_i y_i \\ \sum x_i^2 y_i \end{bmatrix} \quad (2.67)$$

Where $\sum x_i$ is the accumulated generation operation for all the x data and n is the number of x data.

2.7.4 ANN

ANN is one of the most important fields of Artificial Intelligence (AI), which consists of automating the learning of an algorithm based on collected data. Self-learning function is the main character of ANN, while the second character is searching for optimal solution with high speed. With the specific input and output, the relationship between them can be quantified by ANN and then the inner function can be used for the prediction of the given parameters. In this thesis, a supervised learning model is implemented to estimate wear characteristics, such as wear width and wear depth. The normal load, oscillatory displacement amplitude and number of cycles are taken as input, while the wear characteristics are predicted as the corresponding output data. The regression feature is investigated to estimate the size of the damaged

element. The ANN model focused on three layers of nodes including a hidden layer size, an input layer size and an output layer size.

The number of neurons per layer depends on the problems to be studied, based on the number of selected tests from the numerical or experimental analyses.

The selected data from the damage index of the proposed indicator are presented as an input layer and then are transferred to the hidden layer. To study the collected data from the first step to the last one, we have to go through the following two formulations.

$$\bar{\Phi}_j = \sum_{i=1}^n w_{ij} f_i + b_i, \quad j = 1, 2 \dots m \quad (2.68)$$

$$O_j = \frac{1}{1 + e^{-\bar{\Phi}_j}} \quad (2.69)$$

Where $\bar{\Phi}_j$ is the collected data of the j^{th} element of the hidden layer, m specifies the number of neurons used in the hidden layer and n indicates the number of elements inserted to the input layer, f_i indicates the output data of the previous layer, w and b are the weight and bias, respectively, which is used for the training. The first formulation presents the summation function based on the training parameters. After $\bar{\Phi}_j$ is defined, the next equation is used to calculate hidden layer output, O_j . Network input data may be divided into three components, namely validation, tests, and training.

2.8 Concluding remarks

In this chapter, the literature review and research background are given. Contact mechanics is the basic theory for the fretting problem, which can be used as an analytical verification method for the contact model. Then, the current research on fretting, fretting wear and fretting fatigue is presented,

which include the basic theory of wear model, fatigue crack initiation and propagation mechanism and theoretical background, numerical modelling of fretting wear and fretting fatigue. Moreover, the overview of the research on interaction between fretting wear and fretting fatigue is given. Finally, the prediction tools that are used in this thesis are described.

Chapter 3 Methodology and FE modelling

3.1 Overview

Based on the theory and background presented in Chapter 2, three models are designed in this chapter: VWCM, prediction tools to predict the wear characteristics, and combined fretting wear and fatigue model. The methodology and the FE model are given in the following sections.

3.2 Variable wear coefficient model in fretting wear

The wear coefficient is commonly considered as a constant in most FE model as described in section 2.4, whereas the experimental results show the opposite. Figure 3-1 shows the experimental wear volume variation with the number of cycles, in which the slope of the experimental wear volume line is

proportional to the wear coefficient based on Eq. (2.10) [46, 160]. The experimental set up is a ball-on-flat configuration. The corresponding loading conditions and materials are: normal load is 300 N, slip amplitude (half stroke) is 300 μm , and the radius of the ball 30 mm. The slope of the blue line in Figure 3-1 is a constant averaged only through the final wear volumes based on Eq. (2), which was used in most current research work. Through Figure 3-1, we can conclude that the wear coefficient varies with the number of cycles, which should be analysed and considered in the FE model.

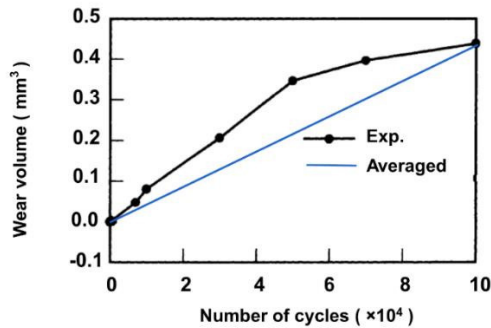


Figure 3-1– Experimental variation of wear volume with number of cycles vs wear volume in simulation

3.2.1 Experimental setup

The experimental results and set up are obtained from Ref. [46]. The geometry of the cylindrical pad and flat specimen is shown in Figure 3-2 (a), where the thickness of the flat specimen, t is 3 mm, and the diameter of cylindrical pad, D is 20 mm. The normal load, P is applied at the top of the cylindrical pad, and oscillatory displacement, δ (half stroke) is applied to the flat specimen. In this experiment, P is 1000 N and δ is 50 μm in gross sliding regime and 10 μm in partial slip regime. The applied displacement is recorded by the extensometer.

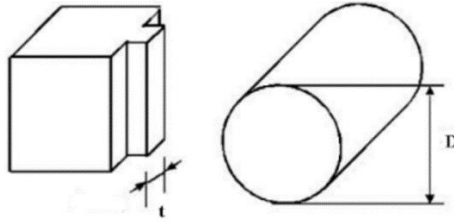


Figure 3-2– Geometry of the cylindrical pad and flat specimen

The material properties are listed in Table 3-1. The coefficient of friction (COF) is 1.0 in the stable stage as reported in Ref. [46]. The plastic strain and stress curve is based on the following equation[136]:

$$\sigma = \sigma_y + \frac{C_1}{\gamma_1} (1 - e^{\gamma_1 \epsilon_p}) + \frac{C_2}{\gamma_2} (1 - e^{\gamma_2 \epsilon_p}) \quad (3.1)$$

Table 3-1– Material properties

Young's modulus (GPa)	119
Poisson ratio	0.29
Yield stress (MPa)	970

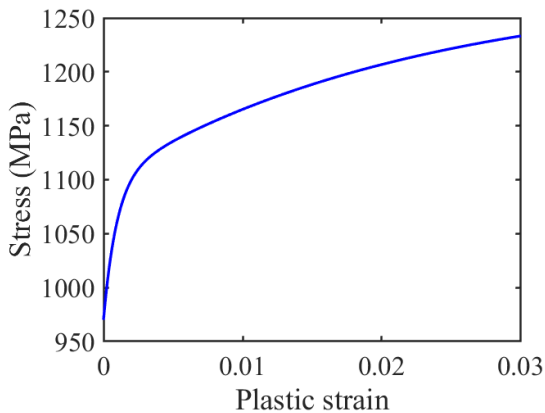


Figure 3-3– Relationship between plastic strain and stress

Where σ_y is the yield stress, and C_1 , γ_1 , C_2 , and γ_2 are material property constants and determined by experiments and the corresponding values of these constants are 136500 MPa, 1050, 8100 MPa and 45. The obtained plastic stain and stress curve is plotted in Figure 3-3.

3.2.2 Numerical models

3.2.2.1 FE model

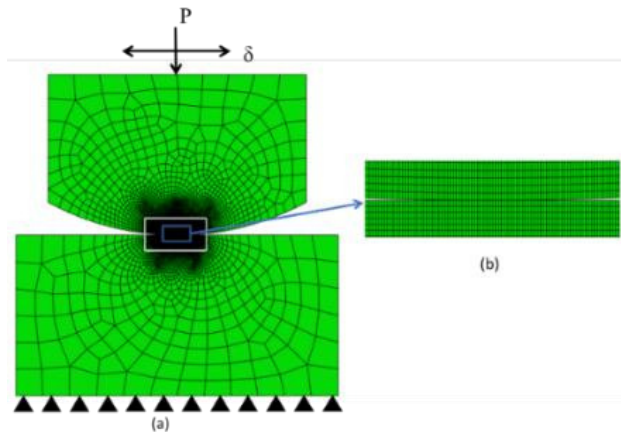


Figure 3-4– FE model: (a) FE model for the flat specimen and cylindrical specimen, and (b) partition for the contact zone

The non-linear FE model is designed in the commercial software ABAQUS by python scripts, which is shown in Figure 3-4 (a). 4-node bilinear plane strain quadrilateral (CPE4) element is applied to the whole model. The radius of the cylindrical pad is 10 mm. To consider both efficiency and accuracy of the model, the partition is used for both parts. The mesh in both contact zones is shown in Figure 3-4 (b) and the mesh size is $10 \mu\text{m} \times 20 \mu\text{m}$.

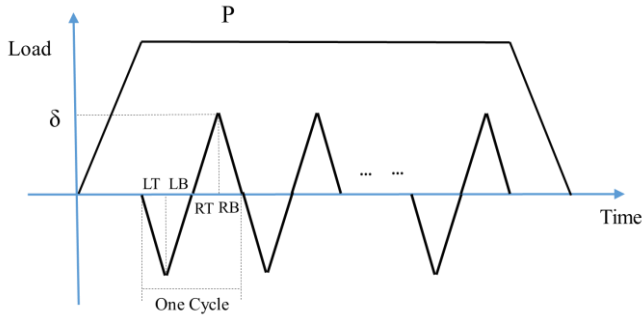


Figure 3-5– Loading history of FE model

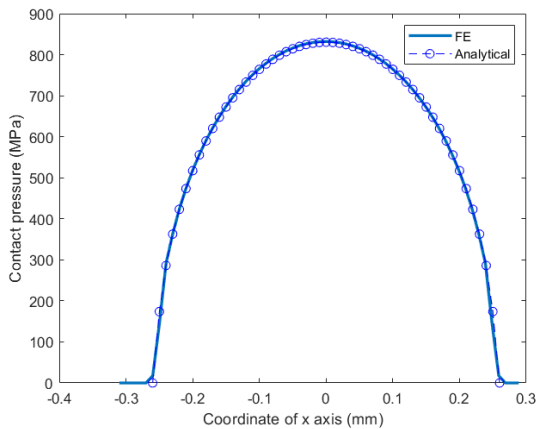


Figure 3-6– Contact pressure comparison between the FE model and analytical solution, when $P = 1000\text{ N}$

The normal load and slip between the two contact parts are both relative. To simplify the model, we apply the normal load and oscillatory displacement on the top centre of the cylindrical pad. The loading history is shown in Figure 3-5. In one cycle, there are four steps: LT, LB, RT, RB, which represent the different tangential positions of the flat. δ is the applied tangential displacement. Before the oscillatory relative slip, normal load, P is applied. Moreover, after all the cycles, there is a releasing step for the normal load. To save more computation time, jump cycle, ΔN is used, which means that after each increment the wear depth is obtained by multiply ΔN in Eq. (4). The first

2500 cycles are the TTS period, and the wear coefficient is set as 0 in this stage. To validate the FE model, the contact pressures of both FE model and analytical solution are compared as shown in Figure 3-6.

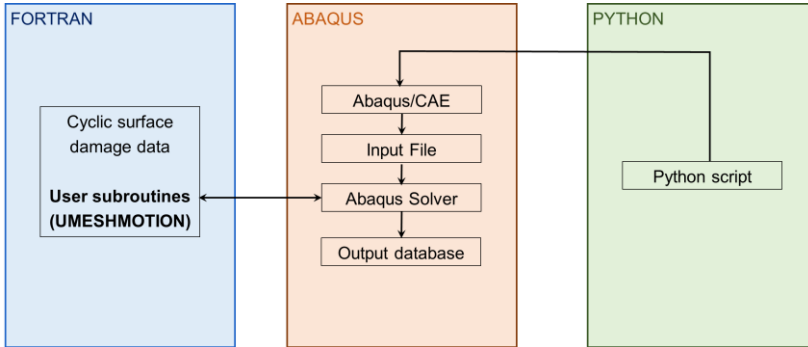


Figure 3-7– ABAQUS implementation for FE analysis of fretting wear

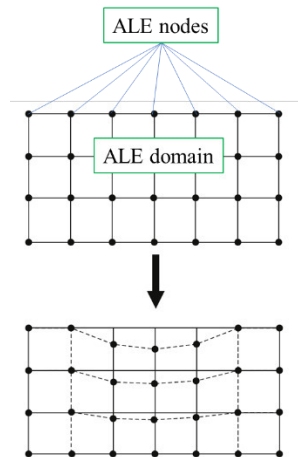


Figure 3-8– The schematic of the vertical movement for ALE nodes

The numerical analysis of fretting wear by FE model can be implemented as shown in Figure 3-7. The dissipated energy wear equation was applied in the user subroutine, UMESHMOTION by applying Arbitrary Lagrangian-

Eulerian (ALE) adaptive mesh constraints to the nodes of contact surface on the partition zone of the flat specimen as shown in Figure 3-4 (b). The partition of the specimen is set as ALE adaptive mesh domain. The schematic of the vertical movement for ALE nodes is shown in Figure 3-8 [161]. Because for fretting wear there is only material removal, only vertical node movement is obtained in UMESHMOTION. In the following FE models, the numerical modelling of fretting wear is implemented in the same way.

3.2.2.2 Modelling the variation in wear coefficient

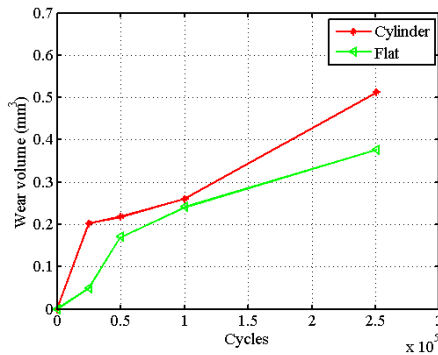


Figure 3-9– Wear coefficient changes with the number of cycles for both flat specimen and cylindrical pad

The variation of wear coefficient during the fretting process is an interesting topic. As shown in Figure 3-9, the wear coefficient of both the cylindrical pad and the flat specimen varies with the number of cycles [46]. In this section, two wear coefficient models are used, namely the constant wear coefficient model (CWCM) and VWCM. To consider this effect in the partial slip regime, the wear coefficient is taken the same as that in the gross sliding regime. By averaging each line in Figure 3-9, the Archard's wear coefficient variation with a certain cycle's period for both cylinder and flat is shown in Figure 3-11, which is used for VWCM. For CWCM, the averaged wear coefficient is obtained through the wear volume at the 25000th cycle.

To obtain the wear coefficient for every cycles' period of the flat and cylindrical pad, relative slip amplitude on the contact surface, δ should be known at first. Based on Eq. (1), the estimated wear coefficient is $9.98 \times 10^{-9} \text{ MPa}^{-1}$ in the 25000 cycles for flat. To make the wear coefficient more accurate to be used in the FE model, a wear coefficient modification method is applied as shown in Figure 3-10 [162]. From the figure, we can see that based on the estimated wear coefficient, the wear volume of FE is compared with wear volume of experiment until it meets the certain accuracy by adjusting the wear coefficient step by step. The wear coefficients for all the periods in Figure 3-9 are shown in Figure 3-11.

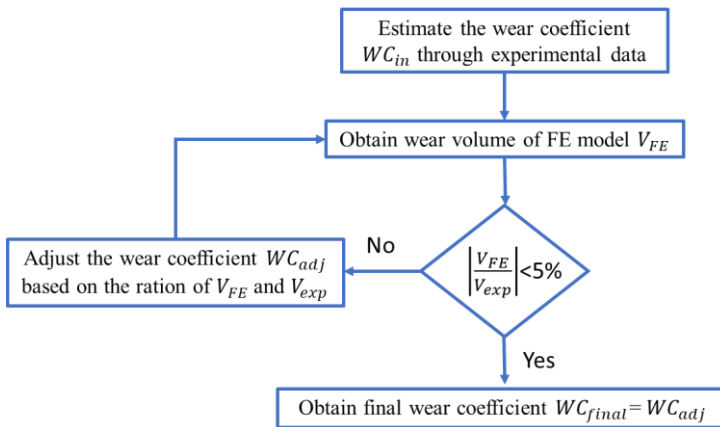


Figure 3-10– Flowchart to obtain the wear coefficient to be used in FE model

From Figure 3-11 we can see that the wear coefficient is not constant in the whole fretting process. Due to the limitation of the experimental data, we can only get the wear coefficient in a certain period. We do not know where there is a variation of wear coefficient in four cycles' intervals. We take the first 25000 cycles of the flat specimen as an example: The averaged wear coefficient is much lower in the first 25000 cycles compared with that in 25000-50000 cycles. It means that in the first 25000 cycles, there is a certain point after which the wear coefficient increased dramatically. The opposite phenomenon happens for the cylindrical pad: In the first 25000 cycles, there

is a certain value, after which there is a significant decrease in wear coefficient. Moreover, based on the experimental data of the COF[46], the first 2500 cycles are considered a TTS period, which means that the wear coefficient is 0 in this period. The averaged Archard's wear coefficients for flat and cylinder are $4.99 \times 10^{-9} \text{ MPa}^{-1}$ and $2.058 \times 10^{-8} \text{ MPa}^{-1}$ in the first 25000 cycles, respectively.

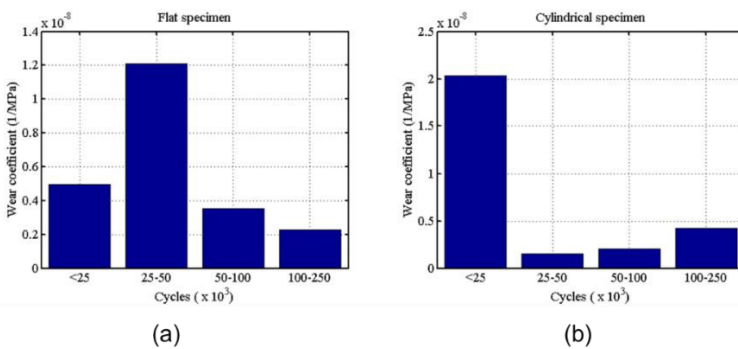


Figure 3-11– Experimental wear coefficient after certain cycles' interval: (a) Flat specimen, and (b) cylindrical pad

Validation of the wear models is done for both specimens. The cross-sections of both specimens are shown in Figure 3-12. After integrating the wear profile, the thickness is used to multiply the integration results to obtain the computational wear volume. The computational wear volumes are 0.0479 mm^3 and 0.1998 mm^3 for flat and cylindrical pad by CWCM after 25000 cycles, respectively. Compared with the experimental result, 0.0497 mm^3 and 0.2026 mm^3 , we can see that the computational wear characteristics by CWCM show a good agreement with experimental results.

In the FE model, the wear profile of the flat specimen can be obtained by export the coordinate of contact surface nodes after the fretting wear process directly. However, for the cylindrical pad, it is not the same case. The profiles of the cylinder before and after fretting wear, and profile after adjustment after 25000 cycles are shown in Figure 3-13. Due to the wear on the cylinder contact

surface, there is an overall vertical movement of the cylinder. To obtain the wear profile of the cylinder, adjustment is applied to make the profiles agree with each other, wherever there is no wear on it. Wear characteristics of both flat specimen and cylindrical specimen after 25000 cycles is obtained in Figure 3-12.

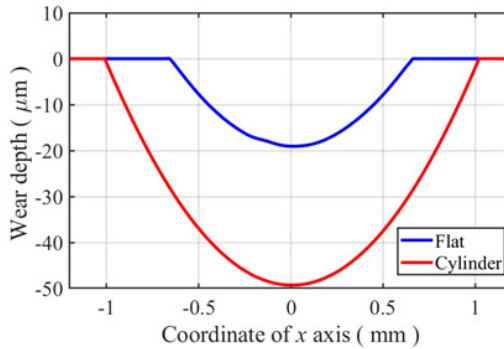


Figure 3-12– Wear characteristics of both flat specimen and cylindrical specimen after 25000 cycles

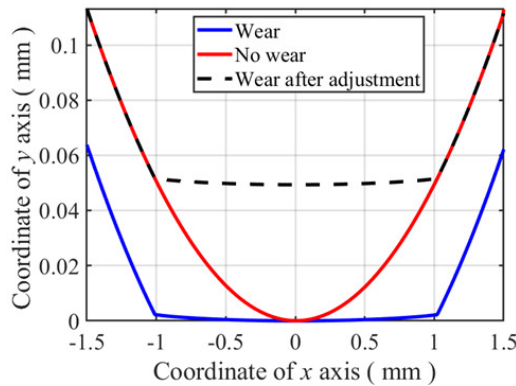


Figure 3-13– Profiles of the cylinder before and after fretting wear and the adjusted wear profile after 25000 cycles

Considering the above conditions, double linear models are used for both flat specimen and cylindrical pad in the first 25000 cycles. The wear volume after 25000 cycles is set to be the same as the experimental data for both specimens. CWCM and VWCM in the first 25000 cycles for both specimens are shown in Figure 3-14.

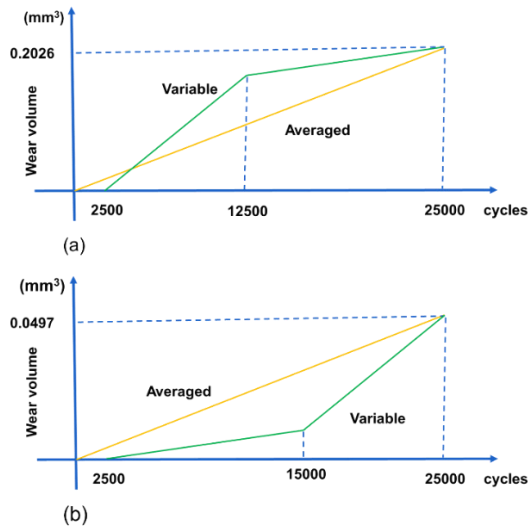


Figure 3-14— Schematic of CWCM and VWCM in the first 25000 cycles for both specimens: (a) cylindrical pad; (b) flat specimen

In Figure 3-14, for variable wear coefficient model, in the first 2500 cycles which is TTS period, no wear happens. Then, the slop of the sharp increment is assumed to be 5 times greater than that of the moderate growth and the sharp increment period is 10000 cycles, while the moderate growth period is 12500 cycles for both cylindrical pad and flat specimen. Based on Eq. (2), two variable Archard's wear coefficients, k_A are 1.996×10^{-9} and 9.98×10^{-9} for flat specimen and are 8.23×10^{-9} and 4.115×10^{-8} for the cylindrical pad. Because COF is 1.0 in the stable stage, the dissipated energy wear coefficient k_E is the same as k_A .

3.2.1 Numerical implementation

Flowchart of the numerical implementation for cylindrical pad and flat specimen is shown in Figure 3-15, where N_{inc} is the total number of increment; K_{Ej} is the wear coefficient, which changes with the number of cycles and is obtained based on Figure 3-14 for both CWCM and VWCM, and N_T is the total number of cycles. From the figure, we can see that after obtaining the simulation result of CWCM and VWCM for both specimens, post-processing and restart python code are used to get the corresponding parameters' history and profile. To obtain the wear characteristics history, a releasing step should be created at the end of each jump cycle by restarting, and the former steps after this jump cycle are deleted in the restarted CAE model.

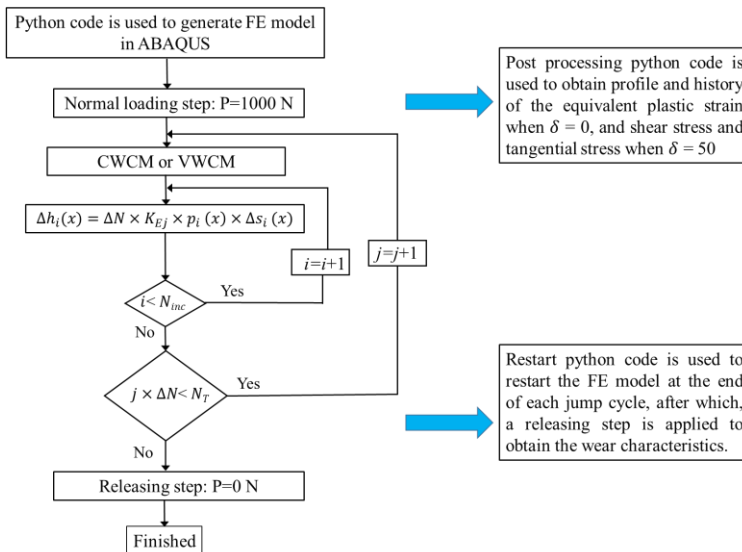


Figure 3-15– Flow chart of numerical implementation of fretting wear for cylindrical pad and flat specimen

As described in Ref. [40], the stability of the model is related to the local wear depth after each increment in the FE simulation process. The local wear depth is proportional to the jump cycles. Based on Figure 3-11 and Figure 3-14, we can see that the wear coefficient of the cylinder is much greater than that of the flat specimen. Therefore, to make the simulation process more stable, 1250 cycles and 625 cycles are used as jump cycles for flat and cylinder parts, respectively, by trial and error.

3.3 Predictive tools to predict the wear characteristics

3.3.1 Model description

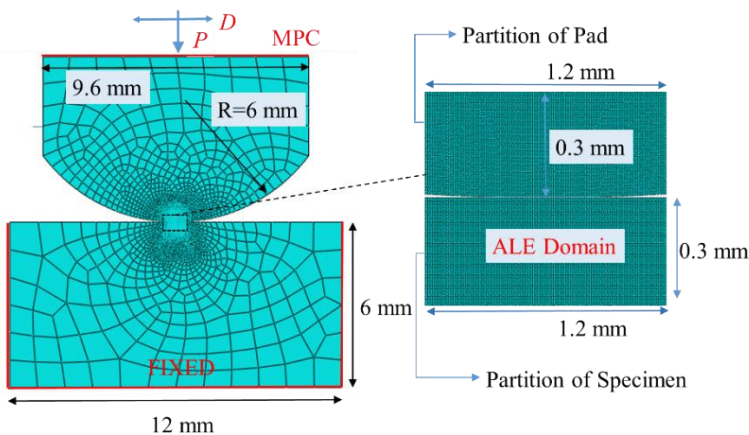


Figure 3-16– Dimensions and boundary conditions of fretting wear FE model

The dimensions and boundary conditions of the FE model are shown in Figure 3-16. The dimensions of the pad and specimen are based on the experimental set-up in Ref. [40]. The radius of the cylindrical specimen is 6 mm, and the thickness of the specimen is 10 mm. Partition is used for the contact zone to get finer mesh. The multipoint constraint is applied on the top of the pad, and

oscillatory displacement D and normal load P are exerted on the top centre of the pad. The loading history is shown in Figure 3-17. The bottom of the specimen is fixed. The partition of the specimen is set as ALE domain. In this way, the wear evolution of the specimen surface can be simulated in the fretting process using the user subroutine UMESHMOTION in the commercial software ABAQUS.

The material used in the model is super CMV steel, for which Young's modulus, E and Poisson ratio, ν are 200 GPa and 0.3, respectively, and the yield strength, σ_{yield} is 1240 MPa [163]. Elastic property is used in the model. In the referenced experiments, three normal load cases are used. Due to the effect of the normal load on the coefficient of friction (CoF) and wear coefficient, the list of these parameters based on the experiments is shown in Table 3-2 [40].

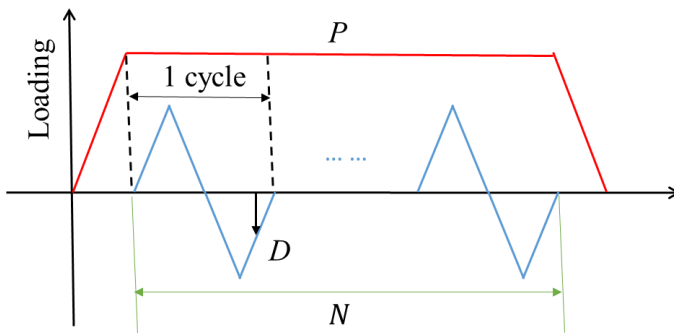


Figure 3-17– Loading history - N is the total number of cycles

Table 3-2– Normal load cases and the corresponding CoF and wear coefficient

Normal Load (N)	CoF	Wear Coefficient (MPa^{-1})
185	0.88	3.3×10^{-8}
350	0.80	5.3×10^{-8}
500	0.75	7.3×10^{-8}
1000	0.70	5.9×10^{-8}
1670	0.68	4.4×10^{-8}

3.3.2 Verification and validation of the FE model

3.3.2.1 Analytical solution for contact pressure and shear distribution

Based on Hertzian contact, the contact pressure can be obtained by Eq. (2.4) and the half contact width, b can be obtained by Eq. (2.1). The contact width, $2b$ and the maximum contact pressure, p_{max} under all the normal loads are given in Table 3-3.

Table 3-3– Contact width and maximum contact pressure for all the normal loads

Normal Load (N)	p_{max} (MPa)	$2b$ (μm)
185	328.5	71.7
350	451.8	98.7
500	540.0	117.9
1000	763.7	166.8
1670	987.0	215.6

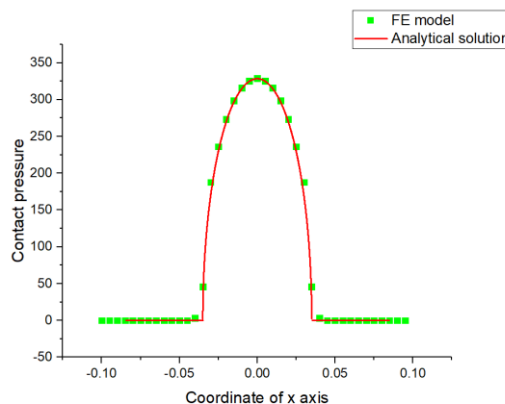


Figure 3-18– Comparison of the FE results with the analytical solution - contact pressure when P is 185 N

Figure 3-18 shows that the contact pressure results of the FE model have a good agreement with analytical solution when the normal load is 185 N, which means that the boundary condition and mesh of FE model are properly applied.

Moreover, Mindlin-Cattaneo shear distribution in partial slip regime is used to verify the FE model, Eq. (3.2) is used. Compared with the equation in (2.9), the axial load is not considered. Therefore, the offset, e is considered as 0.

$$\begin{cases} q(x) = \mu p_{max} \sqrt{1 - \left(\frac{x}{a}\right)^2}, & c < |x| < a \\ q(x) = \mu p_{max} \sqrt{1 - \left(\frac{x}{a}\right)^2} - \mu p_{max} \frac{c}{a} \sqrt{1 - \left(\frac{x}{c}\right)^2}, & |x| < c \end{cases} \quad (3.2)$$

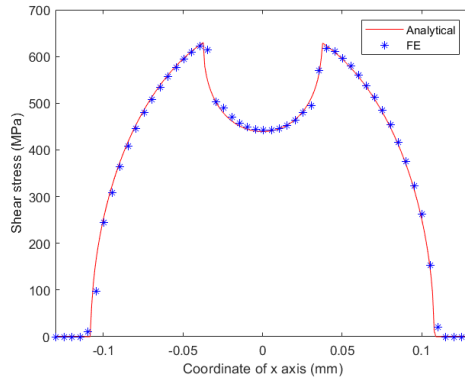


Figure 3-19– Mindlin-Cattaneo shear distribution comparison between analytical and FE results ($Q = 1000$ N and $P = 1670$ N)

Where $q(x)$ is the shear stress along the contact width, μ is CoF, and c is the half stick width. c can be obtained by:

$$c = b \sqrt{1 - \left| \frac{Q}{\mu P} \right|} \quad (3.3)$$

Where Q is the tangential load. The $Q = 1000$ N is applied on the left side of the pad and the normal load, $P = 1670$ N is applied on the top center of the pad. The analytical and FE results are compared in the following figure. It can be seen in Figure 3-19 that the FE point fits the analytical curve well.

3.3.2.2 Mesh size convergence study

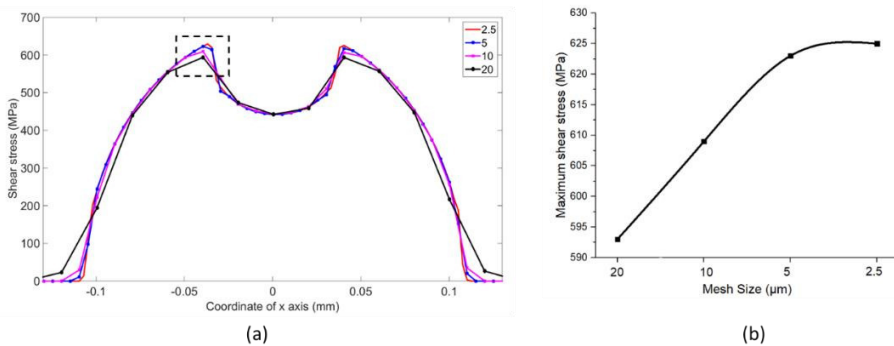


Figure 3-20– Shear stress for different mesh size and the maximum stress trend versus mesh size- $P = 1670$ N, $Q = 1000$ N

The mesh size should be fine enough because of the high stress gradient in the fretting wear process. Therefore, the mesh convergence investigation is applied. Shear stress is used to calculate the wear depth along the contact surface after each increment in FE model. Therefore, the Mindlin-Cattaneo shear distribution is used to select the proper mesh contact size both considering the efficiency and accuracy. Contact mesh sizes of $2.5 \mu\text{m}$, $5 \mu\text{m}$, $10 \mu\text{m}$ and $20 \mu\text{m}$ are applied to the partition zone of the flat and the specimen. The shear stress for all the mesh sizes and the trend of maximum shear stress versus mesh sizes are shown in Figure 3-20 when P is 1670 N and Q is 1000 N. It can be concluded that from mesh size $5 \mu\text{m}$ the maximum shear stress in the dotted rectangle tends to be equal to the next mesh size. Therefore, $5 \mu\text{m}$ is used as the proper mesh size in the model.

3.3.2.3 Experimental results of wear profile

To further validate the wear model implemented by FE method, the wear profile after 18000 cycles when the applied displacement is $25\ \mu\text{m}$ as for normal load $185\ \text{N}$ and $1670\ \text{N}$, is shown in Figure 3-21 (a) and (b), respectively. The simulation results show high accuracy compared with the experimental results. The FE model can be used for the further simulations of other loading cases.

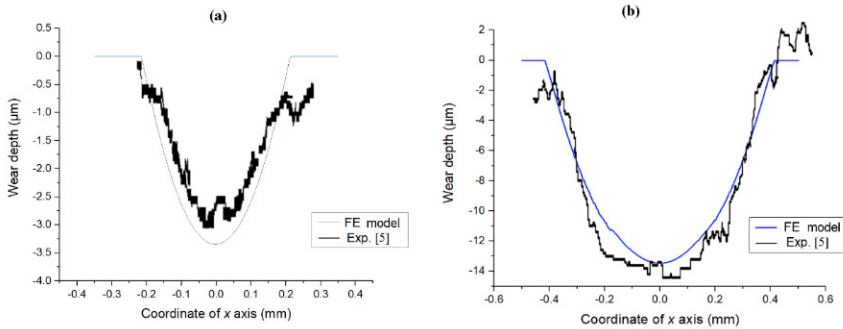


Figure 3-21– Comparison of the FE model wear profile with referenced experimental results after 18000 cycles: (a) P is $185\ \text{N}$ and D is $25\ \mu\text{m}$, (b) P is $1670\ \text{N}$ and D is $25\ \mu\text{m}$ [40]

3.3.2.4 Material property

In this section, the elastic material property model is used in FEM. To validate feasibility of the elastic material property, FE model of elastic perfectly plastic material is compared with that of elastic material. The wear profiles after 30000 cycles for models of both elastic material and elastic perfectly plastic material are shown in Figure 3-22 when P is $1670\ \text{N}$ and D is $25\ \mu\text{m}$. The wear profiles show no difference between two models. This means that the plasticity has no significant effect on the wear profile. The objective of this section is to analyse the wear characteristics. Therefore, to decrease the convergence that may be caused by plasticity, elastic model is applied.

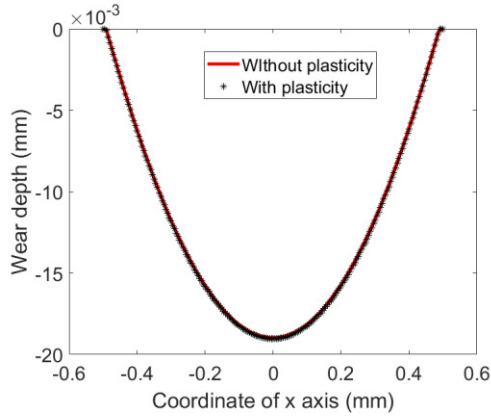


Figure 3-22– Wear profiles after 30000 cycles- P is 1670 N and D is 25 μm

3.3.3 Prediction by POD-RBF

POD-RBF is a strong technique for a model reduction based on Snapshot Matrix, which is collected by FEM, theoretical or experimental data as a first step. The main purpose of this technique is to predict the unknown output parameters from known output parameters. POD-RBF is used to predict the wear characteristics of the specimen under different slip amplitude and normal load in different cycles based on database of the simulation results.

A numerical simulation data of the evolution of wear depth (denoted as W_d) and wear width (denoted as W_w) is used to build Snapshot Matrix U with different applied normal loads F , number of cycles N and displacement amplitude D to build parameters matrix P as presented in the following equations.

$$U = \begin{bmatrix} W_{d1} & W_{d2} & W_{d3} & \cdots & \cdots & \cdots & W_{dn} \\ W_{w1} & W_{w2} & W_{w3} & \cdots & \cdots & \cdots & W_{wn} \end{bmatrix} \quad (3.4)$$

$$P = \begin{bmatrix} D1 & \dots & \dots & Di \\ F1 & F1 & F1 & F1 & F1 & F1 & F2 & F2 & \dots & \dots & Fj \\ N1 & N2 & N3 & N4 & N5 & N6 & N1 & N2 & \dots & \dots & Nk \end{bmatrix} \quad (3.5)$$

Where n is the total number of the loading cases, i is the number of displacement amplitudes, j is the number of normal loads and k is the number of cycles. Normal loads that are used for the simulation are listed as 185 N, 300 N, 500 N, 1000 N and 1670 N. For these normal loads, the number of cycles varies from 5000 to 30000 with interval of 5000 cycles, and the displacement amplitudes varying from 15 μm to 35 μm with interval of 5 μm . Therefore, $i = 5$, $j = 5$, $k = 6$ and $n = 150$, which is obtained by multiplying i , j and k .

C ($C = U \cdot U^T$) is the covariance, λ_i is its eigenvalues and v_i is the eigenvectors. The POD basis Φ is computed by flip the eigenvector matrix.

$$\Phi = \begin{bmatrix} \Phi_1^1 & \Phi_1^2 \\ \Phi_2^1 & \Phi_2^2 \end{bmatrix} \quad (3.6)$$

$$\hat{A} = \hat{\phi}^T \cdot U \quad (3.7)$$

Where, $\hat{\phi}$ is obtained by truncating the matrix φ .

$$\hat{\phi} = \begin{bmatrix} \Phi_1^1 \\ \Phi_2^1 \end{bmatrix} \quad (3.8)$$

$$\hat{A} = [\hat{A}_1 \hat{A}_2 \hat{A}_3 \dots \dots \dots \hat{A}_n] \quad (3.9)$$

The new snapshot matrix can be presented in the following equation:

$$U_{New} \approx \hat{\Phi} \cdot \hat{A} \approx U \quad (3.10)$$

The interpolation RBF and computing G are:

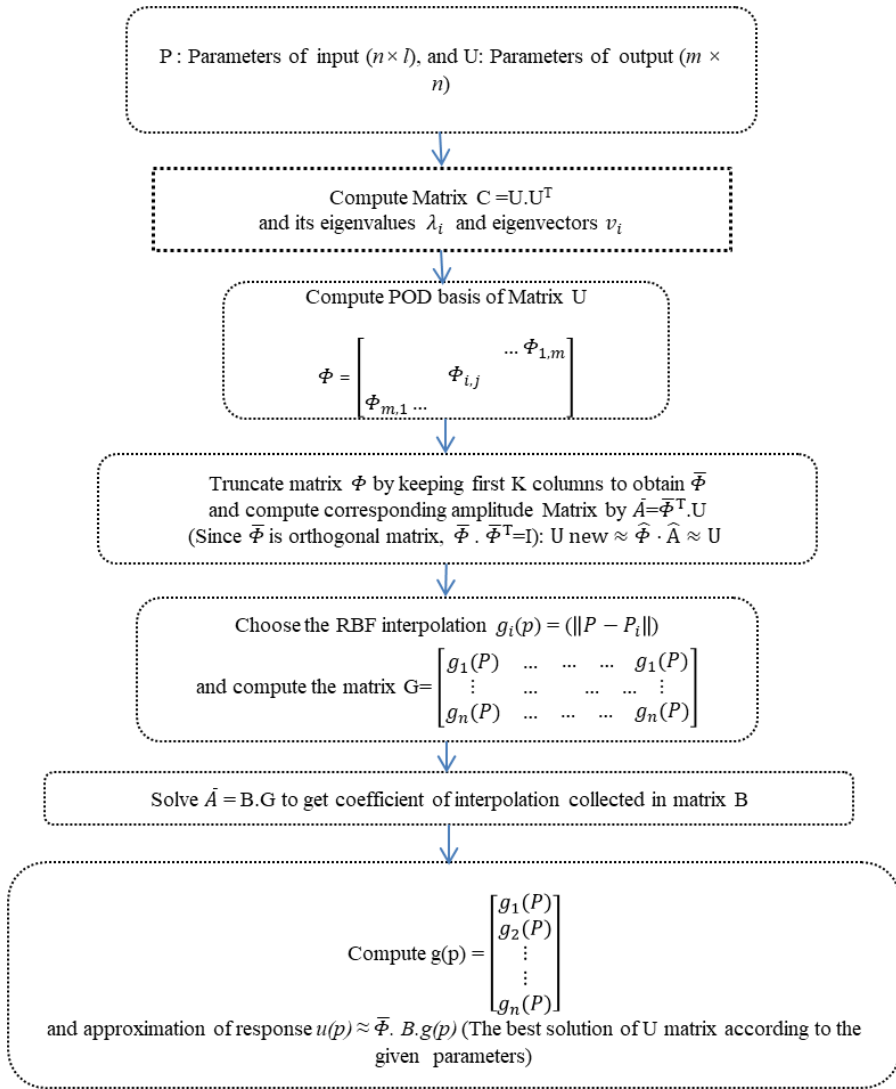


Figure 3-23– Flowchart of POD RBF applied to the wear characteristics prediction

$$G = \begin{bmatrix} g_1(p) & \dots & g_1(p) \\ \vdots & \ddots & \vdots \\ g_n(p) & \dots & g_n(p) \end{bmatrix} \quad (3.11)$$

$$a(p) \approx B \cdot g(p) \quad (3.12)$$

Where $B = A \cdot G^{-1}$

$$g(p) = \begin{bmatrix} g_1(p) \\ g_2(p) \\ \vdots \\ g_n(p) \end{bmatrix} \quad (3.13)$$

The approximation to calculate the friction and wear rate is presented in the following equation:

$$u(p) \approx \Phi \cdot a(p) \quad (3.14)$$

For more details, the procedure of the proposed application is shown in Figure 3-23.

3.4 Combined fretting wear and fretting fatigue models

3.4.1 Experimental set-up

The schematic of the experimental set-up is shown in Figure 3-24 [2]. The normal load, P is applied on the top of cylinders from both sides, after which the tangential load, Q is applied on the right-hand side of the cylinders. Moreover, the cyclic axial stress, σ_A is applied on the right-hand side of the specimen. The tangential stress ratio and the axial stress ratio are all equal to 1. Experimental data for fretting fatigue test is shown in Table 3-4 [2].

The material of both specimen and cylinders is Aluminum 2024-T351. The Young’s modulus, E and Poisson’s ratio, ν are 74.1 GPa and 0.33, respectively. The shear modulus, G , is 28 GPa, and other material parameters are summarised in Table 3-5, in which the first 5 columns are in unit MPa. [164, 165].

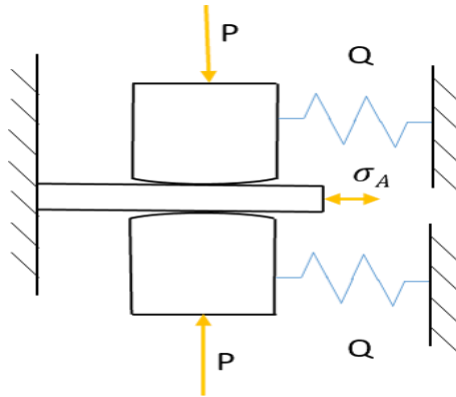


Figure 3-24– Schematic of the experimental set-up

Table 3-4– Experimental data for fretting fatigue test [2]

Experiment Number	P (N)	Q (N)	σ_A (MPa)	N_{exp}^i cycles
1	7085	1487.8	85.2	684658
2	6176	1667.5	84.7	555830
3	6460	2196.4	106.4	195200
4	5319	1914.8	97.4	418911
5	5310	2017.8	85.8	519963
6	6268	1692.4	100	312062

Table 3-5– Constant of material properties [164, 165]

σ'_f	σ_{f-1}	τ_{f-1}	σ_u	σ_y	τ'_f	γ'_f	ϵ'_f	b	c
741	140	80.8	425	310	412.2	0.287	0.166	-0.078	-0.538

The minimum dissipated energy wear coefficient, K_E in sliding condition for pin-on-disc configuration is $3.7 \times 10^{-8} \text{ MPa}^{-1}$ [166]. In partial slip regime, the wear coefficient should be lower. This is because in the contact centre there is a stick zone that supports the partial normal load, where there is no slip to cause wear on the contact surface. Considering this situation, $1.4 \times 10^{-8} \text{ MPa}^{-1}$ is used for the wear coefficient for 2024-T351 in partial slip regime.

3.4.2 FE model

The non-linear FE model is designed in the commercial software ABAQUS by python scripts, which is shown in Figure 3-25. 4-node bilinear plane strain quadrilateral (CPE4) element is applied to the whole model. The radius of the cylinder is 178.0 mm. The heights of cylinder and specimen are 25.0 mm and 6.35 mm, and the lengths of cylinder and specimen are 25.0 mm and 40.0 mm, respectively. The thickness is 12.7 mm for both cylinder and flat. To consider both efficiency and accuracy of the model, the partition is used for both parts. The mesh in both contact zones is magnified in Figure 3-25 and the mesh size on the contact surface is $10 \mu\text{m}$. Multi Point Constraint (MPC) is applied on the top of the cylinder. The flat is set as the slave surface, while the cylinder is set as the master surface. Finite sliding formulation and surface to surface discretization method are used for the contact surfaces. Moreover, the adjustment algorithm is used for the slave surface.

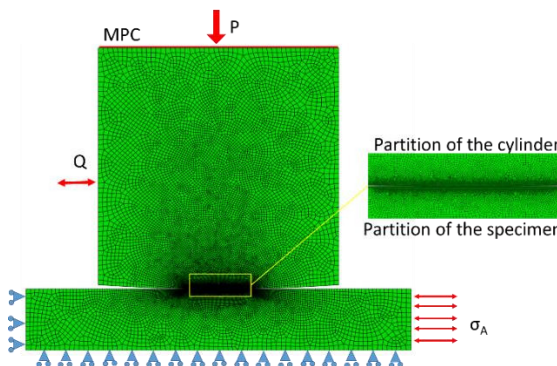


Figure 3-25– FE model 1 for the fretting fatigue experiment

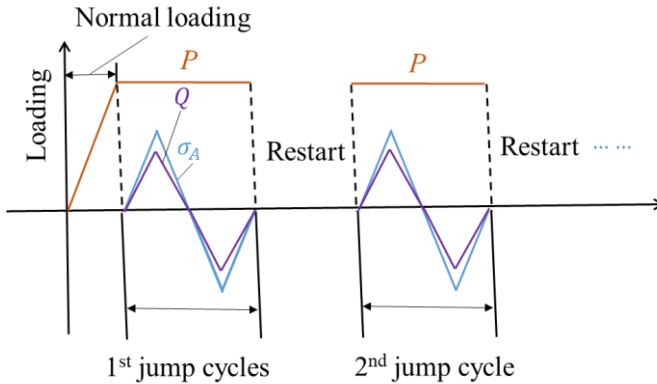


Figure 3-26– Loading history for the fretting fatigue experiment

To make the simulation more efficient, jump cycles, $\Delta N = 5000$ is used in the user subroutine UMESHMOTION. When one cycle is simulated in FE model, the local wear depth will be obtained by multiplying ΔN . The loading condition history in FE model is shown in Figure 3-26. At the end of the first cycle, the model is submitted for the analysis. The second model is established at the end of the first cycle by restating through python code and then it is submitted for the analysis after applying the oscillatory tangential and axial loads. In the following cycles, the process of the loading is the same.

3.4.3 Verification and numerical implementation

3.4.3.1 Verification by Hertzian contact

The shear distribution in partial slip regime is used to verify the FE model, the equation is given by Eq. (2.9). From Figure 3-27, we can see that the FE result of the shear stress shows a good agreement with the analytical one.

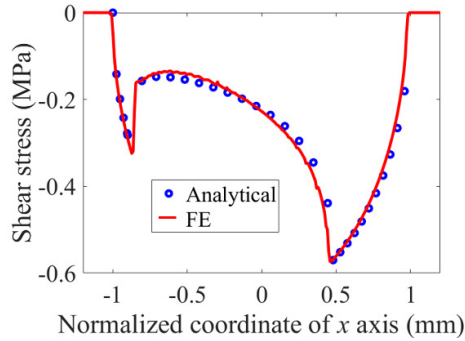


Figure 3-27– Verification of the FE model by the analytical solution

3.4.4 Models with different boundary conditions

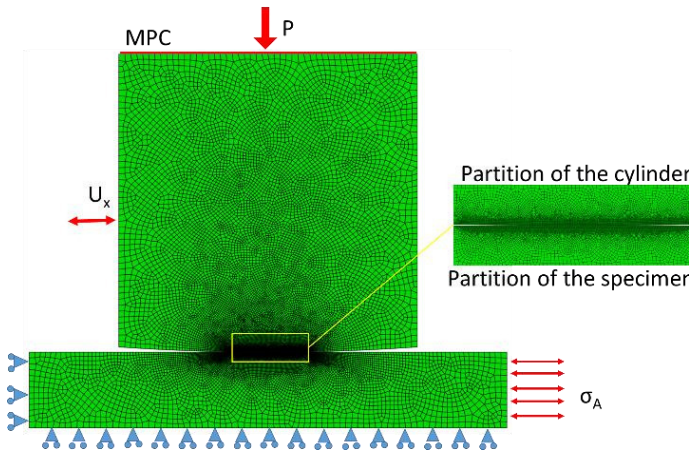


Figure 3-28– FE model 2 for the fretting fatigue experiment

In some experiments, two parameters are given to for the tangential loading: tangential load and tangential displacement. In Ref. [86], the boundary effect is analysed without considering the effect of the wear and it is found that the boundary condition effect on the stress condition is not significant. In this section, the effect of the boundary condition on stress condition is analysed. Based on Exp. 3, the corresponding displacement of the left side of the cylinder can be obtained in model 1 without considering wear. Then the

corresponding oscillatory displacement will be applied to the left side of the cylinder in model 2 considering the effect of wear as shown in Figure 3-28. And then, the stress condition and wear profile in model 2 will be compared with that in model 1 considering the effect of wear.

3.4.5 Loading cases for wear profile analysis

Table 3-6– The loading cases to analyse the effect of loading condition on wear characteristics

Nr.	P (N)	Q (N)	σ_A (MPa)
1	4460	2196.4	106.4
2	6460	2196.4	106.4
3	8460	2196.4	106.4
4	6460	1196.4	106.4
5	6460	3196.4	106.4
6	6460	2196.4	66.4
7	6460	2196.4	146.4

Because the geometry change is the key effect on the variation of stresses and damage parameters, it is very important to analyse the details of the wear characteristics, related to stresses, and damage parameters. Based on the loading conditions of Exp. 3, the effect of the normal load, tangential load, axial load, and non-proportional loading is analysed. Loading cases that are used to analyse the loading condition effect on the wear characteristics are listed in Table 3-6. Experiments 1, 2 and 3 are used to consider the normal load effect, experiments 4, 2, and 5 are used to analyse the effect of the tangential load effect, and experiments 6, 2, and 7 are used to analyse the axial load.

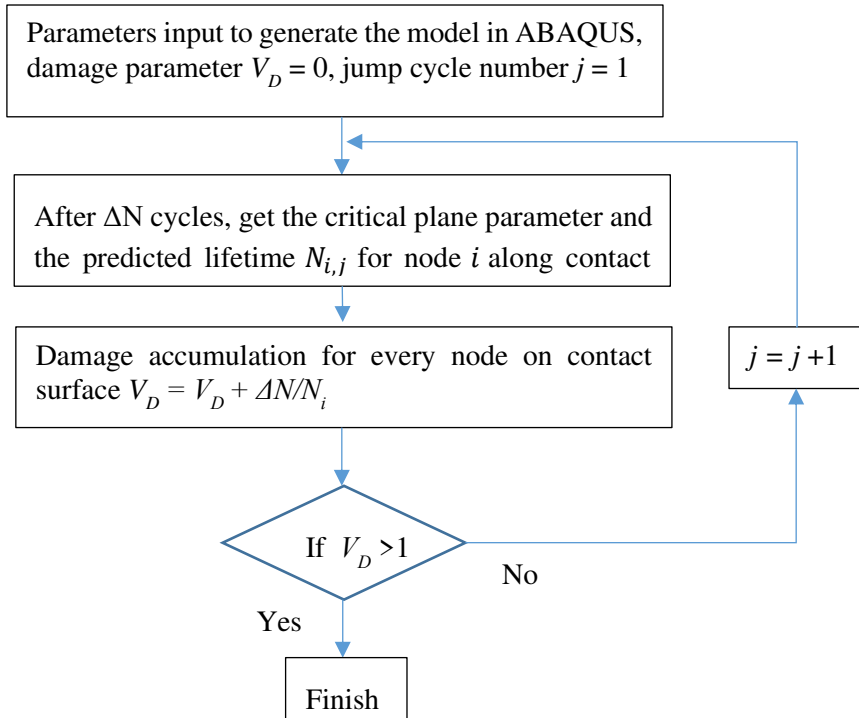


Figure 3-29– Flowchart for the implementation of the prediction of crack initiation lifetime

As shown in Figure 3-29, the wear profile updates and the critical plane parameters are obtained after each cycle. Thereafter, the crack initiation lifetime is calculated, and the damage accumulation parameter is derived from by Miner's rule. The cycle stops when damage parameter on a contact node is greater than 1. The critical plane parameters in some certain cycles are compared and the maximum values of these parameters are considered as where the crack will initiate in the corresponding cycle. Then, the crack initiation location in certain cycle is compared using three critical plane methods. In critical plane methods, the critical plane angle is assumed to be the direction of the crack initiation. Due to the wear effect, Ruiz 2 parameter

is also used for comparison of the crack initiation location with the critical plane methods. Though, Ruiz 1 parameter cannot be used as a standard to determine the crack initiation location, it is proportional to the wear volume. The Ruiz 1 parameter is used to investigate the wear distribution in certain cycles. Exp. 1 is used as an example to analyse the evolution of these parameters.

3.4.6 Fretting fatigue model with debris layer

In the referenced experiments, the wear debris lies near the trailing contact edge as shown in Figure 3-30 [2]. To model the effect of the debris in the FE model of fretting fatigue, the debris layer model concept is considered [70]. The schematic of the debris layer in fretting fatigue model is shown in Figure 3-31 (b). From the figure, we can see that in the stick zone there is no wear and in partial slip zone of both sides, wear happens. This is because not all the wear debris can be ejected from the partial slip zone. Δh is the distance from the original surface to the debris layer. Because the wear profile evolves with cycles and it is not eligible to consider Δh as a constant. In the initial period, the debris effect can be neglected due to the very small wear depth and wear width. After certain cycles, the effect of the debris cannot be ignored anymore. In this section, we analysed the effect of the debris layer after 100000 cycles based on Exp. 1 as shown in Figure 3-31 (a).

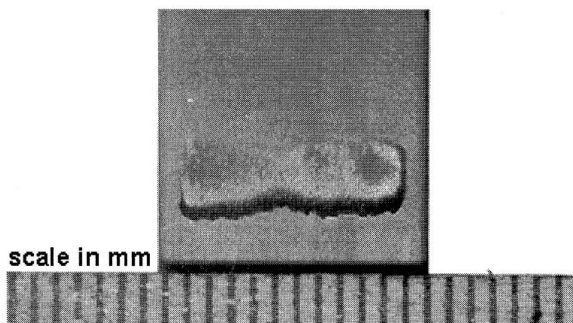


Figure 3-30– Experimental wear profile near the trailing edge

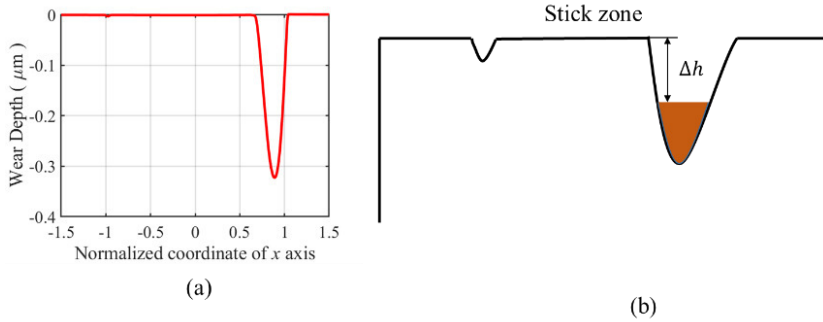


Figure 3-31– Wear profiles: (a) wear profile after 100000 cycle for Exp. 1, and (b) the schematic of the debris layer in fretting fatigue model

After 100000 cycles and releasing the normal load, the debris is introduced as shown in Figure 3-31 (b). Moreover, the wear on the left-hand side can be ignored compared with the wear volume on the right-hand side. If the wear volume is higher in the left-hand side, the debris should also be considered. There are three contacts in FE model: the first one is the contact between the bottom of the cylindrical pad and the upside of the debris, the second one is the contact between the bottom of the cylindrical pad and the upside of the flat specimen and the third one is the bottom of the debris layer and the top of the flat specimen. The bottom of the cylinder is always set as master surface, while the top of the flat specimen is always set as slave surface, which is shown in Figure 3-32. The coefficient of friction is set as 0.65 for the contact between cylinder and the debris, while for the contact between debris and specimen the coefficient of friction is set as 1.0 [70]. The vertical element number is 1 and the horizontal element size is half of the contact element size. Due to the lower amount of wear volume in the first 100000 cycles, the debris is introduced and generated in the model after 100000 cycles. The schematic of the introduction time point of the debris to the model is shown in Figure 3-33. The releasing step is applied at the end of the 100000th cycle by restarting the python code. At the end of the releasing step, then the normal loading, and oscillatory tangential and axial loads are applied consequently after restarting and introducing the debris to the model.

The material properties of the debris layer are the same as the oxide of aluminium. The elastic modulus is 300 GPa and the Poisson’s ratio is 0.21 [167].

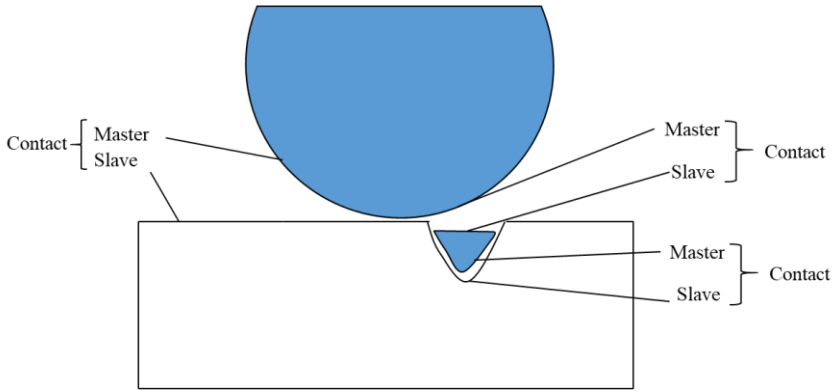


Figure 3-32– Schematic of the contact in FE model

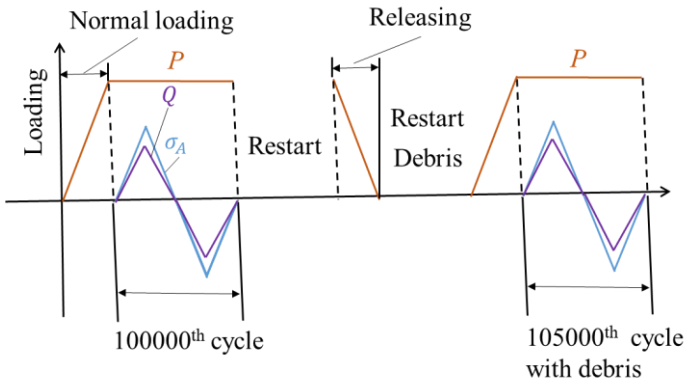


Figure 3-33– Schematic of the introduction time point of the debris to model

3.5 Conclusion remarks

In this chapter, the methodology and numerical models that are used in this paper are presented in detail. Firstly, VWCM and CWCM based on the experimental data are described, in which the TTS period is also considered. Then, prediction tools like POD-RBF, GM, PCF and ANN, and corresponding FE models that are used to generate the database are given. Finally, the model that combines the wear and fretting fatigue both with and without considering the debris layer is described. Moreover, the model considering the effect of fretting fatigue loading is also described. The effect of variable wear coefficient on wear characteristics and the prediction of wear characteristics by POD-RBF, and the effect of the debris on fretting fatigue are given in the following two chapters, respectively.

Chapter 4 Wear characteristics analysis

4.1 Overview

Based on the methodology and FE modelling presented in Section 3.2 and 3.3, the analysis of wear characteristics is given in the following sections. The effect of the variable wear coefficient on the wear characteristics is analysed firstly. In addition, the stress variation with cycles in CWCM is compared with that in VWCM. The result shows that the variable wear coefficient shows a significant effect on the wear characteristics, plasticity accumulation and stress state. Then the prediction tools are applied to predict the wear characteristics under different normal load, oscillatory displacement and cycles by POD-RBF, grey model, PCV, and ANN. The efficiency and accuracy of these methods are compared with each other.

4.2 Effect of variable wear coefficient on wear characteristics

4.2.1 Gross sliding regime

4.2.1.1 Flat specimen

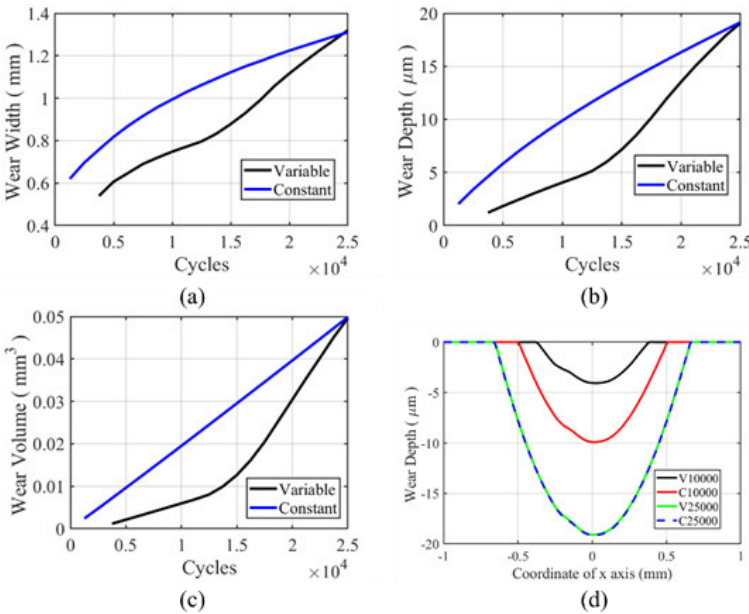


Figure 4-1– History and profile of wear characteristics for the flat specimen in the gross sliding regime for both CWCM and VWCM when $\delta = 50$ mm: (a), (b), and (c) are the history of wear characteristics, and (d) is the wear profiles after 10000th and 25000th cycle

For flat specimen, a moderate-sharp VWCM and CWCM are used. The wear characteristics history can be found in Figure 4-1 (a), (b), and (c). From the figure, we can see that the trend for wear depth, wear width, and wear volume history is the same. In the moderate increment period, the gap between the wear characteristics tends to be greater, while in the sharp increment period, the gap between wear characteristics for VWCM and CWCM tends to be

lower. At the end of the 25000th cycle, there is no significant difference for all the wear characteristics. From Figure 4-1 (d), we can see that in moderate increment period, i.e. 10000th cycle, the wear width and wear depth are both greater in CWCM compared with that in VWCM and at the end of the 25000th cycle, the wear profile of VWCM shows a good agreement with that of CWCM. Moreover, there are some ripples on the left side of the wear profile for both CWCM and VWCM, which is caused by plastic deformation.

From Figure 4-2, we can see that the maximum equivalent plastic strain is located on the left-hand side of the contact centre and the maximum value decreases with the number of cycles. The offset is caused by the initial movement direction of the cylinder. In the initial left movement of the cylinder, the von Mises stress decreases on the contact surface due to the plastic deformation. Therefore, the peak value cannot be reached again when the cylinder moves to the far-right side of contact unless the relative slip amplitude is much greater than the contact zone. This phenomenon is explained in [168, 169]. Another interesting phenomenon is that the plasticity decreases with the number of cycles and the plastic strain on both trailing and leading edges increases with the number of cycles. This phenomenon is caused by the evolution of the wear profile, which removes the residual plastic strain [162]. Moreover, there is a stress concentration on both trailing and leading edges, which causes the plastic deformation. From Figure 4-2 (b), we can see that after an increase of the maximum value of equivalent plastic strain in the TTS period, there is a smooth decrease in the peak value. This means that in the moderate increment period, the equivalent plastic strain decreases smoothly, while in the sharp increment period the equivalent plastic strain decreases dramatically. Due to the increase in the TTS period and the moderate decrease in the moderate increment period, the maximum equivalent plastic strain is always higher in VWCM than that in CWCM.

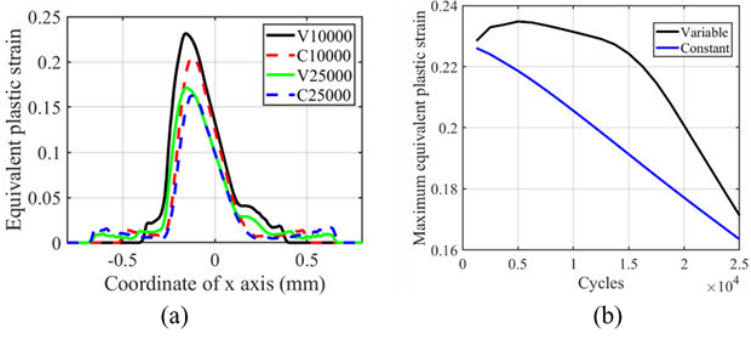


Figure 4-2– Profile and history of equivalent plastic strain for the flat specimen in the gross sliding regime for both CWCM and VWCM when $\delta = 50$ mm: (a) the profiles at 10000th cycle and 250000th cycle, and (b) the maximum value history

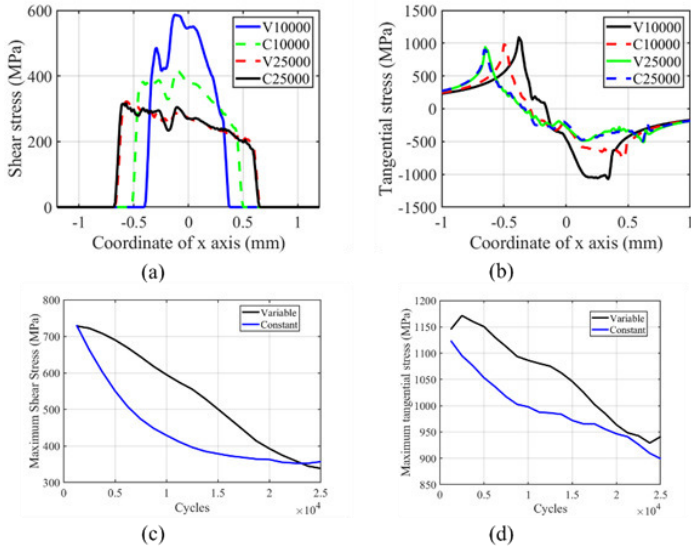


Figure 4-3– Profile and history of shear and tangential stresses for the flat specimen in the gross sliding regime for both CWCM and VWCM: (a) and (b) are shear and tangential stress profiles in 10000th cycle and 250000th cycle when $\delta = 50$ mm, and (c) and (d) are the history of maximum shear and tangential stress, respectively

The shear stress and tangential stress history in the fretting process is shown in Figure 4-3. Both shear and tangential stress are decreasing with number of cycles due to the wear profile evolution. The tangential and shear stress profiles are not smooth on the left-hand side of the contact centre, which is caused by the plastic deformation in this zone. Similar other research results in the literature, the contact zone increases with number of cycles as shown in Figure 4-3 (a) [40]. And due to the lower wear coefficient in the moderate increment period, the contact pressure of VWCM in the 10000th cycle is greater than that of CWCM in the 10000th cycle. From Figure 4-3 (b), we can see that the maximum tangential stress location moves toward the left contact edge with the number of cycles. And in the TTS period, the tangential stress increased with number of cycles, after which it decreases smoothly with the number of cycles. From Figure 4-3 (c) and Figure 4-3 (d), we can see that the tangential and shear stresses are both greater in VWCM than those in CWCM during almost the whole fretting process.

4.2.1.2 Cylindrical pad

For the cylindrical pad, a sharp-moderate VWCM and CWCM are used. The wear characteristics in VWCM, wear width, wear depth, and wear volume are lower in the TTS period and then increase dramatically in the sharp increment period, after which wear characteristics in VWCM exceed that in CWCM at about 5000th cycle. At the end of the 25000th cycle, the wear characteristics of VWCM and CWCM show a good agreement with each other. The ripples on the left-hand side also happens to the cylindrical pad due to the plastic deformation. Based on Figure 4-1 and Figure 4-4, we can see that in the gross slip regime, the variable wear coefficient has no significant effect on the wear characteristics.

The same trend is shown in Figure 4-5 as in Figure 4-2. The peaks of equivalent plastic strain are located on the left-hand side of the contact zone and decrease with number of cycles. The peak value in VWCM is greater than that in CWCM, which is caused by high plastic strain in the TTS period. Based on Figure 4-2 and Figure 4-5, we can conclude that in the gross sliding regime,

there is an increase of equivalent plastic strain in the TTS period and a higher wear coefficient can remove the residual plastic strain faster.

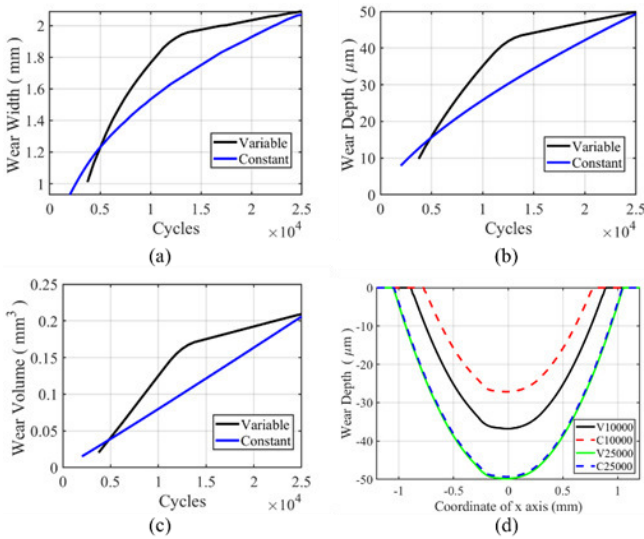


Figure 4-4— History and profile of wear characteristics for the cylindrical pad in the gross sliding regime for both CWCM and VWCM when $\delta = 50$ mm: (a), (b) and (c) are the history of wear characteristics, and (d) is the wear profiles after 10000th and 25000th cycle

The tangential and shear stress profile and maximum value history are shown in Figure 4-6. From Figure 4-6 (c) and (d), we can see that after the TTS period, the maximum value of both tangential and shear stress decreased dramatically in the sharp increment period, after which the maximum value is lower in VWCM than that in CWCM. Moreover, in the moderate increment period, the trend tends to be smooth. The peak values for both stresses tend to be the same for both VWCM and CWCM at the end of the 25000th cycle. From Figure 4-6 (a) and (b), we can see that the position of maximum shear stress is near the maximum equivalent plastic strain point, while the maximum and minimum tangential stresses are located near the contact edge on both sides, respectively. Based on Figure 4-3 and Figure 4-6, we can see that in the gross

sliding regime, the effect of variable wear coefficient on shear and tangential stress is the same as that on the equivalent plastic strain.

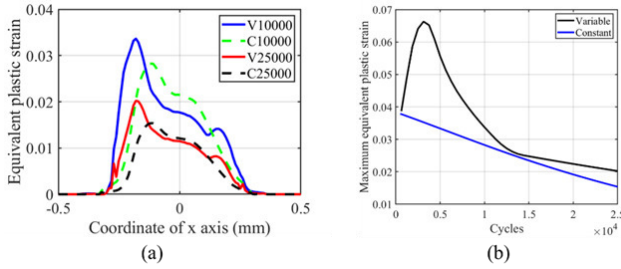


Figure 4-5– Profile and history of the equivalent plastic strain for the cylindrical pad in the gross sliding regime for both CWCM and VWCM when $\delta = 50$ mm: (a) is the profiles in 10000th cycle and 250000th cycle, and (b) is the maximum value history

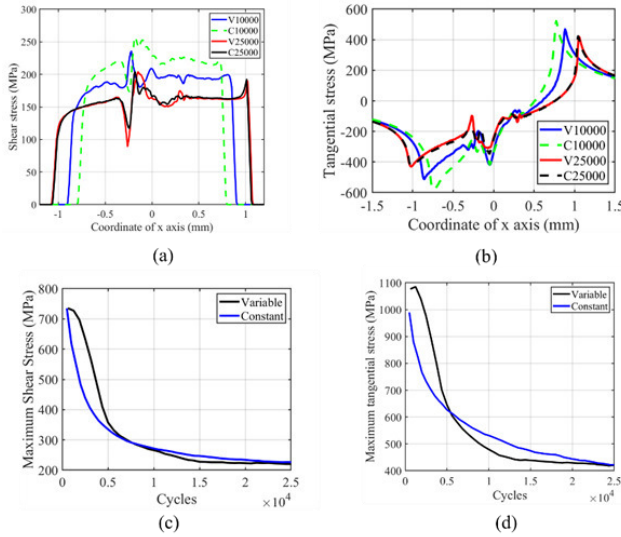


Figure 4-6– Profile and history of shear and tangential stress for the cylindrical pad in the gross sliding regime for both CWCM and VWCM: (a) and (b) are shear and tangential stress profiles in 10000th cycle and 250000th cycle when $\delta = 50$ mm, and (c) and (d) are the history of maximum shear and tangential stress, respectively

4.2.2 Partial slip regime

The wear coefficient in the partial slip regime is assumed to be the same as that in the gross sliding regime. Therefore, the applied displacement $D = 12 \mu\text{m}$ is used to investigate the characteristics history, stress condition in the partial slip regime.

4.2.2.1 Flat specimen

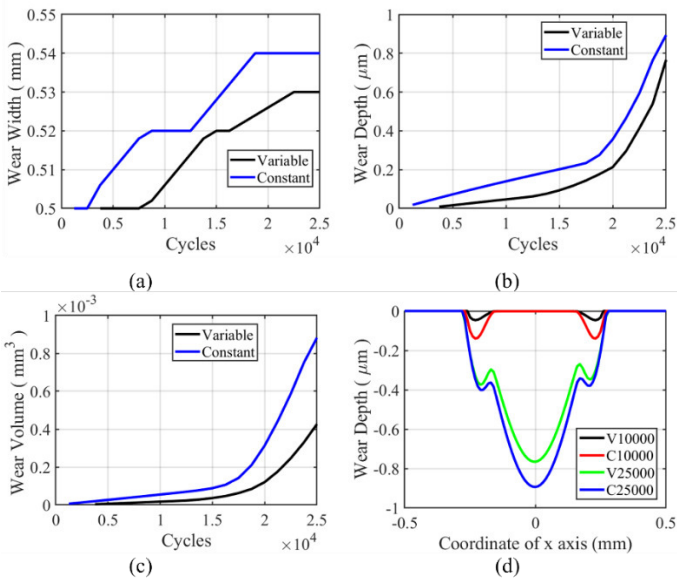


Figure 4-7– History and profile of wear characteristics for the flat specimen in the partial slip regime for both CWCM and VWCM when $\delta = 10 \text{ mm}$: (a), (b), and (c) are the history of wear characteristics, and (d) is the wear profiles after 10000th and 25000th cycle

The wear characteristic for the flat specimen in the partial slip regime is shown in Figure 4-7. From Figure 4-7 (a), we can see that the wear width in VWCM is lower than that in CWCM in the whole process. The line for wear width is not smooth due to the mesh size. For Figure 4-7 (b) and Figure 4-7 (c), we can

see that the wear depth and wear volume in VWCM are also lower than that in CWCM in the whole fretting process. From Figure 4-7 (d), due to the wear in the partial slip zone, the slip happens in the stick zone to accommodate the applied displacement for both VWCM and CWCM. There is a dramatic increase of wear depth and wear volume after the 20000th cycle, due to this phenomenon. Because the shear stress decreases dramatically with cycles as is shown in Figure 4-9 (c), the higher shear stress can cause more wear volume with higher wear coefficient before 15000th cycle and then the time point when the stick zone slips for CWCM is earlier than that for VWCM, after which the wear volume increased dramatically. The transition time point is about 17500th cycle for CWCM, while for VWCM, the transition time point is about 20000th cycle.

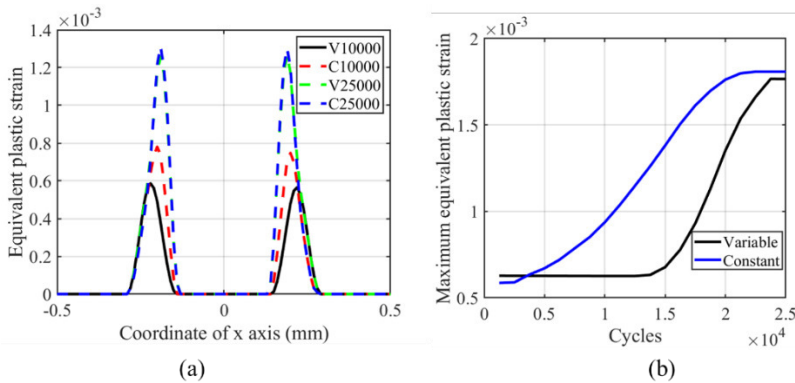


Figure 4-8– Profile and history of equivalent plastic strain for the flat specimen in the partial slip regime for both CWCM and VWCM when $\delta = 10$ mm: (a) is the profiles in 10000th cycle and 25000th cycle, and (b) is the maximum value history

From Figure 4-8, we can see that the accumulation of plasticity increases in partial slip regime with the number of cycles, while in Figure 4-2 the trend is the opposite. This phenomenon is caused by the lower wear effect in partial slip regime on plasticity accumulation. The maximum and profile of plastic strain show no significant difference between VWCM and CWCM. The

maximum plastic strain locates near the initial contact edge. Due to the lower wear coefficient for flat specimen and lower relative slip in partial slip regime, the effect of TTS period on the accumulation of plasticity in VWCM is not significant compared with that in CWCM. At the end of the 25000th cycle, the maximum equivalent strain in CWCM is a little greater than that in VWCM, which is caused by stable plastic accumulation in CWCM. stress concentration in wear process plays a more important role in plastic accumulation compared with wear in partial slip regime.

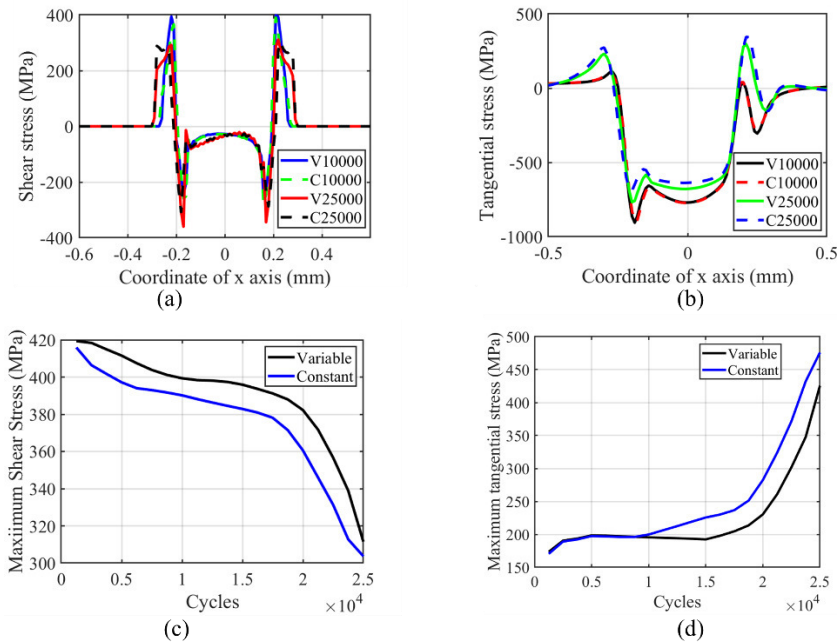


Figure 4-9– Profile and history of shear and tangential stress for the flat specimen in the partial slip regime for both CWCM and VWCM: (a) and (b) are shear and tangential stress profiles in 10000th cycle and 25000th cycle when $\delta = 10$ mm, and (c) and (d) are the history of maximum shear and tangential stress, respectively

The tangential and shear stress profile and maximum value history are shown in Figure 4-9 for flat specimen in partial slip regime. From Figure 4-9 (a) and (b), we can see that the maximum shear stress decreases, while the minimum shear stress increases with the number of cycles. Maximum tangential stress and minimum tangential stress show the opposite trend. Through the history of the maximum shear and tangential stress shown in Figure 4-9 (c) and (d), we can see that the effect of the wear characteristics on the maximum value of tangential and shear stress is the opposite. The maximum tangential stress history shows a similar trend with wear characteristics' history, while maximum shear stress history shows the opposite trend.

4.2.2.2 Cylindrical pad

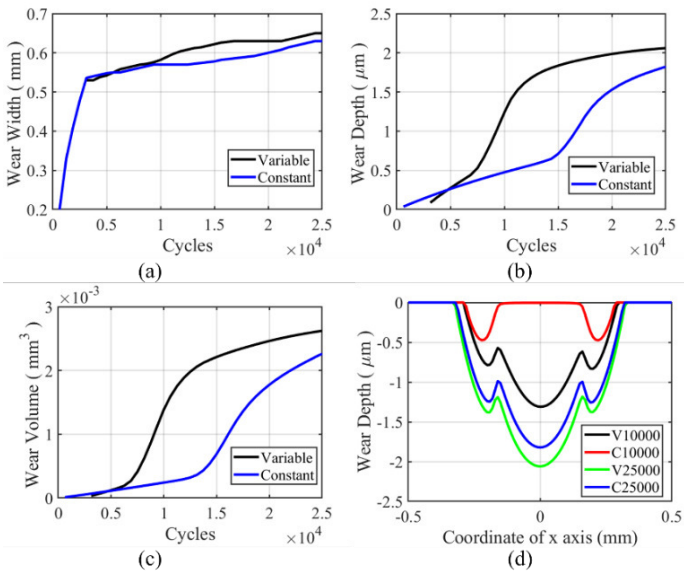


Figure 4-10– History and profile of wear characteristics for the cylindrical pad in the partial slip regime for both CWCM and VWCM when $\delta = 10$ mm: (a), (b), and (c) are the history of wear characteristics, and (d) is the wear profiles after 10000th and 25000th cycle

Wear characteristics for the cylindrical pad in partial slip regime is shown in Figure 4-10. From Figure 4-10 (a), (b), and (c), we can see that after the TTS period, there is a dramatic increment of wear width, wear depth and wear volume in VWCM in the sharp increment period and then smooth increment in moderate increment period. The wear depth and wear volume in VWCM are both higher after about the 6000th cycle than that in CWCM. Though the wear width is almost the same at the 25000th cycle, the wear depth and wear volume are greater in VWCM than that in CWCM. The wear coefficient of the cylindrical pad is much higher than that of the flat specimen. The stick zone begins to slip after about 6000th cycle with a higher wear coefficient and 15000th cycle with a constant wear coefficient respectively, as shown in Figure 4-10 (b) and (c). Therefore, the stick zone begins to slip earlier and with a higher wear coefficient in VWCM than that in CWCM, which causes more wear in the initial stick zone in VWCM with higher shear stress as shown in Figure 4-12 (c) and makes the wear depth, wear width, and width higher in VWCM at the end of the 25000th cycle.

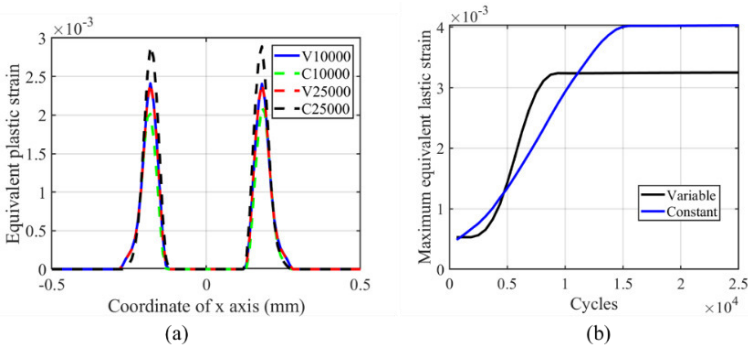


Figure 4-11– Profile and history of the equivalent plastic strain for the cylindrical pad in partial slip regime for both CWCM and VWCM when $\delta = 10$ mm: (a) is the profiles in 10000th cycle and 25000th cycle, and (b) is the maximum value history

From Figure 4-11, the equivalent plastic strain increases with number of cycles for the cylindrical pad in the partial slip regime, which shows the same

trend for the flat specimen in the partial slip regime. The maximum value in CWCM is lower than that in VWCM at the 10000th cycle and is greater than that in VWCM at the 25000th cycle. Moreover, due to more material removal in VWCM, the equivalent plastic strain in CWCM exceeds that in VWCM, as shown in Figure 4-10 (d). The maximum equivalent plastic strain tends to be stable after the slipping of the initial stick zone.

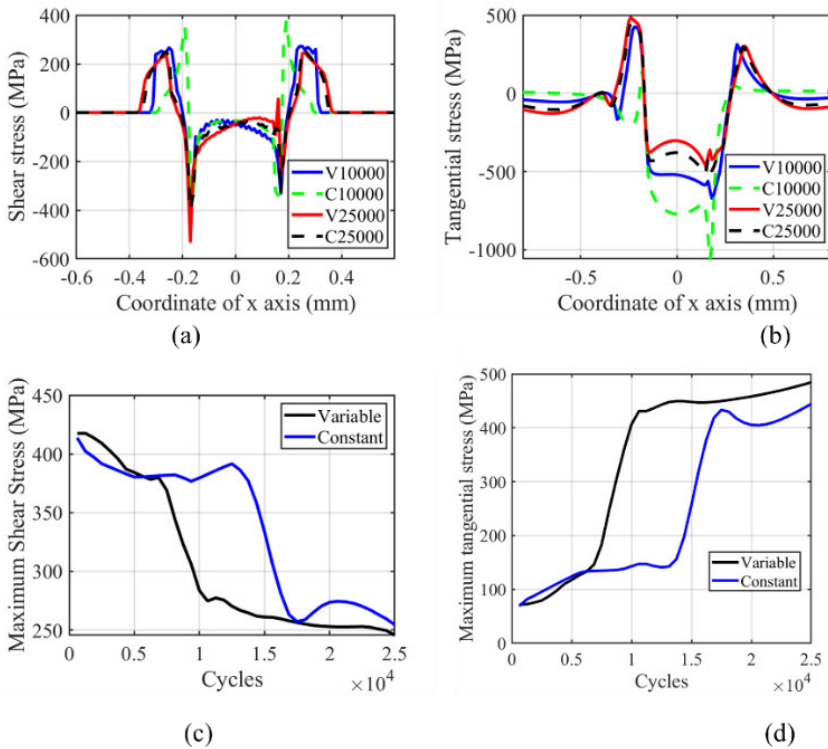


Figure 4-12– Profile and history of shear and tangential stress for cylindrical pad in the partial slip regime for both CWCM and VWCM: (a) and (b) are shear and tangential stress profiles in 10000th cycle and 25000th cycle when $\delta = 10$ mm, and (c) and (d) are the history of maximum shear and tangential stress, respectively

The history and profile of tangential and shear stress are shown in Figure 4-12. From Figure 4-12 (a) and (b), we can see that the maximum tangential and

shear stresses are located near the contact edge and move far away from the contact centre with number of cycles. From Figure 4-12 (c) and (d), we can see that the trend of shear and tangential stresses is opposite with number of cycles. The dramatic decrease of shear stress and increase of tangential stress happen near the cycle in which the initial stick zone begins to slip for both CWCM and VWCM. At the 25000th cycle, the maximum shear stress is lower, and the tangential stress is greater in VWCM than that in CWCM, which shows the same trend as for wear depth and volume in Figure 4-9 (c) and (d).

4.3 Prediction of wear characteristics by POD-RBF

4.3.1 Results of simulated cases

Wear width and wear depth are the main characteristics of wear profile. Three variables are considered as the input for the simulation: normal loads, displacements, and number of cycles. Wear width and wear depth are obtained under different loading cases. Wear depth and wear width variation with cycles and displacements when the normal load is 185 N is taken as an example and the results are presented in Table 4-1 and Table 4-2, respectively. The data in Table 4-1 and Table 4-2 is plotted in Figure 4-13 and Figure 4-14, respectively.

Table 4-1– Wear depth (μm) at different cycles under different amplitudes - normal load 185 N

Displacement (μm)	Number of cycles					
	5000	10000	15000	20000	25000	30000
15	0.9967	1.5933	2.0952	2.5430	2.9561	3.3424
20	1.2078	1.9311	2.5412	3.0877	3.5899	4.0609
25	1.3935	2.2323	2.9403	3.5749	4.1567	4.6926
30	1.5665	2.5152	3.3157	4.0320	4.6930	5.3125
35	1.7274	2.7736	3.6546	4.4469	5.1788	5.8675

Table 4-2– Wear width (μm) at different cycles under different amplitudes - normal load 185 N

Displacement (μm)	Number of cycles					
	5000	10000	15000	20000	25000	30000
15	0.23	0.29	0.33	0.365	0.39	0.415
20	0.26	0.325	0.365	0.405	0.435	0.46
25	0.28	0.35	0.4	0.435	0.47	0.495
30	0.3	0.375	0.43	0.47	0.505	0.535
35	0.32	0.405	0.46	0.505	0.535	0.565

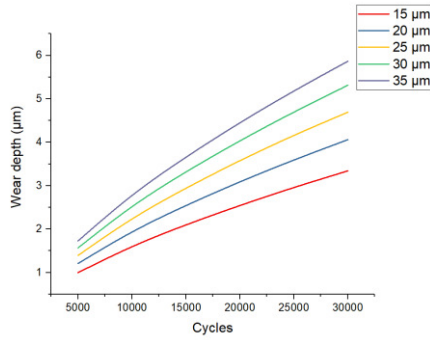


Figure 4-13– Wear depth (μm) versus number of cycles under different amplitudes - normal load 185 N

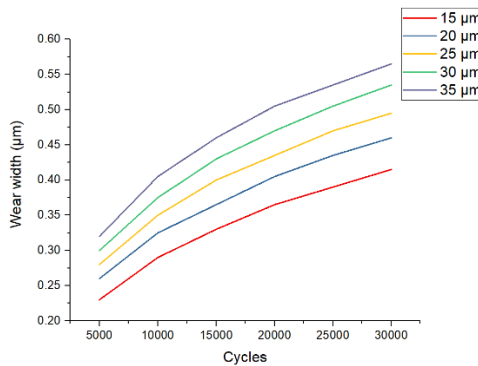


Figure 4-14– Wear width (μm) versus number of cycles under different amplitudes - normal load 185 N

The data of wear depth and wear width under other normal loads, such as 300 N, 500 N, 1000 N and 1670 N, was also obtained, but is not shown in detail. For these normal loads, the number of cycles also varied from 5000 to 30000 where the interval is 5000 cycles and the displacement amplitudes varied from 15 μm to 35 μm where the interval is 5 μm . All above obtained wear characteristics data is organised as database for the prediction.

4.3.2 Prediction of wear profile for different number of cycles

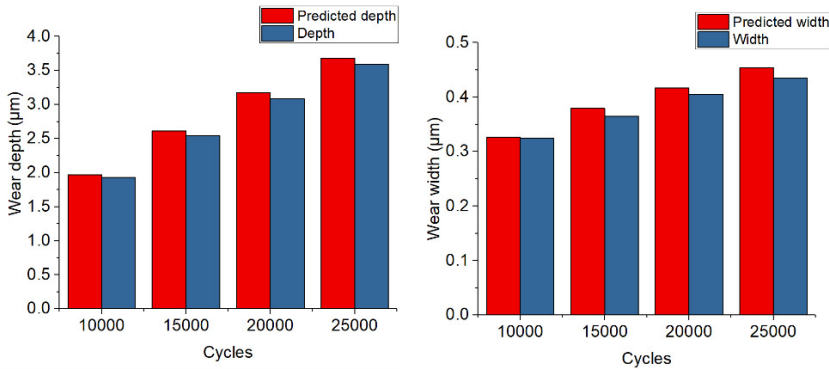


Figure 4-15– Comparison of wear characteristics between simulated data and predicted values by POD-RBF for normal load 185 N and displacement amplitude 20 μm

POD-RBF is commonly used to predict the results between the maximum and minimum input values. For example, wear characteristics can only be predicted between minimum cycle 5000 and maximum cycle 30000 based on the database. The predicted values of wear characteristics under normal load 185 N when the displacement amplitude is 20 μm between 10000 cycle and 25000 cycles, as shown in Figure 4-15. The prediction error is shown in Figure 4-16. It can be concluded that all the prediction error is lower than 5% and the prediction result is very good.

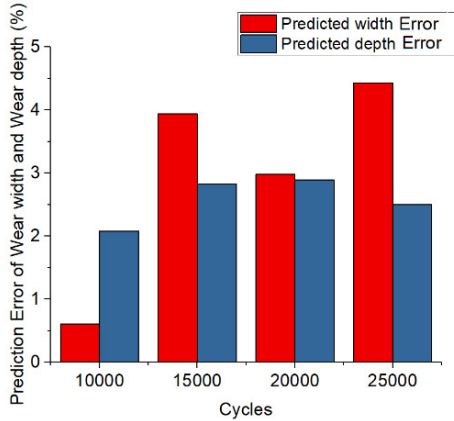


Figure 4-16– Corresponding prediction error of POD-RBF of the data in Figure 4-15

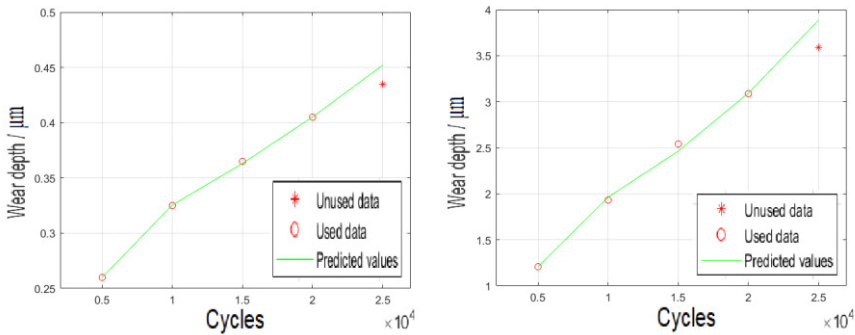


Figure 4-17– Wear characteristics prediction by GM (1, 1)

GM (1, 1) is commonly used for data prediction at the same intervals. The wear characteristics changes with cycles, in which the cycles increment is the same, and the minimum number of raw data is 4. Therefore, GM (1, 1) can be used here. The wear characteristics are predicted when the normal load is 185 N and displacement amplitude is 20 μm at 25000th cycle based on the data

from 5000 cycle to 20000 cycles, as shown in Figure 4-17. From the figure, we can see that there is an error between the predicted value and the raw data, which is the distance between the predicted values and unused data. Used data means that the predicted values are obtained based on these data. The corresponding errors of wear width and wear depth at 25000th cycle are 3.9% and 8.2%, respectively, which are higher than that obtained by POD-RBF. There are also limitations to this approach, for example, there should be the same variable intervals between the raw data and the data to be predicted. And it can only be used for further prediction and interpolation is not available.

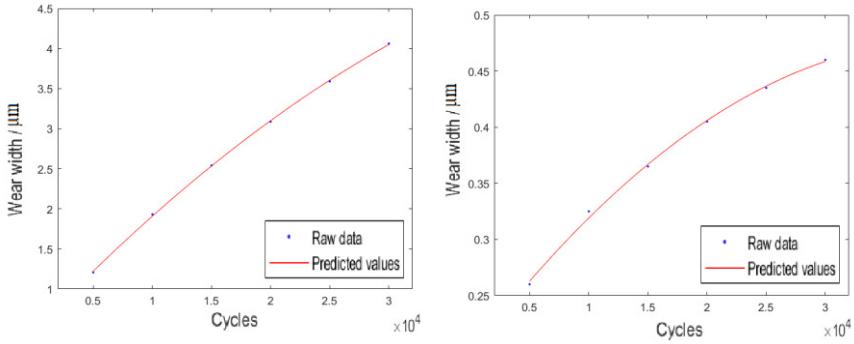


Figure 4-18– Wear characteristics prediction by PCF

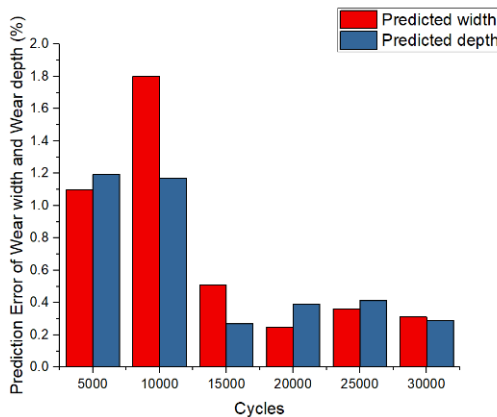


Figure 4-19– Corresponding prediction error of PCF of the data in Figure 4-18

Wear characteristics predicted by PCF of second order and its corresponding error are shown in Figure 4-18 and Figure 4-19, respectively. From the figure, it can be concluded that the predicted values are in good agreement with the raw data and the prediction error is lower than that obtained by POD-RBF.

The CPU time of FE model for each loading cases is 2.5 h, which is much higher than that of prediction methods. Therefore, prediction methods are alternative for the prediction of the wear characteristics. The CPU time of these three methods to predict the correct values is compared in Table 4-3. Obviously, the efficiency of POD-RBF is much greater than the other two methods. GM method's computation time is the greatest among all three methods due to the mean generation operation and n Accumulated Generating Operation in the computing process.

Table 4-3– CPU time of methods for parameters prediction

Methods	GM (1, 1)	PCF	POD-RBF
CPU time / s	1.189	0.485	0.186

4.3.3 Prediction of wear profile for three different parameters

Though the accuracy of POD-RBF is not greater than PCF, the efficiency is greater than the other two methods. There is also another main advantage for POD-RBF, i.e. it can predict the wear characteristics under different displacement amplitude, number of cycles and normal loads. For example, when the normal load is between 185 N and 1670 N, displacement amplitude is between 15 μm and 35 μm , and a few cycles between 5000 and 30000, wear characteristics can all be predicted based on the matrix U and P by POD-RBF. To validate this, five load points are selected randomly and used to predict the wear characteristics, after which the prediction results are compared with the simulation results obtained by FEM.

To obtain the random load cases, Matlab code is used to generate random data of normal load, displacement amplitude and a few cycles, denoted as RN , RD , and RF , respectively. Three randomly generated matrixes are shown as:

$$RN = [19000, 8000, 5000, 29000, 7000]$$

$$RD = [31, 26, 23, 17, 20] \quad (4.1)$$

$$RF = [818, 1370, 1320, 384, 753]$$

The randomly generated load input matrix, LI is generated as:

$$LI = \begin{bmatrix} RD(1) & RD(2) & RD(3) & RD(4) & RD(5) \\ RF(1) & RF(2) & RF(3) & RF(4) & RF(5) \\ RN(1) & RN(2) & RN(3) & RN(4) & RN(5) \end{bmatrix} \quad (4.2)$$

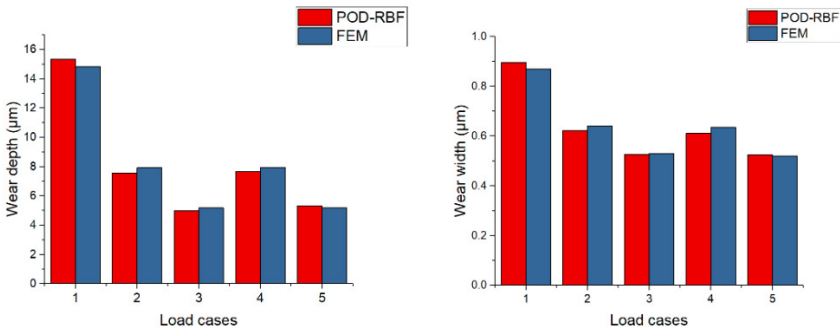


Figure 4-20– Comparison of wear characteristics obtained by FEM and POD-RBF under random generated load cases

Where one column of LI represents one input load case. And every load case in LI is used as the input to obtain the wear characteristics by FEM and POD-RBF. The raw data obtained by FEM and prediction data obtained by POD-RBF under 5 load cases of LI are shown in Figure 4-20. To quantify the

prediction accuracy of wear characteristics by POD-RBF, its prediction errors are shown in Figure 4-21 compared with the FEM raw data under randomly generated load cases. Based on Figure 4-20 and Figure 4-21, it can be concluded that the POD-RBF can be used as prediction tool for wear characteristics under different loading cases based on the raw data. This is because the prediction error is within 5% for all the random generated loading cases.

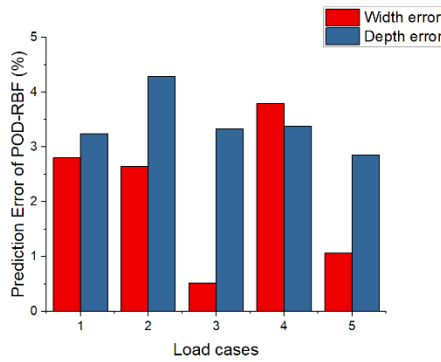


Figure 4-21– Prediction error by POD-RBF compared with the FEM raw data under random generated load cases

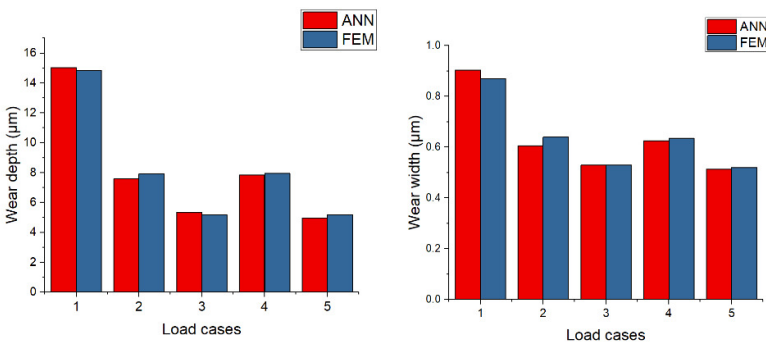


Figure 4-22– Comparison of wear characteristics obtained by FEM and ANN under random generated load cases

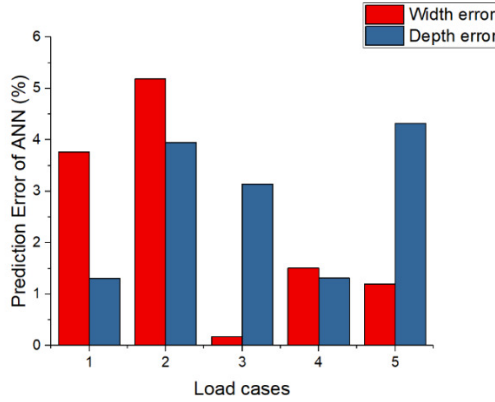


Figure 4-23– Prediction error by ANN compared with the FEM raw data under random generated load cases

Matrix U and P are used as the training input and output data of ANN, respectively. For the common database, two hidden layers are enough [170]. Therefore, two hidden layers are applied. Testing, validation, and training ratios are set as 15/100, 15/100 and 70/100, respectively, which are mostly used in ANN. The prediction results of wear characteristics by ANN compared with FEM results are shown in Figure 4-22. And the corresponding prediction errors are shown in Figure 4-23. ANN can predict the wear characteristics with good accuracy, but compared with POD-RBF, the maximum prediction error of ANN is little higher than 5%. Except one maximum error of ANN, the accuracy of POD-RBF and ANN are all higher than 95% and can be used for the prediction.

Table 4-4– CPU time of methods for 3 parameter prediction

Methods	ANN	POD-RBF
CPU time / s	4.656	1.210

Besides the accuracy, the computational efficiency is also compared between POD-RBF and ANN, as shown in Table 4-4. Due to the data training before prediction in ANN, the CPU time of ANN is much higher than that of POD-RBF.

4.4 Conclusion remarks

In gross sliding regime, the characteristics of the wear profile has an opposite effect on the maximum tangential and shear stress for both flat specimen and cylindrical specimen. Lower maximum stress corresponds to the higher wear characteristics. The effect of wear volume on the plasticity accumulation is significant. The higher wear volume caused less plasticity accumulation. The effect of VWCM for flat and cylindrical specimen on the history of stress, wear characteristics and plasticity accumulation are significant.

In partial slip regime, the characteristics of the wear profile has an opposite effect on the maximum shear stress and positive effect on the tangential stress for both flat specimen and cylindrical specimen. Lower maximum shear stress and higher maximum tangential stress corresponds to the higher wear characteristics. The effect of wear volume on the plasticity accumulation is not significant. Plasticity accumulation in CWCM tends to be higher than that in VCWM for both specimen and cylinder. The effect of VWCM for flat and cylindrical specimen on the history of stress, wear characteristics and plasticity accumulation are significant.

The history of stress and strain in VWCM differs from that in CWCM. Stress and strain history can affect the crack initiation lifetime. Therefore, the effect of VWCM on crack initiation can be future investigated.

A predictive tool for fretting wear characteristics, i.e. wear width and wear depth, namely POD-RBF, is proposed. FEM method is commonly used to predict the wear characteristics. However, it is time-consuming, especially when different parameters such as slip amplitude, number of cycles and normal loads, would be considered. For example, for every load case, a new FE model should be solved. Through POD-RBF, wear characteristics can be predicted within 1 second based on the database for some cases, obtained by FEM. To validate the accuracy, efficiency, and applicability of POD-RBF, it is compared with the GM (1, 1) and PCF of second order when the load and oscillatory displacement are given. The results show that the accuracy of

POD-RBF is greater than 95% and the efficiency is the highest among the three considered prediction methods. To further investigate the applicability of POD-RBF for any combination of displacement amplitude, number of cycles and normal load, five random load cases are applied. Based on the database, the accuracy of wear characteristics prediction under randomly generated load cases is higher than 95% by POD-RBF. Compared with ANN, POD-RBF shows higher computational efficiency and accuracy. This prediction tool can be used to predict fretting wear characteristics properly.

Chapter 5 Effect of wear on fretting fatigue

5.1 Overview

Wear and fatigue both happen in fretting condition, and they interact with one another during the whole process. Fretting fatigue is commonly analysed without considering the effect of wear in partial slip regime, though the fact is that wear affects the lifetime of crack initiation. This thesis investigates, for the first time, the effect of wear debris on fretting fatigue crack initiation. To investigate the effect of debris, fretting wear characteristics in partial slip regime is analysed for loading conditions firstly. Then, the effect of wear on fretting fatigue crack initiation is investigated using Ruiz parameters and critical plane approach without considering the debris effect. Through the results, we see that loading conditions affect the wear profiles in different ways. Moreover, wear has a significant effect on the fatigue in partial slip regime without considering debris especially on the crack initiation location.

Finally, the effect of the wear debris on critical plane parameters are analysed and found that by considering the effect of the debris, the fretting fatigue crack initiation location is shifted towards the trailing edge. The predictions of both crack initiation location and lifetime show a good agreement with the experimental data.

5.2 Effect of boundary condition on the FE results

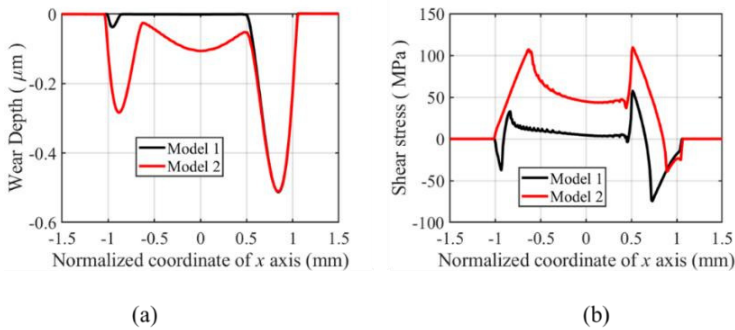


Figure 5-1– Effect of boundary conditions on the wear profile and shear stress: (a) wear profiles after 80000 cycles and releasing step, and (b) shear stress at the end of 80000th cycle.

Using different boundary conditions, the wear profiles show a difference after 80000 cycles as shown in Figure 5-1 (a). The wear depth in the right-hand slip zone is almost the same, while in the left-hand slip zone, the wear depth of model 2 tend to be greater than that of model 1. Moreover, in the stick zone, there is no slip happens in model 1, while in model 2, the wear is significant in the initial stick zone. By comparing the shear stress in Figure 5-1 (b), we can see that in model 2, the shear stress is higher than that in model 1, which means that the boundary conditions influence the shear stress distribution when considering the wear in fretting fatigue. Therefore, higher shear stress

in model 2 can lead to more wear in fretting process. Maximum shear stresses are found near the boundary of slip and stick zone in both models.

The applied tangential force can lead to a tangential displacement in fretting fatigue, and the applied tangential displacement can also lead to a tangential force for the contact parts. When there is no wear, the applied tangential displacement can lead to the corresponding tangential force. The profile of the shear stress obtained by applying tangential force is the same as that obtained by applying corresponding tangential displacement when the wear is not considered. This phenomenon is verified in Ref. [116]. When considering wear in fretting fatigue, the tangential force will lead to a different tangential displacement compared with that without considering wear. This is caused by the wear profile. In the experiments, there are also two kinds of tangential loads, tangential force, and tangential displacement. The same tangential force could cause different tangential displacements in fretting process. There are many experimental fretting loops that show the history of the tangential force and displacement relationship, which is not a constant all the time [171]. Therefore, if a tangential displacement obtained in tangential force model without considering wear is applied to the FE model considering wear, the corresponding tangential force for the contact parts will differ from that without considering wear. This caused the difference of the profile of the shear stress and wear for model 1 and model 2. The reason for the wear in stick zone for constant tangential displacement model when considering the wear is that the elastic deformation can no longer accommodate the relative displacement due to the applied constant tangential displacement. This is the effect of the boundary conditions on the wear profile.

5.3 Effect of loading cases and phase difference on wear profiles

From Figure 5-2 (a), we can see that the normal load can broaden the contact zone and higher normal load can make the wear width greater. Moreover,

lower wear depth was found with higher normal load, which is caused by lower slip amplitude. This is because with the same tangential load there will be a small slip zone under higher normal load. Figure 5-2 (b) shows that the higher tangential load can cause greater wear depth due to the higher slip amplitude and the location of the maximum wear depth is the same for all three loading cases for both left-hand and right-hand sides. In Figure 5-2 (c), we can see that the higher axial load can cause greater maximum wear depth on the right-hand side, and lower maximum wear depth on the left-hand side. It means that the higher axial load can cause a greater slip amplitude on the right-hand side, and lower slip amplitude on the left-hand side. Because the normal load is the same, the position of the maximum wear depth is the same with different axial and tangential loads.

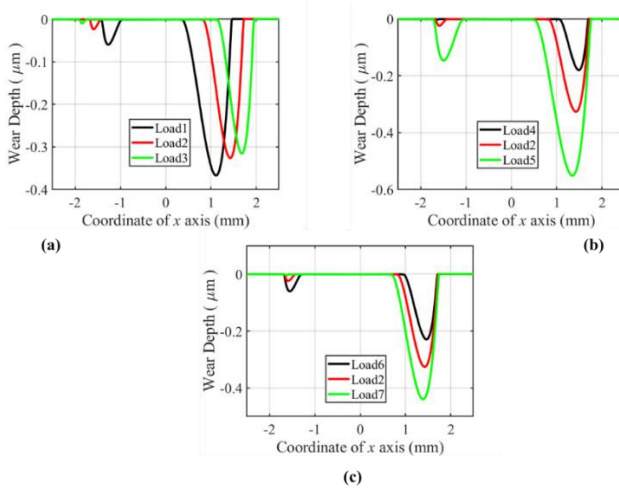


Figure 5-2– Effect of loading cases on wear profiles: (a) effect of normal load, (b) effect of tangential load, and (c) effect of axial load

5.4 Effect of wear on fatigue initiation position

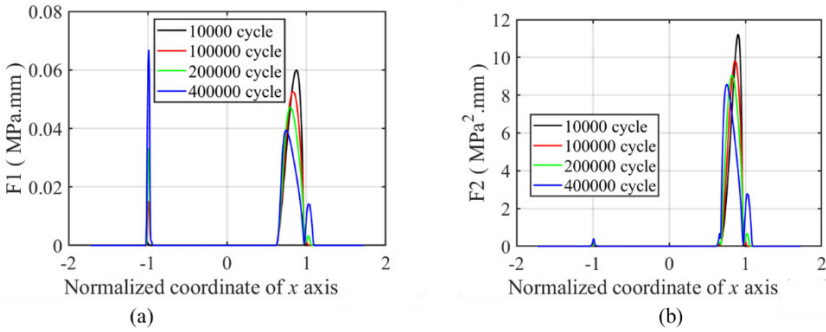


Figure 5-3– Variation of Ruiz parameters with cycles for Exp. 1 when σ_A reaches the maximum value

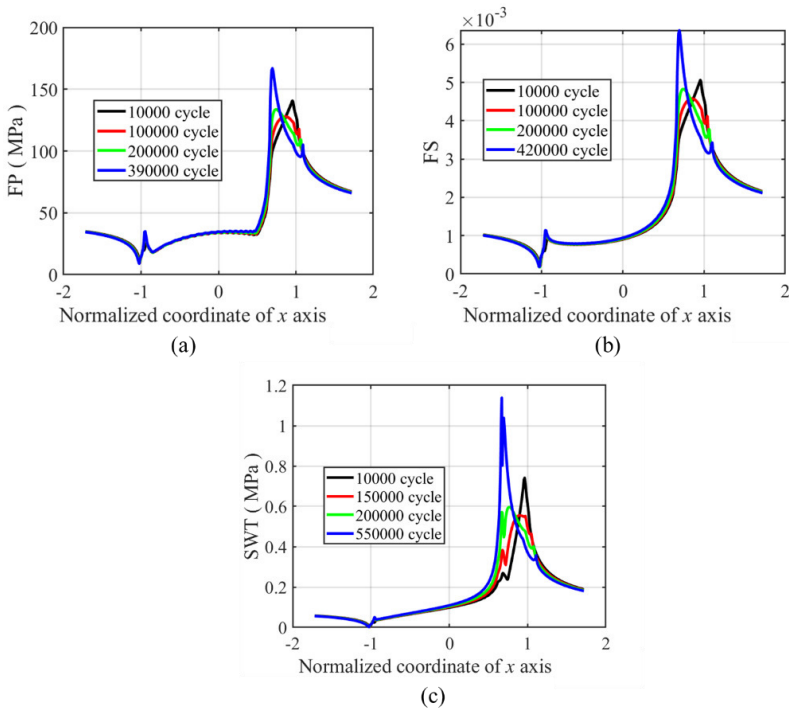


Figure 5-4– Variation of critical plane parameters with cycles for Exp. 1

From Figure 5-3 (a), we can see that the normal load can broaden the contact zone and higher normal load can make the wear width greater. Moreover, lower wear depth was found with higher normal load, which is caused by lower slip amplitude. This is because with the same tangential load there will be a small slip zone under higher normal load. Figure 5-3 (b) shows that the higher tangential load can cause greater wear depth due to the higher slip amplitude and the location of the maximum wear depth is the same for all three loading cases for both left-hand and right-hand sides. In Figure 5-3 (c), we can see that the higher axial load can cause greater maximum wear depth on the right-handed side, and lower maximum wear depth on the left-hand side. It means that the higher axial load can cause a greater slip amplitude on the right-hand side, and lower slip amplitude on the left-hand side. Because the normal load is the same, the position of the maximum wear depth is the same with different axial and tangential loads.

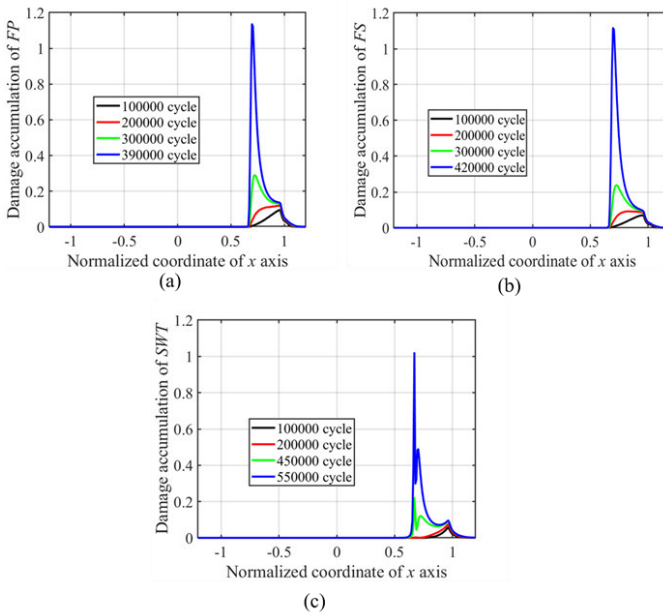


Figure 5-5– Variation of damage accumulation value with cycles for Exp. 1

Variation of critical plane parameters with cycles for Exp. 1 is shown in Figure 5-4. It can be concluded that the maximum values of FP , FS , and SWT tend to move from the trailing edge to the boundary of the stick-slip zone. The variation tendency of these three parameters is similar to each other. The crack initiation position predicted by both critical plane method and damage accumulation model is shown in Figure 5-5. The point of maximum damage accumulation value varies from trailing edge to the boundary of stick-slip zone due to the wear in partial slip zone. When the maximum damage accumulation parameter reaches 1, the predicted crack occurs on the corresponding location. The dramatic increments of the damage accumulation happen near the boundary of the stick-slip zone.

5.5 Lifetime prediction of crack initiation considering wear effect

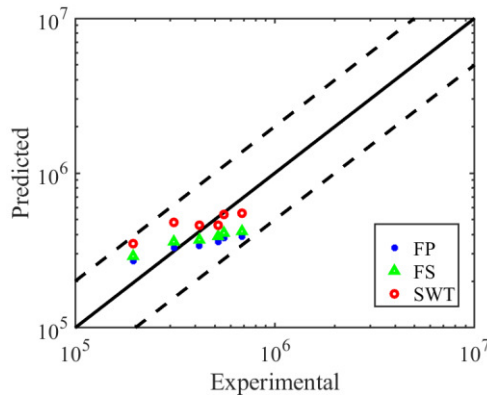


Figure 5-6– Crack initiation lifetime predicted by FP, FS and SWT for Exp. 1

Figure 5-6 shows that all the predicted lifetime lies in $\pm 2N_i$ error band. When the experimental lifetime is lower, then the predicted lifetime by all three

critical plane methods tends to be higher than the experimental one. When the experimental lifetime is higher, then the predicted lifetime tends to be lower than the experimental one. This phenomenon is caused by the dramatic increase in the critical plane parameters with the evolution of the profiles as shown Figure 5-4.

5.6 Effect of debris layer on crack initiation parameter

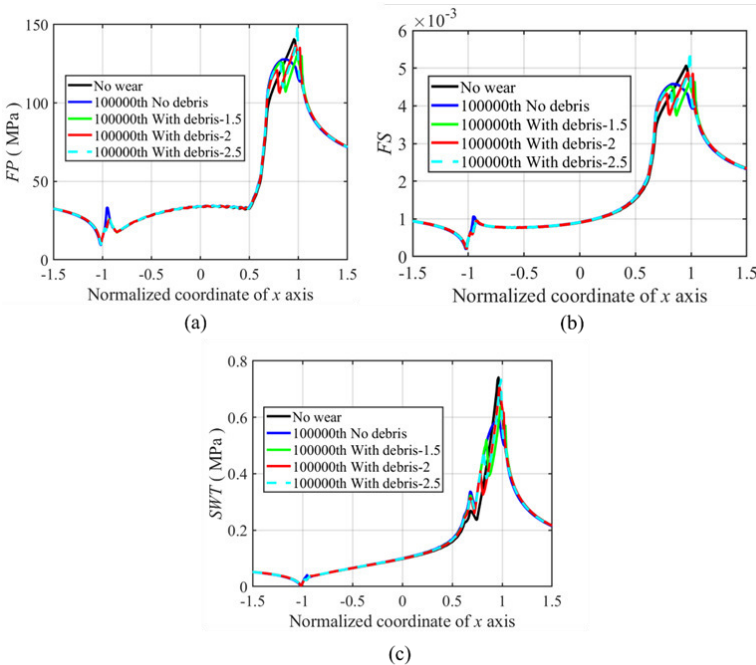


Figure 5-7– Critical plane parameters considering the debris effect after 10000 cycles

In the experiments, the crack initiation tends to be near the trailing edge under the debris layer, whereas in the FE model the crack initiation position tends to be near the boundary of stick-slip zone and far away from the contact edge [2]. Therefore, the crack initiation position is analysed considering the effect of the debris based on Figure 3-31. The critical plane parameters considering

the debris effect after 100000 cycles are shown in Figure 5-7. The values of 1.5, 2.0, 2.5 are used for Δh as shown in Figure 3-31 and the unit is $0.1 \mu\text{m}$. In the model without considering the debris effect, the maximum value locates near the boundary of stick and slip zone, while in the model considering the debris effect the maximum value locates near the trailing edge. The parameters considering the debris tend to have the same trend as those without wear. Moreover, the depth to the surface of the debris Δh also affects the profiles of the parameters on the contact surface. For $\Delta h = 0.25 \mu\text{m}$, the the maximum values of FP and FS approach to peak values of the corresponding parameter for the model without debris. This means that Δh also plays an important role in the whole process, i.e. the ejection and generation rate also affect the lifetime of the crack initiation. For SWT , the maximum value tends to be the same as that in the model without wear when Δh is equal to $0.25 \mu\text{m}$ and $0.2 \mu\text{m}$.

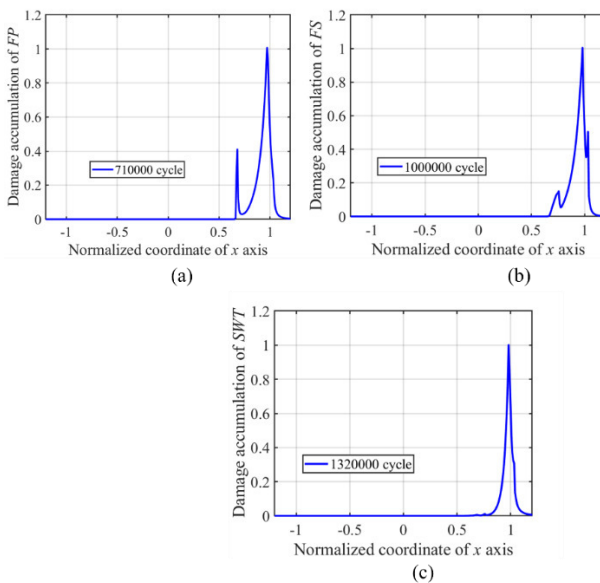


Figure 5-8– Shape of the damage accumulation value for three critical plane parameters that reaches 1, when Δh is $0.15 \mu\text{m}$

The variation of the damage accumulation parameter for three critical plane methods is shown in Figure 5-8 when Δh is $0.15 \mu\text{m}$. It can be concluded that the by considering the effect of the wear debris, the crack initiation position moves from the boundary of the stick-slip regime to the trailing edge compared with that shown in Figure 5-5. Moreover, for the damage accumulation value of *FP* and *FS* another peak value appears near the boundary of stick-slip regime. This peak value is lower than that near the trailing edge. For *SWT*, only one peak value appears near the trailing edge.

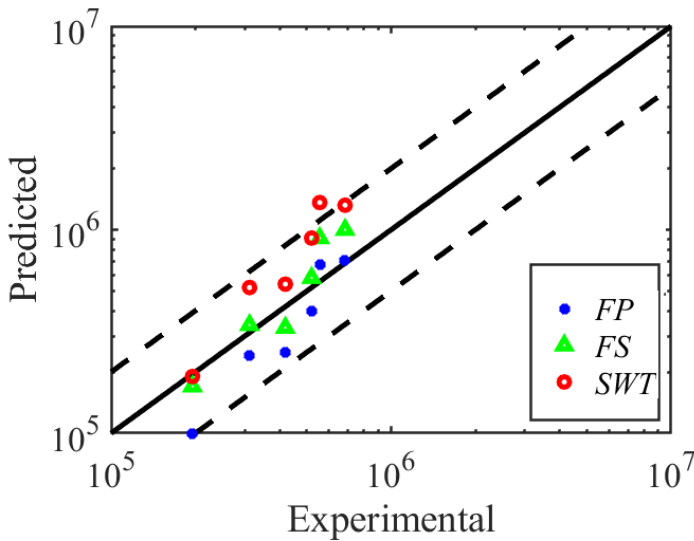


Figure 5-9– Crack initiation lifetime predicted by *FP*, *FS* and *SWT* for Exp. 1 considering debris when Δh is $0.15 \mu\text{m}$

Crack initiation lifetime predicted by *FP*, *FS* and *SWT* for Exp. 1, considering wear debris when Δh is $0.15 \mu\text{m}$, is shown in Figure 5-9. We can see that prediction results of *FP*, and *FS* are within $\pm 2N_i$, while most of the prediction point of *SWT* locates within $\pm 2N_i$ except 1 point, which is higher than $2N_i$. Moreover, the prediction results of *SWT* tend to be higher than those of the *FP*.

5.7 Conclusion remarks

This chapter analysed the effect of the loading cases on the wear profiles, effect of wear on fretting fatigue crack initiation and the effect of the debris on the critical plane parameters. Hereafter, the conclusion can be given as follows.

- The boundary condition influences the shear stress and wear profile when considering the wear in fretting fatigue model.
- The normal load tends to affect the wear width and wear depth, tangential load affects the wear volume and phase difference affects the side of the wear.
- Wear can affect the crack initiation of the fretting fatigue crack initiation, the predicted lifetime tends to be better than that without considering wear in Ref. [89] and all the predicted data lies in the $\pm 2N_i$ band.
- For both Ruiz parameters, $F1$ and $F2$, the maximum tends to be near the boundary of the slip and stick zone on the right-hand side.
- The effect of the wear debris on the critical parameters are considered. It is found that the debris can make the profile of the critical plane parameters close to that in the model without wear and move the location of crack initiation from boundary of stick and slip zone to the trailing edge. The kinematics of the debris also affects the maximum value of the critical plane parameters.
- The predicted lifetime when considering wear debris tends to have the same accuracy with that without considering debris effect. Therefore, the wear affects crack initiation of fretting fatigue for Aluminium 2024-T351 mainly on the location of initiation. The predicted lifetime without considering wear debris can be used as a reference for the

loading case. However, the predicted crack initiation location without considering debris effect cannot be used for the fretting fatigue case.

In this chapter, the effect of the debris is only considered after 100 000 cycle and the kinetics of the debris cannot be determined without experimental data. Therefore, in the further work, the predicted lifetime of the crack initiation considering the debris kinematics should be further investigated.

Chapter 6 Conclusions and future work

6.1 Conclusion

In this thesis, the analysis of fretting wear characteristics and the interaction between fretting wear and fretting fatigue are presented. The main novelties of the thesis are as follows:

1. The effect of variable wear coefficient on wear characteristics and surface stresses is analysed, while in the previous research, wear coefficient is considered as a constant in the whole fretting process [172].
2. At present, the wear characteristics of fretting wear are mostly obtained by FEM [173]. For the first time, POD-RBF is proposed to predict wear characteristics in different loading conditions with high efficiency and accuracy.
3. In Ref. [174], the effect of wear on fatigue is analysed by FEM. However, the effect of the debris is not considered in the fretting process. In this thesis, the effect of wear on crack initiation of fretting

fatigue in partial slip regime is analysed with and without considering the the effect of debris layer by critical plane methods.

Based on the above-mentioned novelties, the detailed conclusions of the thesis are listed as follows.

In gross sliding regime, the characteristics of the wear profile has an opposite effect on the maximum tangential and shear stress for both flat specimen and cylindrical specimen. Lower maximum stress corresponds to the higher wear characteristics. The effect of wear volume on the plasticity accumulation is significant. The higher wear volume caused less plasticity accumulation. The effect of VWCM for flat and cylindrical specimen on the history of stress, wear characteristics and plasticity accumulation are significant. In partial slip regime, the characteristics of the wear profile has an opposite effect on the maximum shear stress and positive effect on the tangential stress for both flat specimen and cylindrical specimen. Lower maximum shear stress and higher maximum tangential stress corresponds to the higher wear characteristics. The effect of wear volume on the plasticity accumulation is not significant. Plasticity accumulation in CWCM tends to be higher than that in VCWM for both specimen and cylinder. The effect of VWCM for flat and cylindrical specimen on the history of stress, wear characteristics and plasticity accumulation are significant. The history of stress and strain in VWCM differs from that in CWCM. Stress and strain history can affect the crack initiation lifetime. Therefore, the effect of VWCM on crack initiation can be investigated in future.

A prediction tool for fretting wear characteristics, i.e. wear width and wear depth, namely POD-RBF, is proposed. FEM is commonly used to predict the wear characteristics; however, it is time-consuming, especially when different parameters such as slip amplitude, number of cycles and normal loads, would be considered. For example, for every load case, a new FE model should be solved. Through POD-RBF, wear characteristics can be predicted within 1 second based on the database for some cases, obtained by FEM. To validate the accuracy, efficiency, and applicability of POD-RBF, it is compared with

the GM (1, 1) and PCF of second order when the load and oscillatory displacement are given. The results show that the accuracy of POD-RBF is greater than 95% and the efficiency is the highest among the three considered prediction methods. To further investigate the applicability of POD-RBF for any combination of displacement amplitude, number of cycles and normal load, five random load cases are applied. Based on the database, the accuracy of wear characteristics prediction under randomly generated load cases is higher than 95% by POD-RBF. Compared with ANN, POD-RBF shows higher computational efficiency and accuracy. This prediction tools can be used to predict fretting wear characteristics properly.

This thesis analysed the effect of the loading cases on the wear profiles, effect of wear on fretting fatigue crack initiation and the effect of the debris on the critical plane parameters. Hereafter, the conclusion can be given as follows.

- The boundary condition influences the shear stress and wear profile when considering the wear in fretting fatigue model.
- The normal load tends to affect the wear width and wear depth, tangential load affects the wear volume and phase difference affects the side of the wear.
- Wear can affect the crack initiation of the fretting fatigue crack initiation, the predicted lifetime tends to be better than that without considering wear in Ref. [89] and all the predicted data lies in the $\pm 2N_i$ band.
- For both Ruiz parameters, $F1$ and $F2$, the maximum tends to be near the boundary of the slip and stick zone on the right-hand side.
- The effect of the wear debris on the critical parameters are considered. It is found that the debris can make the profile of the critical plane parameters close to that in the model without wear and move the location of crack initiation from boundary of stick and slip zone to the

trailing edge. The kinematics of the debris also affects the maximum value of the critical plane parameters.

- The predicted lifetime when considering wear debris tends to have the same accuracy with that without considering debris effect. Therefore, the wear affects crack initiation of fretting fatigue for Aluminium 2024-T351 mainly on the location of initiation. The predicted lifetime without considering wear debris can be used as a reference for the loading case. However, the predicted crack initiation location without considering debris effect cannot be used for the fretting fatigue case.

6.2 Future work

Based on the research in this thesis, the following future research work can be further investigated:

- The history of stress and strain in VWCM differs from that in CWCM. Stress and strain history can affect the crack initiation lifetime. Therefore, the effect of VWCM on crack initiation can be further investigated in partial slip and gross slip regime.
- Besides normal load, oscillatory displacement and cycles that are considered in the prediction of the wear characteristics, other parameters like geometry of the configuration, material properties etc., all these parameters can be considered by POD-RBF or other predictive tools to predict the wear characteristics in more complicated cases.
- In this thesis, the debris is considered in fretting fatigue. However, the kinematics of the debris is assumed to be in a constant condition. It should be further validated and investigated by experiments. With validated wear kinematics in partial slip regime, the effect of debris on fretting fatigue can be further investigated. Moreover, the properties and microstructure of the debris layer can be analysed

- experimentally to have more insights to the mechanism of wear phenomenon on fretting fatigue.
- Considering the effect of wear on fretting fatigue, the contact surface geometry changes cycle by cycle. In this way, the stress distribution on the contact surface can affect the crack opening in the crack propagation phase. Therefore, the effect of fretting wear in fatigue propagation can be investigated.
 - The crack initiation criteria are all based on the common equations when considering wear. The theory of crystal plasticity and crystal plasticity finite element method can be used to investigate the crack initiation and propagation phenomenon when considering wear based on experimental and numerical analyses.
 - To reduce the wear in fretting process, surface treatment is commonly used to reduce the wear on contact surface. Ultrasonic nanocrystal surface modification is a choice to increase the anti-wear ability. The wear mechanism by this surface treatment can be analysed experimentally and numerically.

References

1. Vingsbo, O. and S. Söderberg, *On fretting maps*. *Wear*, 1988. **126**(2): p. 131-147.
2. Szolwinski, M.P. and T.N. Farris, *Observation, analysis and prediction of fretting fatigue in 2024-T351 aluminum alloy*. *Wear*, 1998. **221**(1): p. 24-36.
3. Beek, A.V., *Advanced Engineering Design: Lifetime Performance and Reliability*. 2006.
4. Hills, D.A., *Mechanics of fretting fatigue*. *Wear*, 1994. **175**(1-2): p. 107-113.
5. Anderson, T.L., *Fracture mechanics: fundamentals and applications*. 2017: CRC press.
6. Cuffaro, V., F. Cura, and A. Mura, *Analysis of the pressure distribution in spline couplings*. ARCHIVE Proceedings of the Institution of Mechanical Engineers Part C Journal of Mechanical Engineering Science 1989-1996 (vols 203-210), 2012. **226**(12): p. 2852-2859.
7. Cuffaro, V., F. Curà, and A. Mura, *Fretting wear damage in crowned splined couplings*. Powertransmissionworld Com, 2014.
8. English, R., A. Ashkanfar, and G. Rothwell, *A computational approach to fretting wear prediction at the head–stem taper junction of total hip replacements*. *Wear*, 2015. **338-339**: p. 210-220.

9. Fallahnezhad, K., et al., *An adaptive finite element simulation of fretting wear damage at the head-neck taper junction of total hip replacement: The role of taper angle mismatch*. Journal of the Mechanical Behavior of Biomedical Materials, 2017. **75**: p. 58-67.
10. Naboulsi, S., and Calcaterra, J. *Fretting fatigue investigation of dovetail*. in *In 11th International Conference on Fracture 2005*. 2005.
11. Llavori, I., et al., *Development of a modular fretting wear and fretting fatigue tribometer for thin steel wires: Design concept and preliminary analysis of the effect of crossing angle on tangential force*. Metals, 2019. **9**(6): p. 674.
12. Hertz, H.R.J.V.d.V.z.B.d.G., Berlin, *Über die Berührung fester elastischer Körper und Über die Harte*. 1882: p. 449.
13. Johnson, K.L. and K.L. Johnson, *Contact mechanics*. 1987: Cambridge university press.
14. Popov, V.L., *Contact mechanics and friction*. 2010: Springer.
15. Hills, D.A. and D. Nowell, *Mechanics of fretting fatigue*. 1994: Springer Netherlands.
16. Klaffke, D., *Fretting wear of ceramics*. Tribology international, 1989. **22**(2): p. 89-101.
17. Eden, E.M., W.N. Rose, and F.L. Cunningham, *The endurance of metals: experiments on rotating beams at University College, London*. ARCHIVE Proceedings of the Institution of Mechanical Engineers 1847-1982 (vols 1-196), 2006. **81**(1911): p. 839-974.
18. Zhu, M.H. and Z.R. Zhou, *On the mechanisms of various fretting wear modes*. Tribology International, 2011. **44**(11): p. 1378-1388.
19. Zhang, P., et al., *Torsional fretting and torsional sliding wear behaviors of CuNiAl against 42CrMo4 under dry condition*. Tribology International, 2018. **118**: p. 11-19.

-
20. Ovcharenko, A. and I. Etsion, *Junction growth and energy dissipation at the very early stage of elastic-plastic spherical contact fretting*. Journal of Tribology, 2009. **131**(3): p. 031602.
 21. Berthier, Y., L. Vincent, and M. Godet, *Fretting fatigue and fretting wear*. Tribology international, 1989. **22**(4): p. 235-242.
 22. Bock, E. and J. Whitley, *Fretting corrosion in electric contacts*. Electric Contacts-1974, 1974: p. 128.
 23. Mindlin, R.D., *Compliance of Elastic Bodies in Contact*. Journal of Applied Mechanics, 1949. **16**: p. 259-268.
 24. Zhou, Z.R., et al., *Progress in fretting maps*. Tribology International, 2006. **39**(10): p. 1068-1073.
 25. Zhou, Z., S. Fayeulle, and L. Vincent, *Cracking behaviour of various aluminium alloys during fretting wear*. Wear, 1992. **155**(2): p. 317-330.
 26. Zhou, Z., V. Pellerin, and L. Vincent. *Wear mechanisms in fretting of aluminium alloys*. in *Proc. of 2nd Int. Conf. on Aluminium Alloys*. 1990.
 27. Vincent, Z.R.Z., *Mixed fretting regime*. Wear, 1995.
 28. Fouvry, S., P. Kapsa, and L. Vincent, *Analysis of sliding behaviour for fretting loadings: determination of transition criteria*. Wear, 1995. **185**(1-2): p. 35-46.
 29. Hurricks, P.L., *The mechanism of fretting — A review*. Wear, 1970. **15**(6): p. 389-409.
 30. Paulin, C., S. Fouvry, and S. Deyber, *Wear kinetics of Ti-6Al-4V under constant and variable fretting sliding conditions*. Wear, 2005. **259**(1): p. 292-299.
 31. Huang, W., et al., *Fretting wear behavior of AZ91D and AM60B magnesium alloys*. Wear, 2006. **260**(11-12): p. 1173-1178.
 32. Cruzado, A., M.A. Urchegui, and X. Gómez, *Finite element modeling of fretting wear scars in the thin steel wires: Application in crossed cylinder arrangements*. Wear, 2014. **318**(1-2): p. 98-105.

33. Li, J. and Y.H. Lu, *Effects of displacement amplitude on fretting wear behaviors and mechanism of Inconel 600 alloy*. Wear, 2013. **304**(1): p. 223-230.
34. Anandavel, K. and R.V. Prakash, *Effect of three-dimensional loading on macroscopic fretting aspects of an aero-engine blade-disc dovetail interface*. Tribology International, 2011. **44**(11): p. 1544-1555.
35. Yan, S., D. Zhang, and G.E. Shirong, *Effect of fretting amplitudes on fretting wear behavior of steel wires in coal mines*. International Journal of Mining Science and Technology(矿业科学技术学报), 2010. **20**(6): p. 803-808.
36. A, K.N., et al., *Surface modification of aluminum alloy to improve fretting wear properties*. Tribology International, 2016. **93**: p. 702-708.
37. Sato, J., et al., *Effect of lubricants on fretting wear of steel*. Wear, 1988. **125**(1): p. 83-95.
38. Achard, J., *Contact and Rubbing of Flat Surface*. Journal of Applied Physics, 1953. **24**(8): p. 981-988.
39. Van Beek, A., *Advanced engineering design*. TU Delft, Delft, The Netherlands, 2015: p. 191-192.
40. McColl, I., J. Ding, and S. Leen, *Finite element simulation and experimental validation of fretting wear*. Wear, 2004. **256**(11-12): p. 1114-1127.
41. Fouvry, S., P. Kapsa, and L. Vincent, *Quantification of fretting damage*. Wear, 1996. **200**(1): p. 186-205.
42. Fouvry, S., et al., *An energy description of wear mechanisms and its applications to oscillating sliding contacts*. Wear, 2003. **255**(1): p. 287-298.
43. Sauger, E., et al., *Tribologically transformed structure in fretting*. Wear, 2000. **245**(1-2): p. 39-52.

-
44. Sauger, E., et al., *Study of the tribologically transformed structure created during fretting tests*. Tribology International, 2000. **33**(11): p. 743-750.
 45. Zhou, Z., et al., *Nucleation and early growth of tribologically transformed structure (TTS) induced by fretting*. Wear, 1997. **212**(1): p. 50-58.
 46. Fridrici, V., S. Fouvry, and P. Kapsa, *Effect of shot peening on the fretting wear of Ti-6Al-4V*. Wear, 2001. **250**(1-12): p. 642-649.
 47. DANG, V., *Contribution à l'étude de la transformation tribologique superficielle en fretting*. 1997, INSA de Lyon.
 48. Paulin, C., S. Fouvry, and S. Deyber, *Wear kinetics of Ti-6Al-4V under constant and variable fretting sliding conditions*. Wear, 2005. **259**(1-6): p. 292-299.
 49. Cruzado, A., et al., *Fretting wear of thin steel wires. Part 1: Influence of contact pressure*. Wear, 2010. **268**(11): p. 1409-1416.
 50. Guo, X., et al., *Effects of sliding amplitude and normal load on the fretting wear behavior of alloy 690 tube exposed to high temperature water*. Tribology International, 2017. **116**: p. 155-163.
 51. Ohmae, N. and T. Tsukizoe, *The effect of slip amplitude on fretting*. Wear, 1974. **27**(3): p. 281-294.
 52. Xushou, Z., Z. Chuenhe, and Z. Chailu, *Slip amplitude effects and microstructural characteristics of surface layers in fretting wear of carbon steel*. Wear, 1989. **134**(2): p. 297-309.
 53. Warmuth, A.R., et al., *The effect of contact geometry on fretting wear rates and mechanisms for a high strength steel*. Wear, 2013. **301**(1): p. 491-500.
 54. Cruzado, A., et al., *Fretting wear of thin steel wires. Part 2: Influence of crossing angle*. Wear, 2011. **273**(1): p. 60-69.

55. Winter, T., et al., *Coefficient of friction evolution with temperature under fretting wear for FeCrAl fuel cladding candidate*. Journal of Nuclear Materials, 2019. **520**: p. 140-151.
56. Kesavan, D., et al., *High temperature fretting wear prediction of exhaust valve material*. Tribology International, 2016. **100**: p. 280-286.
57. Rybiak, R., S. Fouvry, and B. Bonnet, *Fretting wear of stainless steels under variable temperature conditions: Introduction of a 'composite' wear law*. Wear, 2010. **268**(3): p. 413-423.
58. Hager, C.H., J.H. Sanders, and S. Sharma, *Effect of high temperature on the characterization of fretting wear regimes at Ti6Al4V interfaces*. Wear, 2006. **260**(4): p. 493-508.
59. Kayaba, T. and A. Iwabuchi, *Effect of the hardness of hardened steels and the action of oxides on fretting wear*. Wear, 1981. **66**(1): p. 27-41.
60. Ramesh, R. and R. Gnanamoorthy, *Effect of hardness on fretting wear behaviour of structural steel, En 24, against bearing steel, En 31*. Materials & Design, 2007. **28**(5): p. 1447-1452.
61. Kubiak, K., et al., *Behaviour of shot peening combined with WC-Co HVOF coating under complex fretting wear and fretting fatigue loading conditions*. Surface and Coatings Technology, 2006. **201**(7): p. 4323-4328.
62. Park, C., et al., *Influence of diode laser heat treatment and wear conditions on the fretting wear behavior of a mold steel*. Wear, 2019. **434-435**: p. 202961.
63. Li, L., et al., *Finite element analysis of fretting wear considering variable coefficient of friction*. Proceedings of the Institution of Mechanical Engineers, Part J: Journal of Engineering Tribology, 2019. **233**(5): p. 758-768.
64. Yue, T. and M. Abdel Wahab, *Finite element analysis of fretting wear under variable coefficient of friction and different contact regimes*. Tribology International, 2017. **107**: p. 274-282.

-
65. Pereira, K., T. Yue, and M.A. Wahab, *Multiscale analysis of the effect of roughness on fretting wear*. Tribology International, 2017. **110**: p. 222-231.
 66. Rodríguez-Tembleque, L., R. Abascal, and M.H. Aliabadi, *A boundary elements formulation for 3D fretting-wear problems*. Engineering Analysis with Boundary Elements, 2011. **35**(7): p. 935-943.
 67. Rodríguez-Tembleque, L. and M.H. Aliabadi, *Numerical simulation of fretting wear in fiber-reinforced composite materials*. Engineering Fracture Mechanics, 2016. **168**: p. 13-27.
 68. Leonard, B.D., et al., *Fretting Wear Modeling of Coated and Uncoated Surfaces Using the Combined Finite-Discrete Element Method*. Journal of Tribology, 2011. **133**(2).
 69. Lee, C.Y., et al., *Application of influence function method on the fretting wear of tube-to-plate contact*. Tribology International, 2009. **42**(6): p. 951-957.
 70. Yue, T. and M. Abdel Wahab, *A numerical study on the effect of debris layer on fretting wear*. Materials, 2016. **9**(7): p. 597.
 71. Ding, J., et al., *A finite element based approach to simulating the effects of debris on fretting wear*. Wear, 2007. **263**(1-6): p. 481-491.
 72. Arnaud, P., S. Fouvry, and S.J.W. Garcin, *A numerical simulation of fretting wear profile taking account of the evolution of third body layer*. 2017. **376**: p. 1475-1488.
 73. Leonard, B.D., et al., *Third body modeling in fretting using the combined finite-discrete element method*. International Journal of Solids and Structures, 2014. **51**(6): p. 1375-1389.
 74. Leonard, B.D., et al., *Fretting wear modeling of coated and uncoated surfaces using the combined finite-discrete element method*. Journal of Tribology, 2011. **133**(2): p. 021601.

75. Leonard, B.D., et al., *A numerical and experimental investigation of fretting wear and a new procedure for fretting wear maps*. Tribology Transactions, 2012. **55**(3): p. 313-324.
76. S., et al., *Introduction of a new sliding regime criterion to quantify partial, mixed and gross slip fretting regimes: Correlation with wear and cracking processes*. Wear, 2010. **269**(7-8): p. 515-524.
77. Kubiak, K., S. Fouvry, and A.M. Marechal, *A practical methodology to select fretting palliatives: Application to shot peening, hard chromium and WC-Co coatings*. Wear, 2005. **259**(1): p. 367-376.
78. Jin, O. and S. Mall, *Effects of slip on fretting behavior: experiments and analyses*. Wear, 2004. **256**(7-8): p. 671-684.
79. Sabelkin, V. and S. Mall, *Investigation into relative slip during fretting fatigue under partial slip contact condition*. Fatigue & Fracture of Engineering Materials & Structures, 2010. **28**(9): p. 809-824.
80. Madge, J.J., et al., *Contact-evolution based prediction of fretting fatigue life: Effect of slip amplitude*. Wear, 2007. **262**(9): p. 1159-1170.
81. Majzoobi, G.H., K. Azadikhah, and J. Nemati, *The effects of deep rolling and shot peening on fretting fatigue resistance of Aluminum-7075-T6*. Materials Science and Engineering: A, 2009. **516**(1): p. 235-247.
82. Endo, K. and H. Goto, *Initiation and propagation of fretting fatigue cracks*. Wear, 1976. **38**(2): p. 311-324.
83. Pape, J. and R. Neu, *Influence of contact configuration in fretting fatigue testing*. Wear, 1999. **225**: p. 1205-1214.
84. Husheng, G., G. Haicheng, and Z. Huijiu, *The effect of hardness on the fretting fatigue of alloy steels*. Fatigue & Fracture of Engineering Materials & Structures, 1991. **14**(7): p. 789-796.
85. Fu, Y., J. Wei, and A.W. Batchelor, *Some considerations on the mitigation of fretting damage by the application of surface-*

-
- modification technologies*. Journal of Materials Processing Technology, 2000. **99**(1-3): p. 231-245.
86. Bhatti, N.A. and M.A. Wahab, *Finite element analysis of fretting fatigue under out of phase loading conditions*. Tribology International, 2017. **109**: p. 552-562.
87. Bhatti, N.A. and M.A.J.T.I. Wahab, *Fretting fatigue crack nucleation: A review*. 2018. **121**: p. 121-138.
88. Findley, W.N., *A theory for the effect of mean stress on fatigue of metals under combined torsion and axial load or bending*. Journal of Engineering for Industry, 1959. **81**(4): p. 301-305.
89. Bhatti, N.A. and M.A. Wahab, *A numerical investigation on critical plane orientation and initiation lifetimes in fretting fatigue under out of phase loading conditions*. Tribology International, 2017. **115**: p. 307-318.
90. Park, J. and D. Nelson, *Evaluation of an energy-based approach and a critical plane approach for predicting constant amplitude multiaxial fatigue life*. International Journal of Fatigue, 2000. **22**(1): p. 23-39.
91. Bhatti, N.A., *Numerical Modelling of Fretting Fatigue Crack Nucleation under Out-of-Phase Loading*. 2018, Ghent University.
92. Fatemi, A. and D.F. Socie, *A critical plane approach to multiaxial fatigue damage including out - of - phase loading*. Fatigue & Fracture of Engineering Materials & Structures, 1988. **11**(3): p. 149-165.
93. Neu, R.W., J.A. Pape, and D.R. Swalla, *Methodologies for linking nucleation and propagation approaches for predicting life under fretting fatigue*, in *Fretting fatigue: current technology and practices*. 2000, ASTM International.
94. Socie, D., *Critical plane approaches for multiaxial fatigue damage assessment*, in *Advances in multiaxial fatigue*. 1993, ASTM International.

95. Szolwinski, M.P. and T.N. Farris, *Mechanics of fretting fatigue crack formation*. Wear, 1996. **198**(1-2): p. 93-107.
96. Ruiz, C., P.H.B. Boddington, and K.C. Chen, *An investigation of fatigue and fretting in a dovetail joint*. Experimental Mechanics, 1984. **24**(3): p. 208-217.
97. A, N.A.B. and M.A.W.B.C. D, *Finite element analysis of fretting fatigue under out of phase loading conditions*. Tribology International, 2017. **109**: p. 552-562.
98. Kachanov, L.M., *Time of the Rupture Process under Creep Conditions*, *Izy Akad. Nank S. S. R. Otd Tech Nauk*, 1958. **8**.
99. Dhar, S., P.M. Dixit, and R. Sethuraman, *A continuum damage mechanics model for ductile fracture*. International Journal of Pressure Vessels and Piping, 2000. **77**(6): p. 335-344.
100. Lemaitre, J., *Formulation and Identification of Damage Kinetic Constitutive Equations*. 1987: Continuum Damage Mechanics Theory and Application.
101. Lemaitre, J., *A Course on Damage Mechanics*. 1992: A Course on Damage Mechanics.
102. Hojjati-Talemi, R. and M.A. Wahab, *Fretting fatigue crack initiation lifetime predictor tool: Using damage mechanics approach*. Tribology International, 2013. **60**: p. 176-186.
103. Bhatti, N.A. and M. Abdel Wahab, *Fretting fatigue damage nucleation under out of phase loading using a continuum damage model for non-proportional loading*. Tribology International, 2018. **121**: p. 204-213.
104. Haddad, M., K.N. Smith, and T.H. Topper, *Fatigue Crack Propagation of Short Cracks*. Trans.asme J.eng.mater.technol, 1979. **110**(1): p. 42-46.
105. Irwin, G.R., *Analysis of Stresses and Strains Near End of a Crack Traversing a Plate*. journal of applied mechanics, 1956.
106. Anderson, T.L., *Fracture Mechanics – Fundamentals and Applications*. 1991.

-
107. Ribeaucourt, R., M.C. Baietto-Dubourg, and A. Gravouil, *A new fatigue frictional contact crack propagation model with the coupled X-FEM/LATIN method*. Computer Methods in Applied Mechanics & Engineering, 2007. **196**(33-34): p. 3230-3247.
 108. Giner, E., et al., *Orientation of propagating crack paths emanating from fretting-fatigue contact problems*. Frattura ed Integrità Strutturale, 2016.
 109. Hourlier, F., et al., *Fatigue Crack Path Behavior Under Polymodal Fatigue*. Multiaxial Fatigue, 1985.
 110. Pereira, K. and M. Abdel Wahab, *Fretting fatigue crack propagation lifetime prediction in cylindrical contact using an extended MTS criterion for non-proportional loading*. Tribology International, 2017. **115**: p. 525-534.
 111. J., et al., *A Mixed-Mode Crack Analysis of Isotropic Solids Using Conservation Laws of Elasticity*. Journal of Applied Mechanics, 1980. **47**(2): p. 335-341.
 112. Hoenig, A., *Near-tip behavior of a crack in a plane anisotropic elastic body*. Engineering Fracture Mechanics, 1982. **16**(3): p. 393-403.
 113. Warzynek, P.A., B.J. Carter, and L. Banks-Sills, *The M-Integral for Computing Stress Intensity Factors in Generally Anisotropic Materials*. 2005.
 114. Tsai, C.T. and S. Mall, *Elasto-plastic finite element analysis of fretting stresses in pre-stressed strip in contact with cylindrical pad*. Finite Elements in Analysis & Design, 2000. **36**(2): p. 171-187.
 115. Mall, S.N., *Fretting fatigue crack initiation behavior using process volume approach and finite element analysis*. Tribology International, 2003.
 116. Bhatti, N.A., K. Pereira, and M. Abdel Wahab, *A continuum damage mechanics approach for fretting fatigue under out of phase loading*. Tribology International, 2017: p. S0301679X17303870.

117. Bhatti, N.A., K. Pereira, and M.A. Wahab, *Effect of stress gradient and quadrant averaging on fretting fatigue crack initiation angle and life*. Tribology International, 2019. **131**: p. 212-221.
118. Kumar, D., et al., *Fretting fatigue stress analysis in heterogeneous material using direct numerical simulations in solid mechanics*. Tribology International, 2017.
119. Deng, Q., et al., *The effect of a critical micro-void defect on fretting fatigue crack initiation in heterogeneous material using a multiscale approach*. Tribology International, 2019. **141**: p. 105909.
120. Lanoue, F., A. Vadean, and B. Sanschagrin, *Finite element analysis and contact modelling considerations of interference fits for fretting fatigue strength calculations*. Simulation Modelling Practice & Theory, 2009. **17**(10): p. 1587-1602.
121. Ding, J., et al., *Fretting fatigue predictions in a complex coupling*. International Journal of Fatigue, 2007. **29**(7): p. 1229-1244.
122. Mantyla, et al., *Experimental and numerical investigation of fretting fatigue behavior in bolted joints*. Tribology International, 2016.
123. A, E.G., et al., *An Abaqus implementation of the extended finite element method*. Engineering Fracture Mechanics, 2009. **76**(3): p. 347-368.
124. Moës, N., J.D. And, and T. Belytschko, *A finite element method for crack growth without remeshing*. International Journal for Numerical Methods in Engineering, 1999.
125. Giner, E., et al., *Fretting fatigue life prediction using the extended finite element method*. International Journal of Mechanical Sciences, 2011. **53**(3): p. 217-225.
126. Sabsabi, M., E. Giner, and F.J. Fuenmayor, *Experimental fatigue testing of a fretting complete contact and numerical life*

-
- correlation using X-FEM*. International Journal of Fatigue, 2011. **33**(6): p. 811-822.
127. Llavori, I., et al., *Critical analysis of the suitability of crack propagation direction criteria for 2D cylindrical plain fretting contact*. Engineering Fracture Mechanics, 2019.
 128. Pereira, K. and M.A. Wahab, *Fretting fatigue lifetime estimation using a cyclic cohesive zone model*. Tribology International, 2019. **141**: p. 105899.
 129. Hojjati-Talemi, R., et al., *Prediction of fretting fatigue crack initiation and propagation lifetime for cylindrical contact configuration*. Tribology International, 2014. **76**: p. 73-91.
 130. Peng, J., et al., *Study on the damage evolution of torsional fretting fatigue in a 7075 aluminum alloy*. Wear, 2018. **402-403**.
 131. Bhatti, N.A., K. Pereira, and M.A.J.T.I. Wahab, *Effect of stress gradient and quadrant averaging on fretting fatigue crack initiation angle and life*. 2019. **131**: p. 212-221.
 132. Bhatti, N.A. and M.A.J.T.I. Wahab, *Fretting fatigue damage nucleation under out of phase loading using a continuum damage model for non-proportional loading*. 2018. **121**: p. 204-213.
 133. Pereira, K. and M.A. Wahab, *Fretting fatigue lifetime estimation using a cyclic cohesive zone model*. Tribology International, 2020. **141**: p. 105899.
 134. Madge, J., et al., *Contact-evolution based prediction of fretting fatigue life: effect of slip amplitude*. Wear, 2007. **262**(9-10): p. 1159-1170.
 135. Madge, J., S. Leen, and P. Shipway, *The critical role of fretting wear in the analysis of fretting fatigue*. Wear, 2007. **263**(1-6): p. 542-551.
 136. Shen, F., W. Hu, and Q. Meng, *A damage mechanics approach to fretting fatigue life prediction with consideration of elastic-plastic damage model and wear*. Tribology International, 2015. **82**: p. 176-190.

137. Ding, J., et al., *Simple parameters to predict effect of surface damage on fretting fatigue*. International Journal of Fatigue, 2011. **33**(3): p. 332-342.
138. O'Halloran, S.M., et al., *A combined wear-fatigue design methodology for fretting in the pressure armour layer of flexible marine risers*. Tribology International, 2017.
139. Madge, J., S. Leen, and P. Shipway, *A combined wear and crack nucleation-propagation methodology for fretting fatigue prediction*. International Journal of Fatigue, 2008. **30**(9): p. 1509-1528.
140. Giner, E., et al., *Extended finite element method for fretting fatigue crack propagation*. International Journal of Solids & Structures, 2010. **45**(22-23): p. 5675-5687.
141. Hattori, T., N. Nishimura, and M. Yamashita, *Fretting fatigue strength estimation considering the fretting wear process*. Key Engineering Materials, 2007. **353-358**(Pt2): p. 882-885.
142. Wang, D., et al., *Dynamic wear evolution and crack propagation behaviors of steel wires during fretting-fatigue*. Tribology International, 2016. **101**: p. 348-355.
143. Zhang, et al., *Fretting fatigue behavior of steel wires contact interface under different crossing angles*. Wear Lausanne, 2018.
144. Shen, Y., et al., *Fretting wear behaviors of steel wires under friction-increasing grease conditions*. Tribology International, 2011. **44**(11): p. 1511-1517.
145. Fouvry, S., P. Duo, and P. Perruchaut, *A quantitative approach of Ti-6Al-4V fretting damage: friction, wear and crack nucleation*. Wear, 2004. **257**(9-10): p. 916-929.
146. Kim, D.-G. and Y.-Z. Lee, *Experimental investigation on sliding and fretting wear of steam generator tube materials*. Wear, 2001. **250**(1-12): p. 673-680.
147. Yue, T. and M.A. Wahab, *Finite element analysis of fretting wear under variable coefficient of friction and different contact regimes*. Tribology International, 2017. **107**: p. 274-282.

-
148. Paulin, C., S. Fouvry, and C. Meunier, *Finite element modelling of fretting wear surface evolution: Application to a Ti-6Al-4V contact*. *Wear*, 2008. **264**(1-2): p. 26-36.
 149. Liang, Y., et al., *Proper orthogonal decomposition and its applications—Part I: Theory*. *Journal of Sound and vibration*, 2002. **252**(3): p. 527-544.
 150. Schilders, W.H., H.A. Van der Vorst, and J. Rommes, *Model order reduction: theory, research aspects and applications*. Vol. 13. 2008: Springer.
 151. Khatir, S., et al., *Damage detection and localization in composite beam structures based on vibration analysis*. *Mechanics*, 2015. **21**(6): p. 472-479.
 152. Khatir, S. and M.A. Wahab, *Fast simulations for solving fracture mechanics inverse problems using POD-RBF XIGA and Jaya algorithm*. *Engineering Fracture Mechanics*, 2019. **205**: p. 285-300.
 153. Benaissa, B., et al. *Application of proper orthogonal decomposition and radial basis functions for crack size estimation using particle swarm optimization*. in *Journal of Physics: Conference Series*. 2017. IOP Publishing.
 154. Wahlström, J., *A comparison of measured and simulated friction, wear, and particle emission of disc brakes*. *Tribology International*, 2015. **92**: p. 503-511.
 155. Hao, L. and Y. Meng, *Numerical prediction of wear process of an initial line contact in mixed lubrication conditions*. *Tribology Letters*, 2015. **60**(2): p. 31.
 156. Palavar, O., D. Özyürek, and A. Kalyon, *Artificial neural network prediction of aging effects on the wear behavior of IN706 superalloy*. *Materials & Design*, 2015. **82**: p. 164-172.
 157. Grzegorzec, W. and S.F. Scieszka, *Prediction on friction characteristics of industrial brakes using artificial neural networks*. *Proceedings of the Institution of Mechanical*

- Engineers, Part J: Journal of Engineering Tribology, 2014. **228**(10): p. 1025-1035.
158. Ju-Long, D., *Control problems of grey systems*. Systems & control letters, 1982. **1**(5): p. 288-294.
159. Julong, D., *Introduction to grey system theory*. The Journal of grey system, 1989. **1**(1): p. 1-24.
160. Chen, G. and Z. Zhou, *Study on transition between fretting and reciprocating sliding wear*. Wear, 2001. **250**(1-12): p. 665-672.
161. Raca, B., et al., *Wear numerical assessment for partial slip fretting fatigue conditions*. Tribology International, 2019. **136**: p. 508-523.
162. Tobi, A.M., et al., *A study on the interaction between fretting wear and cyclic plasticity for Ti-6Al-4V*. Wear, 2009. **267**(1-4): p. 270-282.
163. Soh, H.P., *Fretting wear studies of aeroengine materials*. 2006, University of Nottingham.
164. Usa, D.O.D.O., *Metallic Materials and elements for aerospace vehicle structures*. 1994.
165. Blatt, P.A., *Evaluation of Fatigue Crack Initiation Behavior of an Experimental Ternary Aluminum-lithium Alloy*. 1990: Purdue University.
166. Ashwin, A., et al., *Predicting the Wear Rate of Aluminum Alloy AA2024-T351 using Hybrid Linear function and Radial Basis Function*. IOP Conference Series: Materials ence and Engineering, 2019. **561**: p. 012046-.
167. Kumar, G.B.V., et al., *Studies on Al6061-SiC and Al7075-Al2O3 Metal Matrix Composites*. Journal of Minerals & Materials Characterization & Engineering, 2009. **09**(1): p. 43-55.
168. Nagentrau, M., W.A. Siswanto, and A.L. Mohd Tobi, *Predicting the sliding amplitude of plastic deformation in the*

-
- reciprocating sliding contact*. ARPN Journal of Engineering and Applied Sciences, 2016. **11**(4): p. 2266-2271.
169. Tobi, A.M., W. Sun, and P. Shipway, *Investigation on the plasticity accumulation of Ti-6Al-4V fretting wear by decoupling the effects of wear and surface profile in finite element modelling*. Tribology International, 2017. **113**: p. 448-459.
170. Lecun, Y., Y. Bengio, and G. Hinton, *Deep learning*. Nature, 2015. **521**(7553): p. 436.
171. Hirsch, M.R. and R.W. Neu, *A simple model for friction evolution infretting*. Wear, 2013. **301**(1-2): p. 517-523.
172. Argatov, I.I. and Y.S. Chai, *Fretting wear with variable coefficient of friction in gross sliding conditions*. Tribology International, 2020. **153**: p. 106555.
173. Li, L., et al., *Numerical analysis of fretting wear in lateral contact of sphere/sphere*. ARCHIVE Proceedings of the Institution of Mechanical Engineers Part J Journal of Engineering Tribology 1994-1996 (vols 208-210), 2021: p. 135065012098367.
174. Basseville, S., D. Missoum-Benziane, and G. Cailletaud, *3D finite element study of the fatigue damage of Ti-6Al-4V in presence of fretting wear*. Computational Mechanics, 2019. **64**(3): p. 663-683.

List of publications

A1 - Journal publications

1. Wang, S., S. Khatir, and M. Abdel Wahab, *Proper Orthogonal Decomposition for the prediction of fretting wear characteristics*. Tribology International, 2020. **152**: p. 106545.
2. Wang, S., T. Yue, and M.A. Wahab, *Multiscale Analysis of the Effect of Debris on Fretting Wear Process Using a Semi-Concurrent Method*. Computers, Materials and Continua, 2019. **61**(3): p. 17-35.
3. Wang S, Wahab MA. *A Numerical Study on the Effect of Variable Wear Coefficient on Fretting Wear Characteristics*. Materials. 2021; 14(8):1840.
4. Wang, S., T. Yue, and M.A. Wahab, *Effect of wear debris on fretting fatigue crack initiation*. Submitted to Friction, Springer, 2021.

C1 - Articles published in proceedings of scientific conferences

1. Wang, S., et al. *Numerical Investigation on the Effect of Wear Coefficient on Fretting Wear*. in *Proceedings of 1st International Conference on Structural Damage Modelling and Assessment*. 2020. Springer.
2. Wang, S. and M. Abdel Wahab. *Fretting Wear Effect on Fretting Fatigue by Findley Parameter in Mixed Slip Regime*. 2021. Singapore: Springer Singapore.

3. Wang, S. and M. Abdel Wahab. *Effect of Loading Conditions in Fretting Fatigue on Wear Characteristics*. 2020. Singapore: Springer Singapore.



The bad cutting condition of CNC milling machine causes wear on end-mill tools and burring chips.